Theoretical Studies of Electronic Structures and Dielectric Properties of Functional Materials

Akinori Fukushima

Department of Micro Engineering

Kyoto University

2010

Acknowledgements

I wish to express my gratitude to many people who helped me here. First, I am thankful to Professor Akitomo Tachibana for his guidance, valuable suggestions, discussions, and encouragement. Moreover, I also am grateful to Dr. Masato Senami, Dr. Kazuhide Ichikawa, Dr. Kentaro Doi, and Dr. Koichi Nakamura for their valuable suggestions and discussions. I also thanks Mr. Yutaka Mikazuki, Mr. Shinya Sugino, Mr. Toshiyuki Myoraku, and Mr. Kotaro Kimura, for their discussions to overcome difficulties. Parts of my studies are supported by Kyoto university venture business laboratory. Finally, I would like to express my gratitude to my parents for their continuing encouragement.

Introduction

Recently, due to the innovation of science and technology, new functional materials, such as nanowire and nanotube, are available. Compared with current materials, these ones have marvelous mechanical, electronic, and chemical properties, and hence they contribute to the downsizing of electric devices and constructions of new energy systems.

For example, these materials are employed to improve the capacity of hydrogen in fuel cells. High capacity is one of essential issues for practical use. Nanostructures are exceedingly suitable for these requirement. For the higher wt% of the hydrogen atom, a light weight and high hydrogen atom storage capacity are favored. For another example, in metal-oxide-semiconductor field effect transistor, the thickness of future insulator film is predicted to attain four and five dozens of atoms due to the downsizing of the transistor. However, for the thickness of insulator films, new serious problems are reported. The shortage of the thickness causes the increase of leak current, and also raise the waste of electric power. Hence, new materials, such as hafnia, are studied for alternative candidates.

For these nanosize materials, computational simulation process is useful for the material design and improvement of devices. Electronic structure calculations, such as first-principles calculation, are one of powerful tools. Hence they are used for analysis. Due to the drastic innovation of the technology, large-scale and high accuracy calculations are available in recent days. In the case of the analysis of the nanosize materials, physical properties highly depend on positions. Hence these quantities have to be analyzed in local viewpoints. The analysis with local density quantities is suitable for this purpose. One of these quantities is quantum energy density defined by Tachibana. Accordingly, in this thesis, the quantum energy density is applied for the study of materials for semiconductor devices and energy storage devices.

This thesis is organized as follows. First, Chapters 1 and 2 consist of theoretical studies of aluminum boride nanowires and a pentagonal aluminum nanowire for hydrogen adsorption materials. The development of hydrogen storage materials are one of essential factors of the practical use of a fuel cell. A nanowire has high ratio of surface area to its mass, and hence it is considered that nanowires are major candidates for hydrogen storage materials. In Chapter 1, hydrogen adsorption properties of aluminum boride nanowires are studied in the viewpoints of adsorption energy and quantum energy density. To analyze bonding states in detail, we investigate these nanowires in terms of quantum energy density, such as kinetic energy density, tension density, and stress tensor density. In addition, the changes of geometries and quantum energy density caused by the hydrogen adsorption are also discussed.

In Chapter 2, the hydrogen atom migration on a pentagonal aluminum nanowire surface is studied. To discuss this migration, we calculate the potential energy surface (PES) of the hydrogen atom adsorbed on the pentagonal nanowire. Using this result, we discuss the behavior of the hydrogen atom on the nanowire. Moreover, due to the light mass of hydrogen, zero point vibrational energy is large and the probability density of a nucleus may widely be distributed. Hence the probability density of hydrogen and deuterium atoms are calculated from PES results.

Second, Chapters 3 and 4 consist of theoretical studies of dielectric properties of high-k metal oxides. Dielectric breakdown observed for gate insulators in complementary-metal-oxide-semiconductor is a serious problem in the reliability of advanced electronic devices. Many researchers have argued that hafnium oxides are superior to silicon oxides for gate insulators. However, in the case of hafnium oxide insulators, Fermi level pinning is known to make threshold voltage uncontrollable. It is reported that oxygen vacancies may cause this phenomenon. Since local effects, such as vacancies, are important, local analysis is required for the investigation of prospective insulator films. Hence, in these Chapters, dielectric properties of hafnium oxides are discussed in terms of local dielectric constant defined by Tachibana. In particular, eigenvalues of a local dielectric constant tensor may have imaginary parts, and these imaginary parts are considered as the rotational response to external electric fields. In Chapter 3, local dielectric properties of a cubic hafnium oxide are investigated, since its dielectric constant is higher than that of the most stable monoclinic structure. In this Chapter, we show that the response of inner parts of the hafnia have the rotational feature and are very complex due to their asymmetric potential caused by nuclei.

In Chapter 4, the dielectric property of $\mathrm{HfLaO_x}$ is investigated, since it is reported that the incorporation of lanthanum atoms makes the structure of a hafnium oxide cubic. The purpose of this chapter is to clarify the effect of the lanthanum atom on the dielectric properties of cubic hafnium oxides in terms of local dielectric constant. The comparison between dielectric properties of hafnium and lanthanum oxides is made by local dielectric constant to show the effect of the lanthanum interpolation.

At last, in Chapter 5, we investigate a reaction of boron trichloride with iron hydroxide as a simple model of iron impurities in boron trichloride gas. Boron trichloride gas is widely used in a production process of semiconductor devices. However, for the downsizing of devices, iron impurities in the gas is considered to disturb their improvement, and hence the higher purity is needed. In this study, we clarify a reaction path of boron trichloride with iron hydroxide. Furthermore, we also discuss its stabilization process using interaction energy density, which is also one of quantities in quantum energy density framework, and clarify the usefulness of this density. We find stabilization takes place where electron density increases.

Contents

Chapter 1

Theoretical study of
the hydrogen adsorption on AlB nanowire

I Introduction

Nowadays, hydrogen energy is focused on as a clean energy resource, taking the place of fossil fuel. However, hydrogen is gas in room temperature and 1 atm, and thus hydrogen is difficult to store safely. One of methods of hydrogen storage is using hydrogen adsorption. For the hydrogen adsorption, higher weight percent storage is required for hydrogen to take rank with fossil fuel. However, high-weight-percent hydrogen storage has not been achieved for most of hydrogen storage materials. To overcome the difficulty, nanostructures are focused on. Nanostructures have larger surfaces than usual bulk structures. In this point, they have a possibility to store much hydrogen. Thus many studies are reported about hydrogen storage nanostructures [1, 2] and [3].

In nanomaterials, we particularly focused on one-dimensional structures such as a carbon nanotube (CNT) and Al nanowire [1, 4] and [5]. Makita *et al.* [4] calculated optimized geometries of aluminum nanowires based on gold nanowires using first-principles electronic structure calculations. Kawakami *et al.* [5] showed that hydrogen is adsorbed on a pentagonal Al nanowire model by the separation of a H_2 molecule into two H atoms. Nakano *et al.* [1] suggested to wrap Al species in carbon materials to enhance the hydrogen adsorption on CNT. Note that Suzuki *et al.* [6] reported that Al whiskers are actually fabricated by glancing angle deposition on a high temperature (HT-GLAD) substrate.

For a hydrogen molecule adsorption on these hydrogen storage materials, the low adsorption and dissociation energy under 1.0 eV is for the usage as a fuel cell. However, these energy are generically larger than 1.0 eV for these nanostructures. As a solution strategy to overcome the high adsorption and desorption energy, we suggest the use of the electronic and magnetic force. Thus in this paper, we focus on hydrogen adsorption abilities and the electronic structures of the AlB and Al nanowires. AlB nanowires are expected to be a better candidate for hydrogen storage because of light weight of B comparing to Al. We carry out first-principles calculations to optimized geometries, analyze electronic structures and clarify the influence of substitution of Al with B for the electronic structures. In addition, we analyze details of the electronic structures in terms of the quantum mechanical energy densities based on the regional density functional theory [7–12] and [13].

II Computational Methods

II-i Calculation model and method

Two AlB nanowire models for our calculation are shown in Figs. 1 and 2. Fig. 1(a) shows AlB_2 bulk models [14]. Fig. 1(b) and (c) shows the hexagonal nanowire models based on AlB2 bulk models. Fig. 1(d) and (e) are AlB_2 bulk surface models, which are called as the surface model 1 and model 2, respectively. These models are also based on AlB_2 bulk models. In this paper, the small nanowire of Fig. 1(c) is considered to be a hydrogen storage material. Other models are used to compare with nanowire models. In Fig. 2, another AlB nanowire and Al nanowire model are shown. This AlB nanowire model is composed of pentagonal B rings and an Al monoatomic wire. Fig. 2(a) shows the Al nanowire whose geometry was calculated by Makita *et al.* [4] consisting of pentagonal rings and monoatomic wire. Pentagonal B rings are placed with rotating by 36° for each ring. The AlB pentagonal nanowire shown in Fig. 2(b) is based on this Al nanowire. This AlB nanowire is also considered to be a hydrogen storage material.

The boundary condition of these models is imposed as periodic one. In our calculation, two kinds of supercell are used. 8.36 Å × 8.36 Å × 4c Å supercell is considered for AlB nanowires and 10.6 Å × 10.6 Å × 8c Å supercell is considered for Al nanowire. The parameter c is the distance from atoms on the axis to the pentagonal or hexagonal ring. If the smaller unit cell is used for Al nanowire, the interaction with next unit cell is not negligible. The supercells for AlB_2 surface models shown in Fig. 1(d) and (e) are 5.19 Å × 6.54 Å × 10.4 Å and 5.99 Å × 6.54 Å × 10.4 Å, respectively.

To investigate the electronic structures of the systems, variational calculations are carried out based on density functional theory, which is implemented by FHI98md program package [15]. Wave functions of valence electrons are expanded by Bloch functions, while atomic cores and inner-shell electrons are replaced by Hamman's norm conserving pseudopotentials [16]. The generalized-gradient-approximation method is employed for exchange-correlation interaction formulated by Perdew and Wang (PW91) [17]. The values of cutoff energy for wave functions with plane-wave expansion are chosen as 1088 eV for the AlB nanowires and 408 eV for the Al nanowire. The higher cutoff energy, 1088 eV, is required to derive an accurate result for B atoms. The cutoff energy for bulk surface model is the same as the lower cutoff energy. This is because the vacuum region is only one direction. Thus the lower cutoff energy is sufficient.

The density of states (DOS) are calculated using a density functional method with ADF program package [18]. Electron wave functions are expanded with linear combinations of atomic orbital basis set. In our calculation, hybridization of Slater type double-zeta basis and numerical one are employed.

The minimum point in a potential energy surface corresponds optimized structure. In the optimization calculation, two geometric parameters, the radius of nanowire r_1 and the length of the unit c, are determined. The geometries of our models are optimized with keeping their symmetries.

II-ii Quantum energy density

Quantum energy density [7–9] and [10] provides a number of information about electronic properties. First, we can derive kinetic energy density $n_T(\vec{r})$ from electron wave functions as follows,

$$n_T(\vec{r}) = -\frac{\hbar^2}{4m}\sum_i \nu_i \Big[\psi_i^*(\vec{r})\triangle\psi_i(\vec{r}) + \triangle\psi_i^*(\vec{r})\psi_i(\vec{r})\Big], \tag{1}$$

where ν_i is the occupation number of the ith state ψ_i. This energy density represents whether electrons can behave as classical particle. Electrons can freely move as obeying classical mechanics in positive kinetic energy density region, which is called as electronic drop region R_D. On the other hand, in the negative kinetic energy density region, which is called as electronic atmosphere region R_A, electrons cannot move freely and exist by only quantum tunneling effects. The boundary of these two regions is called electronic interface S. Stress tensor density $\overleftrightarrow{\tau}^S(\vec{r})$ is denoted as a 3×3 matrix whose element $\tau^{Skl}(\vec{r})$ is given by

$$\tau^{Skl}(\vec{r}) = \frac{\hbar^2}{4m}\sum_i \nu_i \left[\psi_i^*(\vec{r})\frac{\partial^2\psi_i(\vec{r})}{\partial x^k \partial x^l} - \frac{\partial\psi_i^*(\vec{r})}{\partial x^k}\frac{\partial\psi_i(\vec{r})}{\partial x^l} + \frac{\partial^2\psi_i^*(\vec{r})}{\partial x^k \partial x^l}\psi_i(\vec{r}) - \frac{\partial\psi_i^*(\vec{r})}{\partial x^l}\frac{\partial\psi_i(\vec{r})}{\partial x^k}\right]. \tag{2}$$

The positive and negative eigenvalues of $\overleftrightarrow{\tau}^S(\vec{r})$ represent the tensile and compressive stress, respectively. This tensor clarifies properties of chemical bonds, i.e., covalent bonds and metallic ones are distinguished. In this paper, we show the largest eigenvalues and their eigenvectors as the principal stress. Tension density $\vec{\tau}^S(\vec{r}) = (\tau^{S1}(\vec{r}), \tau^{S2}(\vec{r}), \tau^{S3}(\vec{r}))$ is given as the divergence of the stress tensor density, $\overleftrightarrow{\tau}^S(\vec{r})$,

$$\tau^{Sk}(\vec{r}) = \frac{\hbar^2}{4m}\sum_i \nu_i \left[\psi_i^*(\vec{r})\frac{\partial \triangle\psi_i(\vec{r})}{\partial x^k} - \frac{\partial\psi_i^*(\vec{r})}{\partial x^k}\triangle\psi_i(\vec{r}) + \frac{\partial \triangle\psi_i^*(\vec{r})}{\partial x^k}\psi_i(\vec{r}) - \triangle\psi_i^*(\vec{r})\frac{\partial\psi_i(\vec{r})}{\partial x^k}\right]. \tag{3}$$

III Results and Discussion

III-i Geometry of AlB nanowires

Fig. 3 shows the potential energy curves of both AlB nanowires for hydrogen storage. The energy curves are shown depending on the parameter r_1 and c. The optimized parameter corresponds to the minimum energy. The calculation is done in detail around the stable geometry. In the case of the pentagonal AlB nanowire, r_1 and c are determined at 1.31 Å and 1.80 Å, respectively. In this structure, the bond length between B atoms on the same ring is 1.54 Å and that between B and Al atoms is 2.23 Å. In the hexagonal AlB nanowire, r_1 and c are 1.54 Å and 1.68 Å, respectively, and the length between B (B and Al) atoms is 1.54 Å (2.28 Å). The optimized lengths of B−B bond are the same for both models, while other parameters are different from each other. On the other hand, in larger hexagonal nanowire models, the B−B bond length is 1.67 Å and the B−Al length is 2.36 Å. Moreover the interatomic distances in AlB_2 crystal are known as 1.73 Å for B−B and 2.38 Å for B−Al, these bond lengths are shorter in nanowire structures. In Al nanowire, the wire radius r_1 and the length of the unit c are 2.48 Å and 1.34 Å, respectively.

Fig. 4 shows $\triangle E/\triangle c$ as a function of $\triangle c$, where $\triangle c$ is the difference between c and that of the stable geometry, and $\triangle E$ is the difference in the potential energy. In both simple AlB nanowire models, the line can be approximately considered as straight. The gradients of the lines mean the stability of nanowires. This figure shows that larger energy is needed for larger $\triangle c$. Therefore, the gradients are regarded as Youngs modulus. Thus these figures indicate the stabilization of simple AlB nanowires in the axial direction. But the geometry which is calculated with keeping symmetry may be a meta-stable one. The stability of nanowire model is investigated by the deformation along the normal vibrational modes, where the norm of the eigenvectors is set to 0.1 Å. The normal vibrational modes are calculated with Gaussian 03 in the molecular system [19]. Atoms of models are moved to the direction of the imaginary normal vibrational modes and the total energy are calculated with this models in the periodic system. As a result, these nanowires are stable enough.

Electronic structure of simple nanowires

First, we discuss the electronic structure of nanowire models. The DOS and band structure of simple nanowire models are shown in Fig. 5. The Fermi levels are shifted to the origin in the vertical axes. In addition, the DOS of the AlB_2 bulk, surface and larger nanowire models are shown in Fig 6. Moreover the band structure of larger nanowire models is shown in Fig 6. The Fermi levels are also shifted as figures of simple nanowire models. In the pentagonal AlB nanowire, the band gap on the Fermi level is seen in Fig. 5(a). Hence this indicates that AlB pentagonal nanowire has different conductive property from AlB_2 bulk structure. On the other hands, DOS and band structure of AlB hexagonal nanowire in Fig. 5(b) is metallic. Moreover the DOS and band structure of AlB_2 surface and larger hexagonal nanowire are shown in Figs. 6(a)-(c). In Al pentagonal nanowire model, DOS and band structure is metallic.

Next, to study electronic state of the simple nanowire models in detail, the electron density, the kinetic energy density, tension density and stress tensor density are calculated. The electron density on the xz-plane and xy-plane are shown in Fig. 7. Fig. 7(a), (b), (d), (e), (g), and (h) are the sum of the occupied states and Fig. 7(c), (f) and (i) are the highest occupied state. Fig. 7(a), (d) and (g) show electron density on xy-plane and the other figures show that of xz-plane. In Fig. 8, the kinetic energy density and the tension density is shown. Fig. 8(a), (b), (d), (e), (g) and (h) are the sum of the occupied states and Fig. 8(c), (f) and (i) are the highest occupied state. The tension density is normalized. Fig. 8(a), (d) and (g) show the kinetic energy density and tension density on xy-plane and the other figures show those of xz-plane. Fig. 9 shows the largest eigenvalue and eigenvector of stress tensor density. The eigenvector is normalized. Fig. 9(a),(c), and (e) show stress tensor density on xy-plane and the other figures show that of xz-plane.

First, we discuss the pentagonal AlB nanowire. In Fig. 7(a) and (b), the electron density between B atoms is high. It shows that B atoms are bonded each other. It is seen from Fig. 7(c) that the electron density of the highest occupied state concentrates on B atoms rather than on Al atoms. The highest occupied state B($2s2p$) appears on the direction perpendicular to the wire axis like dangling bonds. Hence, it is seen that it makes bonds not along the wire axis but between B atoms on the five-membered ring. Therefore, in the pentagonal AlB nanowire, electrons cannot move along the nanowire axis like free electrons. Moreover, it can be speculated that this concentrated electron density affects H atom adsorption. This tendency is also seen in the kinetic energy density and tension density. In Fig. 8(a) and (b), the kinetic energy density concentrate between B atoms and in Fig. 8(c) the kinetic energy density of the highest occupied state concentrate on the direction perpendicular to the wire axis like dangling bonds. In Fig. 9(a) and (b), the largest eigenvalue and the eigenvector are shown. The red (blue) region means the positive (negative) eigenvalue of the stress tensor density. The positive stress is seen between B atoms and spindle structure is seen in the same region. This means B−B bond has the covalent property.

Properties of the hexagonal AlB nanowire are similar to those of the pentagonal one as seen in Fig. 7, Fig. 8 and Fig. 9. However, in the hexagonal one, the highest occupied state B($2s2p$) appears not only on the direction perpendicular to the wire axis. It appears around B atoms, which is in contrast with that of the pentagonal one. The interaction of these atomic orbitals is weak, and hence narrow band appears near the Fermi level as seen in Fig. 5(b). However, electrons on the narrow band are not conductive, since electrons concentrates on B($2s2p$) hybridized orbitals and heavy effective masses are understood from the DOS and band structure. Thus, the motion of electrons is also constrained only on the atoms, and hence this nanowire is expected not to have the conductivity as the pentagonal one.

Next, we consider the pentagonal Al nanowire. The band structure shows metallic properties as shown in Fig. 5(c). In the Al nanowire, the electron density and the positive kinetic energy density region is observed in the whole Al nanowire (Fig. 7 and Fig. 8(g)−(i)). Hence, it is expected that electrons can be accelerated by the external fields and escape from the constraint of atomic nuclei. Therefore, it can be concluded that Al nanowire has conductivity. The largest eigenvalue is almost negative on the xz-plane and xy-plane. This shows metallic bond between Al atoms. In Al nanowire models, electrons of HOMO state are not localized. Thus it can be speculated that AlB nanowire has different hydrogen adsorption property.

III-ii Hydrogen adsorption on AlB nanowires

Hydrogen adsorption site and energy

In this section, hydrogen adsorption on the nanowires is discussed. Total energy is calculated to find out the stable adsorption point of a H atom on the nanowires. Three adsorption points, sites 1, 2, and 3, as shown in Fig. 10 are considered. First, the geometries of the nanowires are fixed for the calculation of total energy. The stabilization energy $\triangle E$ is defined as

$$\triangle E = E(\text{nanowire} + \text{H}) - \{E(\text{nanowire}) + E(\text{H})\}. \tag{4}$$

The results of $\triangle E$ are shown in Table 1. In these results, the stabilization energy is the lowest on site 1 for all models. Therefore, a H atom is adsorbed on the top of B (Al) atoms. In the following, we only consider the hydrogen adsorption on the top of Al or B of the ring layer.

Next we consider the adsorption of H_2 molecules. The number of H atoms is even, and therefore the following definition of the adsorption energy is used,

$$\triangle E = \frac{E(\text{nanowire} + N \times \text{H}_2) - E(\text{nanowire}) - N \times E(\text{H}_2)}{N}, \tag{5}$$

where N is the number of H_2 in the system. The results are shown in Table 2. $\triangle E$ is calculated on the condition that hydrogen is adsorbed on all adsorption sites as shown in Fig. 11. The radius of B ring, r_1, and the distance between B and H, r_2, are investigated as geometric parameters with keeping their symmetry of nanowires (Fig. 11). In the case of the pentagonal AlB nanowire and H atoms, r_1 and r_2 are determined at 1.47 Å and 1.20 Å, respectively. In this structure, the bond length between B atoms on the same ring is 1.73 Å and that between B and Al atoms is 2.50 Å. The stabilization energy $\triangle E$ is -2.14 eV. In the hexagonal AlB nanowire, r_1 (r_2) are 1.68 (1.20) Å, the length between

B (B and Al) atoms is 1.68 (2.34) Å, and the stabilization energy $\triangle E$ is -2.10 eV. In both models, the bond lengths between B atoms on the same ring are longer than those of AlB nanowire without H atoms. The stabilization energy is below -2.0 eV. On the other hand, in the case of Al nanowire, the bond length between Al atoms on the same ring is 2.76 Å, which is shorter than Al nanowire without H atoms. The stabilization energy is -0.5 eV. Therefore, AlB nanowires are also more stable than Al nanowire for hydrogen adsorption. This difference of the hydrogen adsorption energy comes from the effect of the stabilization of the localized electron in HOMO. Since the adsorption energy of a H_2 molecule adsorption is -1.83 eV in the AlB_2 bulk surface model 1 and -1.12 V in the surface model 2 in the case of AlB_2, these results mean that AlB nanowires are more stable than AlB2 bulk surface for hydrogen adsorption.

Electronic structure

The DOS and band structure of AlB and Al simple nanowires after H adsorption are shown in Fig. 12. The DOS of AlB_2 bulk surface models after hydrogen adsorption are shown in Fig. 13. The DOS and band structure of all models are metallic. In both AlB simple nanowires, the state on the Fermi level consists of narrow band. Thus the conductivity of AlB simple nanowire is different from the AlB_2 bulk and surface.

The electron density on the xz-plane and xy-plane are shown in Fig. 14. Figs. 14(a), (b), (d), (e), (g), and (h) are the sum of the occupied states and (c), (f) and (i) are the highest occupied state. Figs. 14(a), (d), and (g) show electron density on xy-plane and the other figures show that of xz-plane. In Fig. 15, the kinetic energy density and the tension density is shown. Figures 15(a), (b), (d), (e), (g), and (h) are the sum of the occupied states and (c), (f) and (i) are the highest occupied state. The tension density is normalized. Figs. 15(a), (d), (g) show the kinetic energy density and tension density on xy-plane and the other figures show those of xz-plane. Fig. 16 shows the largest eigenvalue and eigenvector of stress tensor density on xy-plane and the other figures show those of

xz-plane. The eigenvector is normalized.

First, we discuss the pentagonal AlB nanowire. After the hydrogen adsorption on the pentagonal AlB nanowire, the sum of the electron density in Figs. 14(a) and (b) appear between B and H. In the highest occupied state (Fig. 14(c)), the electron density also appears around H atoms. In the kinetic energy density (Fig. 15(a)-(c)), the sum of the all occupied states shows the same tendency in the electron density. The kinetic energy density regions with negative kinetic energy density for the highest occupied state appear at the center of the five-membered ring. This means that the highest occupied state consists of H states. Thus the peak around the Fermi level in the DOS figure is the electron related with B−H bonds. In Fig. 16(a) and (b), the positive region and the spindle structure are seen between B and H and between B atoms on the same ring. This means that the both bonds are the covalent bond. The AlB hexagonal nanowire similar properties to the pentagonal model as seen in Figs. 12, 14-16.

In Al nanowire, it is seen in Fig. 12 the DOS of Al nanowire on the Fermi level is changed by the hydrogen adsorption. The electron density of the sum of the all occupied state is high around H atoms. In the highest occupied state, the electron density and the kinetic energy density are localized between Al and H and between atoms on the axis. This is different from the electron density before the hydrogen adsorption. In Figs. 16(e) and (f), the positive region and the spindle structure are seen between Al and H and the negative region is seen between Al atoms. This means that the Al-H bond is the covalent bond and Al−Al bond is metallic.

IV Conclusion

We performed first-principles calculations for AlB nanowires to study the transitions of their electronic structures caused by H atoms adsorption. The difference between AlB nanowires and Al nanowire is clearly seen in the electron density and energy density. The electron of the highest occupied state appears on the direction perpendicular to the wire axis like dangling bonds. Therefore, it can be concluded that the AlB nanowires do not have the conductivity, while AlB_2 bulk has it. It can be also seen that AlB nanowires are more stable in the hydrogen adsorption. After the hydrogen adsorption occurred, H atoms make the covalent bond with B and Al. There is no significant difference of the electron density between the hexagonal AlB nanowire and the pentagonal within this work. The DOS of the Al nanowire on the Fermi level is decreased by the H adsorption. We have confirmed that conductivity of AlB nanowires are unchanged with hydrogen adsorption as seen from the electron density and the energy density. The hydrogen adsorption energy of AlB nanowire models is larger than that of Al nanowire. In this point, AlB nanowire is more stable in the hydrogen adsorption.

Reference

[1] H. Nakano, H. Ohta, A. Yokoe, K. Doi, and A. Tachibana, J. Pow. Sour. **163**, 125 (2006).

[2] A. Goldberg and I. Yarovsky, Phys. Rev. B **75**, 195403 (2007).

[3] H. Cheng, A. C. Cooper, and G. P. Pez, J. Am. Chem. Soc. **123**, 5845 (2001); L. Chen, A. C. Cooper, G. P. Pez, and H. Cheng, J. Phys. Chem. C, **112**, 1755 (2008).

[4] T. Makita, K. Doi, K. Nakamura, and A. Tachibana, J. Chem. Phys. **119**, 538 (2003).

[5] Y. Kawakami, Y. Nojima, K. Doi, K. Nakamura, and A. Tachibana, Electrochim. Acta **50**, 739 (2004).

[6] M. Suzuki, K. Nagai, S. Kinoshita, K. Nakajima, K. Kimura, T. Okano, and K. Sasakawa, Appl. Phys. Lett. **89**, 133103 (2006).

[7] A. Tachibana, J. Chem. Phys. **115**, 3497 (2001).

[8] A. Tachibana, in Stress Induced Phenomena in Metallization, edited by S. P. Baker (American Institute of Physics, New York, 2002), pp.105-116.

[9] A. Tachibana, in Fundamental Perspectives in Quantum Chemistry: A Tribute to the Memory of Per-Olov Löwdin, edited by E. Brändas, and E. Kryachko (Kluwer Academic, Dordrecht, 2003), Vol. II, pp.211-239.

[10] A. Tachibana, Int. J. Quantum Chem. Symp. **21**, 181 (1987).

[11] A. Tachibana and R. G. Parr, Int. J. Quantum Chem. **41**, 527 (1992).

[12] A. Tachibana, Int. J. Quantum Chem. **57**, 423 (1996).

[13] A. Tachibana, Theor. Chem. Acc. **102**, 188 (1999).

[14] I. Loa, K. Kunc, and K. Syassen, Phys. Rev. B **66**, 134101 (2002).

[15] Periodic Regional DFT program package, ver.2, (Tachibana Lab., Kyoto Univ., Kyoto, 2002).

[16] D. R. Hamann, Phys. Rev. B **40**, 2980 (1989).

[17] J. P. Perdew and Y. Wang, Phys. Rev. B **45**, 13244 (1992).

[18] M. J. Frisch et al., Gaussian 03, Revision B.05, Gaussian, Inc., Pittsburgh PA 2003.

[19] G. te Velde, F. M. Bickelhaupt, S. J. A. van Gisbergen, C. Fonseca Guerra, E. J. Baerends, J. G. Snijders, and T. Ziegler, J. Comput. Chem. **22**, 931 (2001).

Table 1: The geometry parameters of nanowiremodels and AlB_2 bulk

	Site 1	Site 2	Site 3
AlB Pentagonal	-5.53 [eV]	-3.54 [eV]	-
AlB Hexagonal	-5.65 [eV]	-4.53 [eV]	-
Al pentagonal	-3.59 [eV]	-3.34 [eV]	-3.37 [eV]

Table 2: Geometry parameters and the stabilization energy of H_2 molecule adsorption

	r_1 (Å)	r_2 (Å)	ΔE(eV)
AlB Pentagonal	1.47	1.20	-2.14
AlB Hexagonal	1.68	1.20	-2.10
Al Pentagonal	2.35	1.57	-0.50
AlB Surface 1	-	-	-1.84
AlB Surface 2	-	-	-1.12

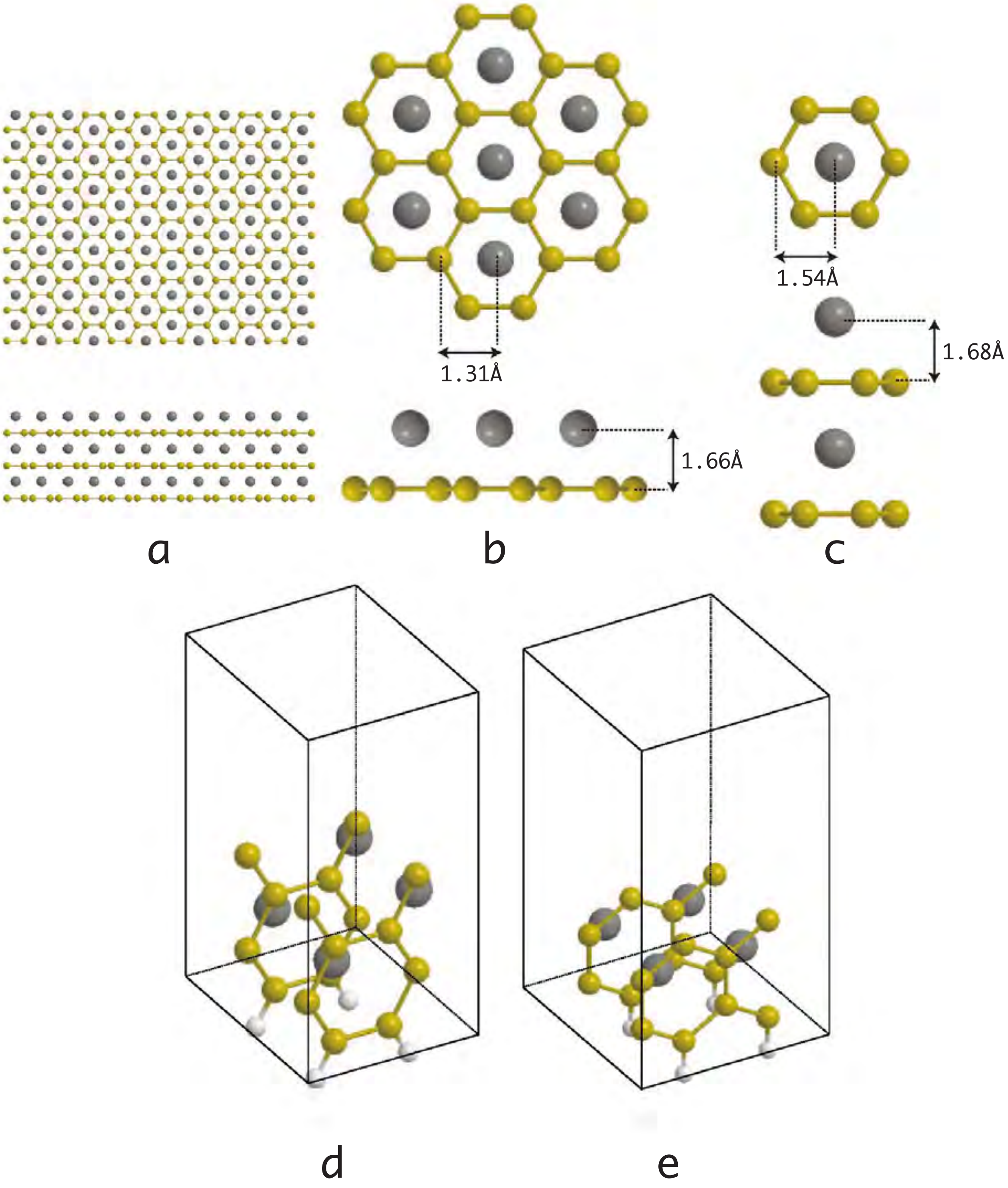

Figure 1: (a) AlB_2 bulk model, (b) AlB larger hexagonal nanowire model, (c) AlB hexagonal nanowire model, (d) AlB_2 bulk surface model 1, (e) AlB_2 bulk surface model 2.

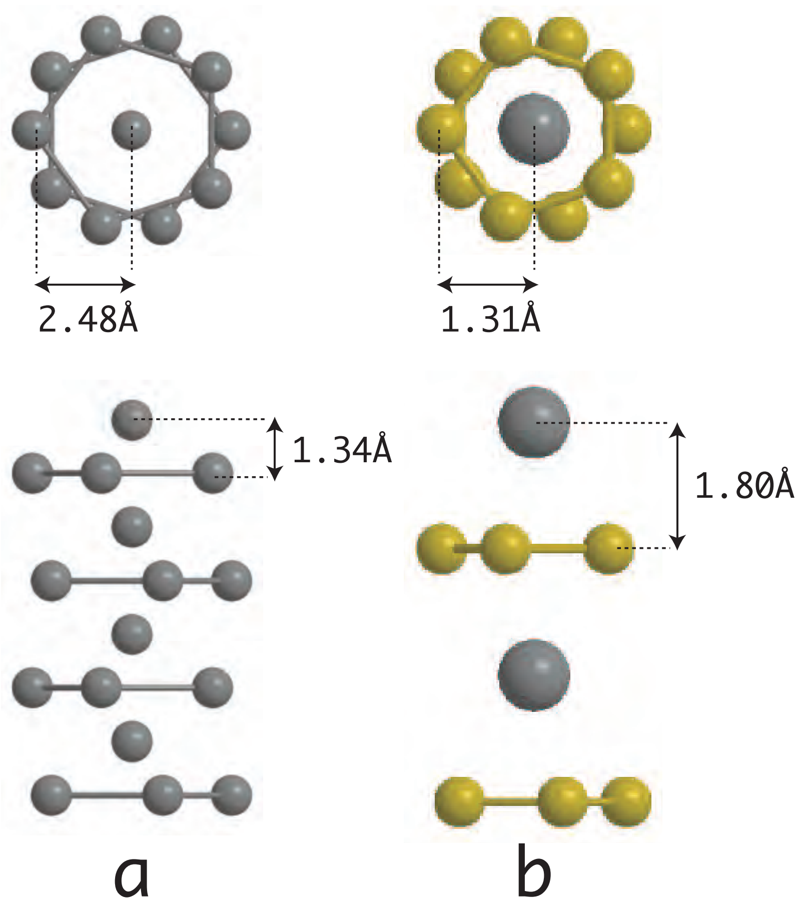

Figure 2: (a) Al pentagonal nanowire model, (b) AlB pentagonal nanowire model.

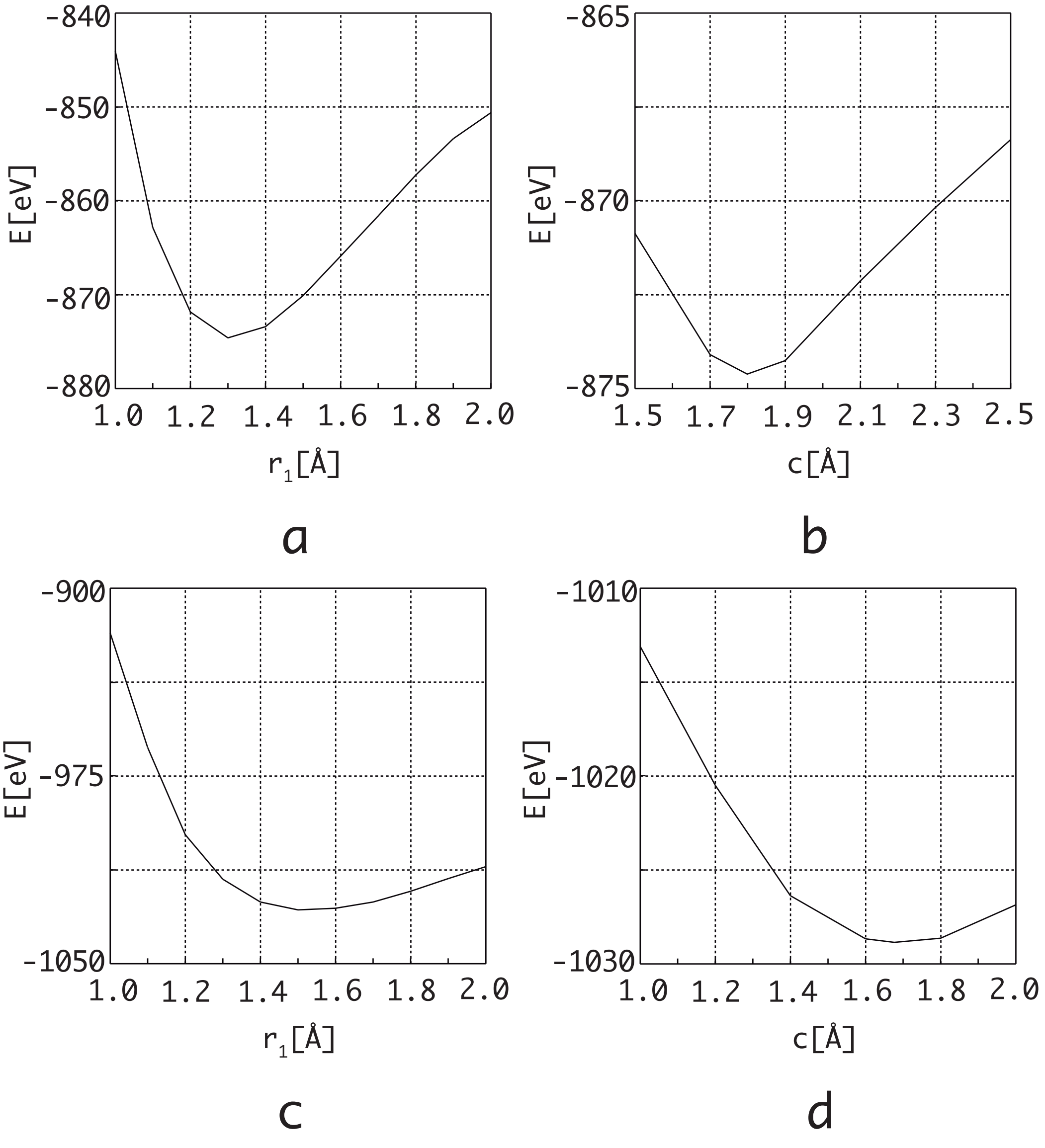

Figure 3: Total energy curves. (a) AlB pentagonal nanowire model as a function of r_1, (b) AlB pentagonal nanowire model as a function of c. (c) AlB hexagonal nanowire model as a function of r_1. (d) AlB hexagonal nanowire model as a function of c.

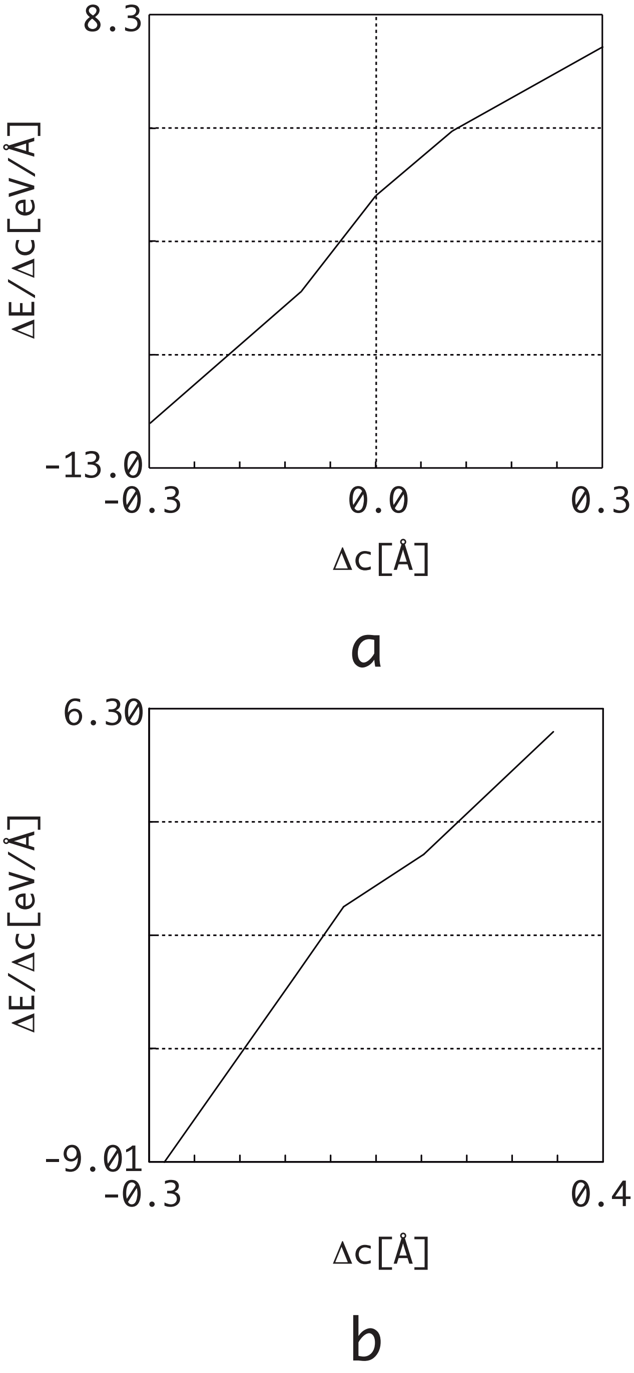

Figure 4: Total $\triangle E/\triangle c$ as a function of $\triangle c$. (a) AlB pentagonal nanowire model, (b) AlB hexagonal nanowire model.

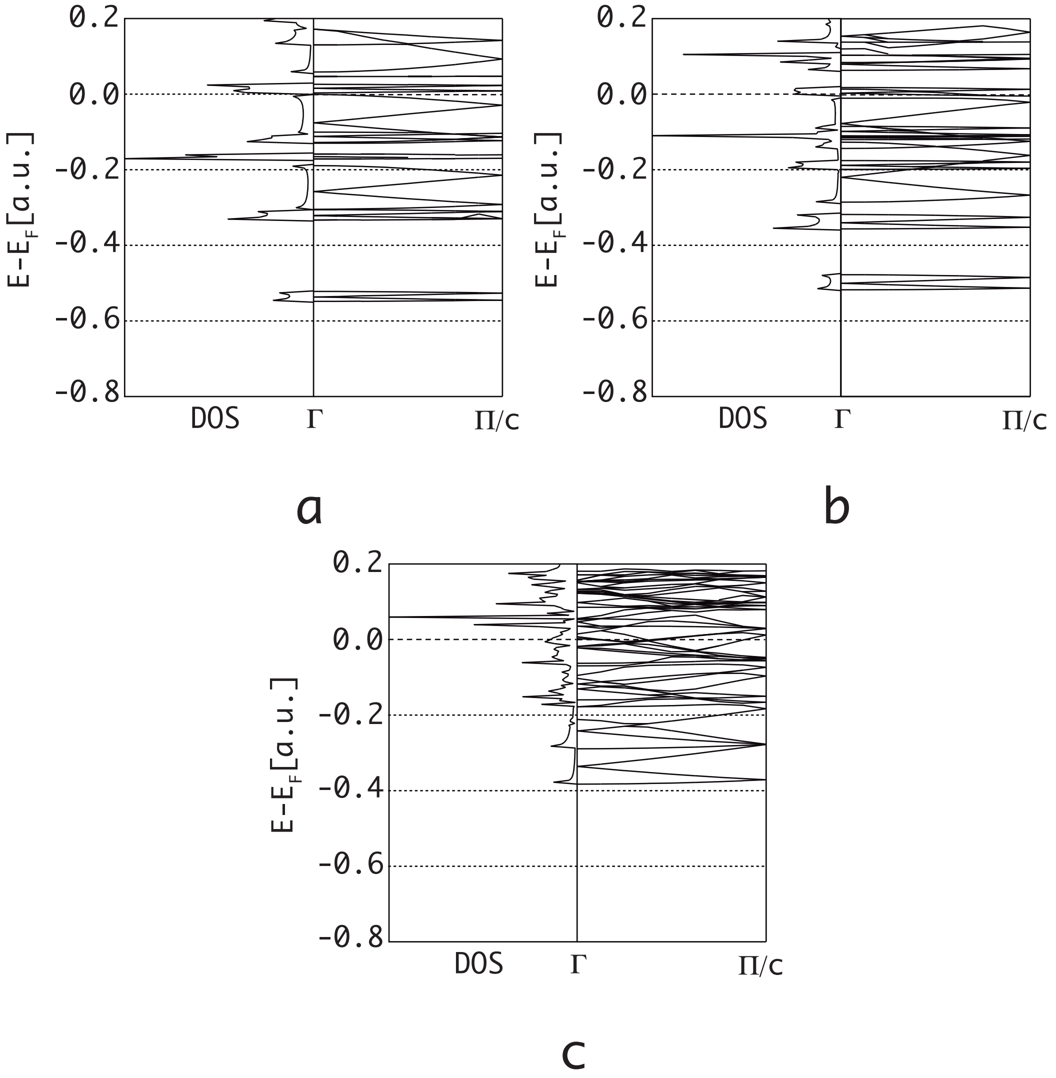

Figure 5: DOS and band structure of AlB nanowire model. (a) AlB pentagonal nanowire model, (b) AlB hexagonal nanowire model, (c) Al pentagonal nanowire model.

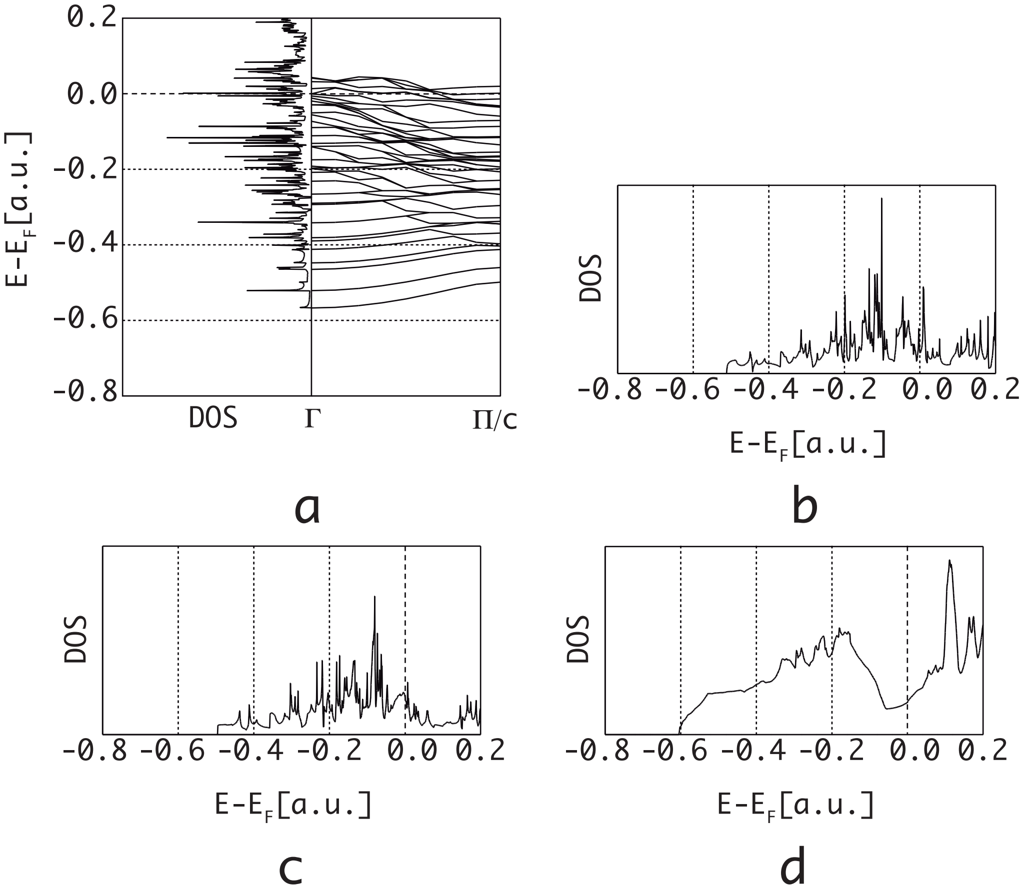

Figure 6: DOS and band structure of AlB lager hexagonal nanowire model and DOS of AlB_2 bulk and bulk surface. (a) AlB larger hexagonal nanowire model, (b) AlB_2 surface model 1, (c) AlB_2 surface model 2, (d) AlB_2 bulk model.

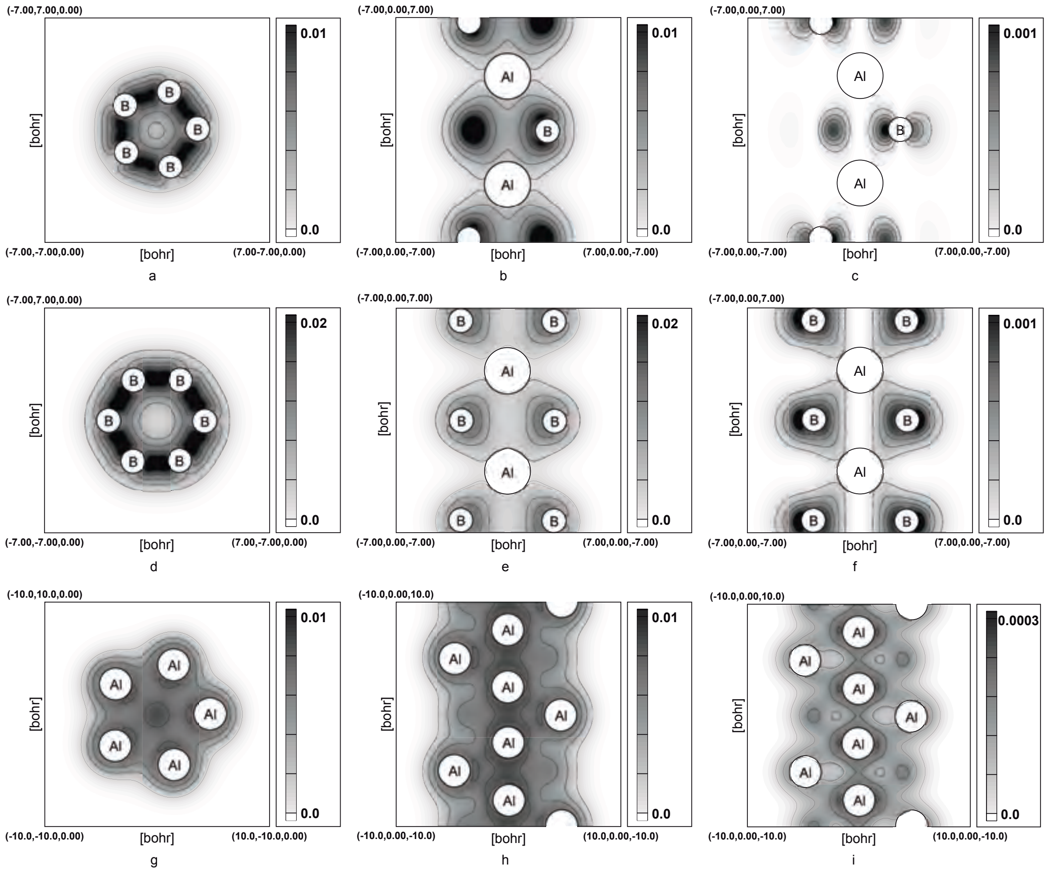

Figure 7: Electron density of nanowire models. The region in the circle is pseudopotential. Electron density of the sum of all occupied states in (a) and (b) AlB pentagonal, (d) and (e) AlB hexagonal, and (g) and (h) Al pentagonal nanowire models. Electron density of the highest occupied states (c) AlB pentagonal, (f) AlB hexagonal and (i) Al pentagonal nanowire models.

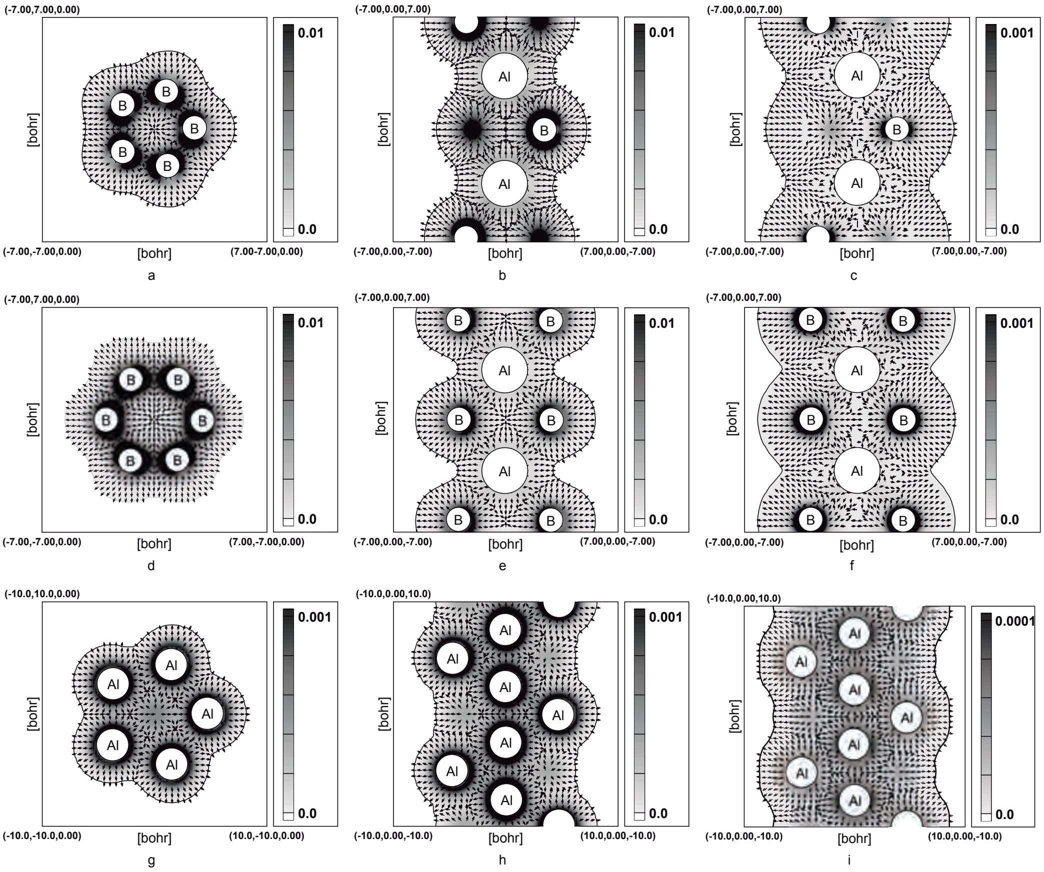

Figure 8: Kinetic energy density and tension density of nanowire models. The region in the circle is pseudopotential. The tension density is showed only on the region where the kinetic energy is positive. Kinetic energy density and tension density of the sum of all occupied states in (a) and (b) AlB pentagonal, (d) and (e) AlB hexagonal, and (g) and (h) Al pentagonal nanowire models. Light (dark) gray region means positive (negative) kinetic energy density. Kinetic energy density and tension density of the highest occupied states (c) AlB pentagonal, (f) AlB hexagonal, and (i) Al pentagonal nanowire models.

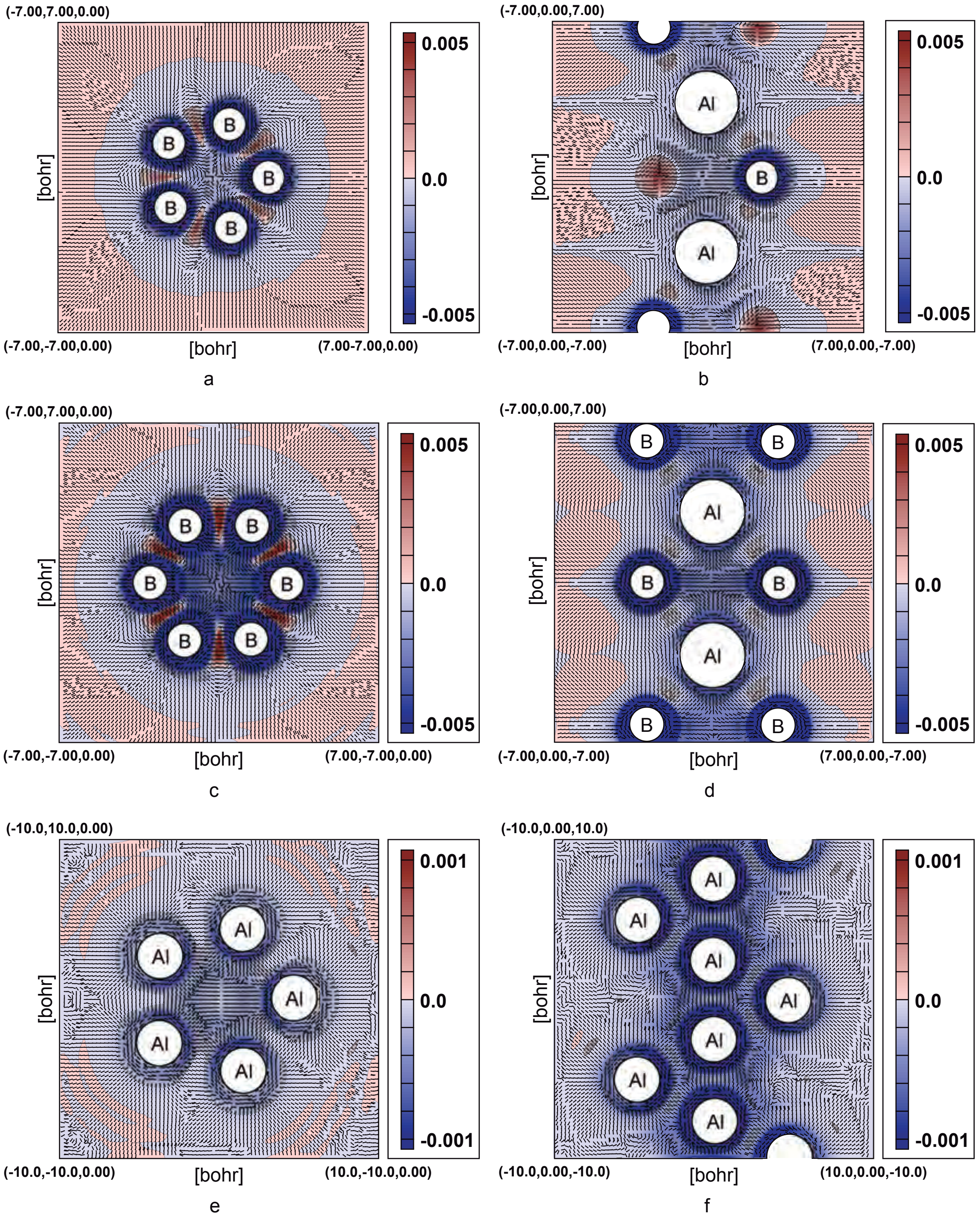

Figure 9: The largest eigenvalues of stress-tensor density. Red (blue) region means positive (negative) stress density. The eigenvectors are normalized. The largest eigenvalues and eigenvectors of stress-tensor density in (a) and (b) AlB pentagonal, (d) and (e) AlB hexagonal, and (g) and (h) Al pentagonal nanowire models.

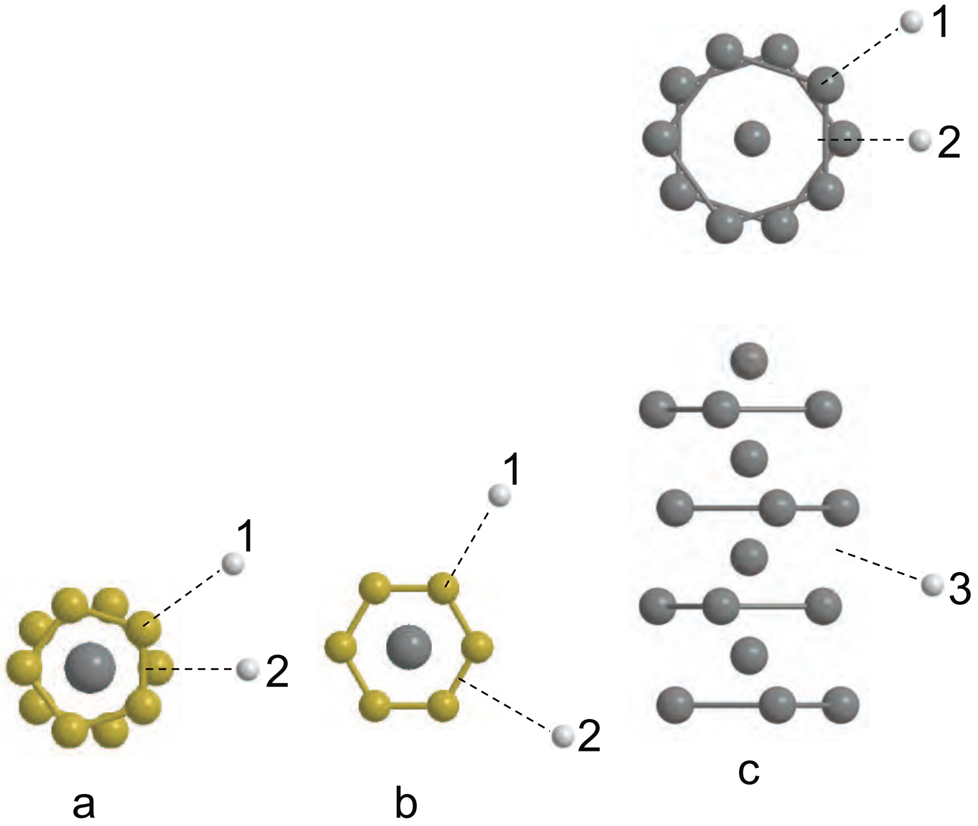

Figure 10: H atom adsorption site. (Site 1) The top of B(Al) ring. (Site 2) The same distance from B(Al) atoms of the same ring. (Site 3) The same distance from B(Al) atoms of the different rings.

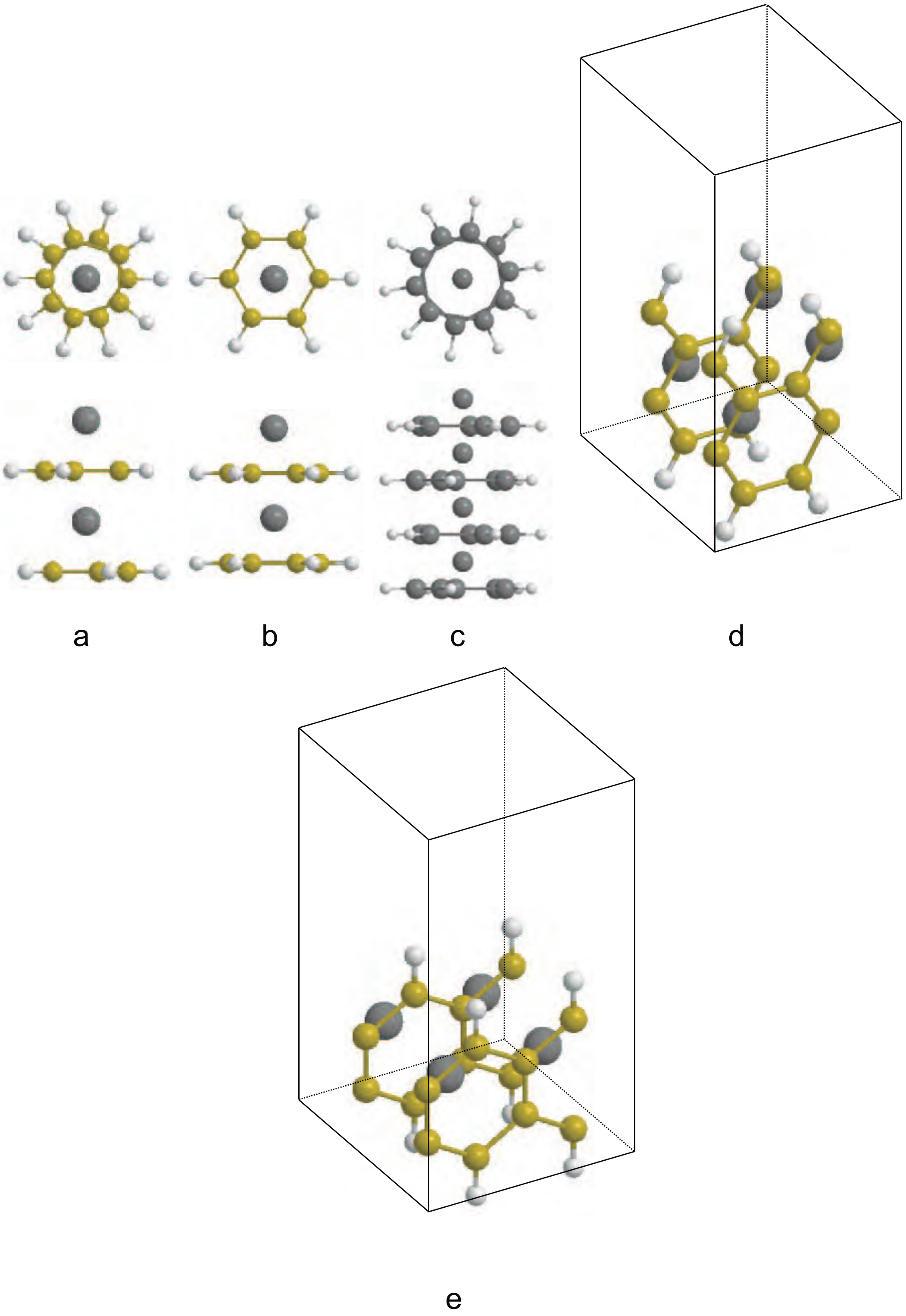

Figure 11: H absorbed simple nanowire models and AlB_2 surfaces. (a) AlB pentagonal nanowire model. (b) AlB hexagonal nanowire model. (c) Al pentagonal nanowire model. (d) AlB_2 surface model 1. (e) AlB_2 surface model 2.

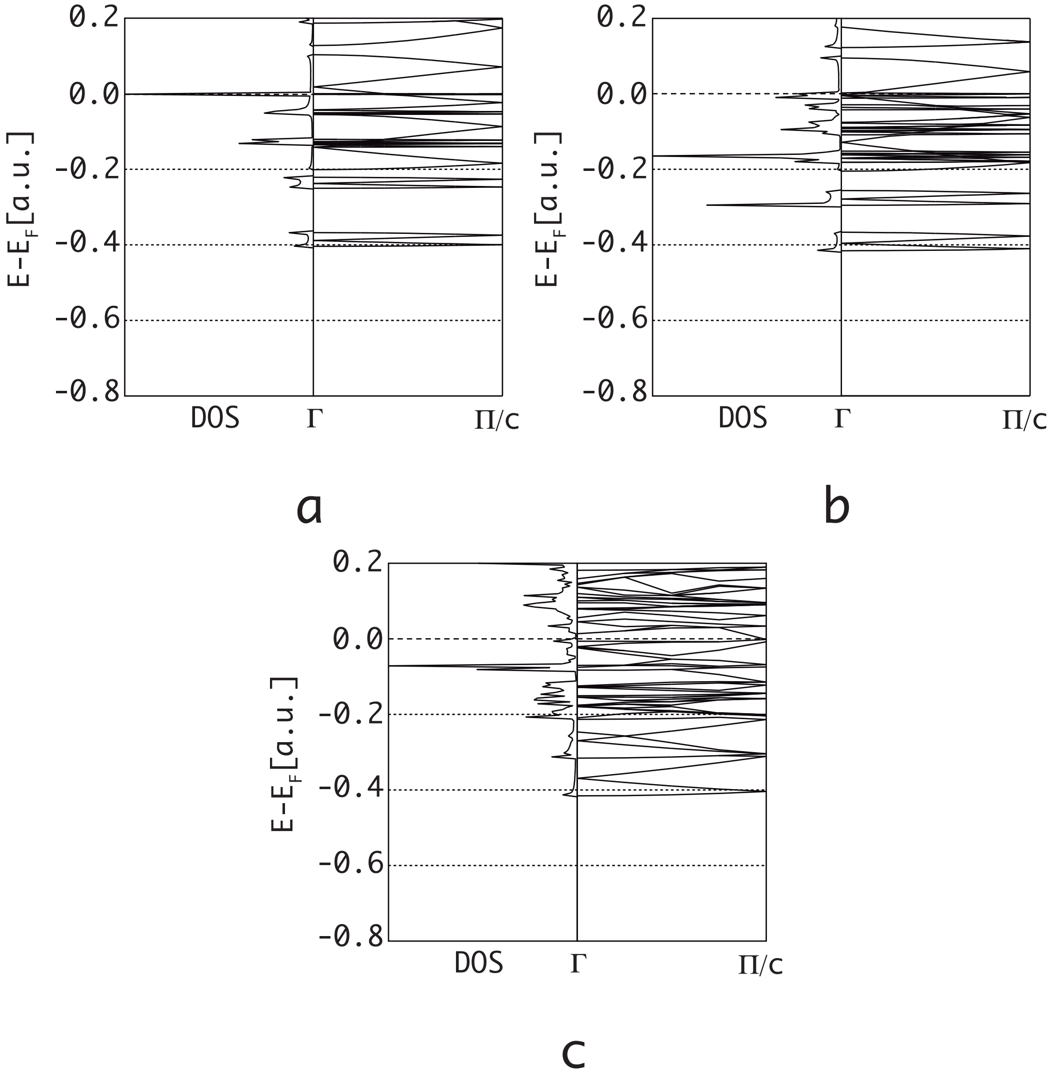

Figure 12: Total DOS and band structure of nanowire models after H adsorption. (a) AlB pentagonal nanowire model. (b) AlB hexagonal nanowire model. (c) Al pentagonal nanowire model.

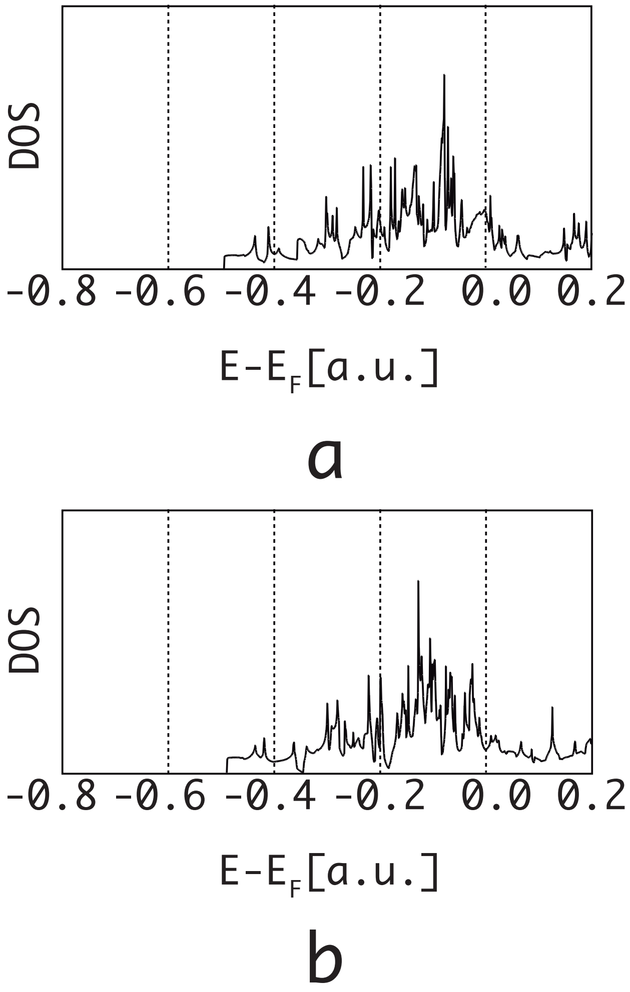

Figure 13: Total DOS of surface models after H adsorption. (d) AlB_2 surface model 1. (e) AlB_2 surface model 2.

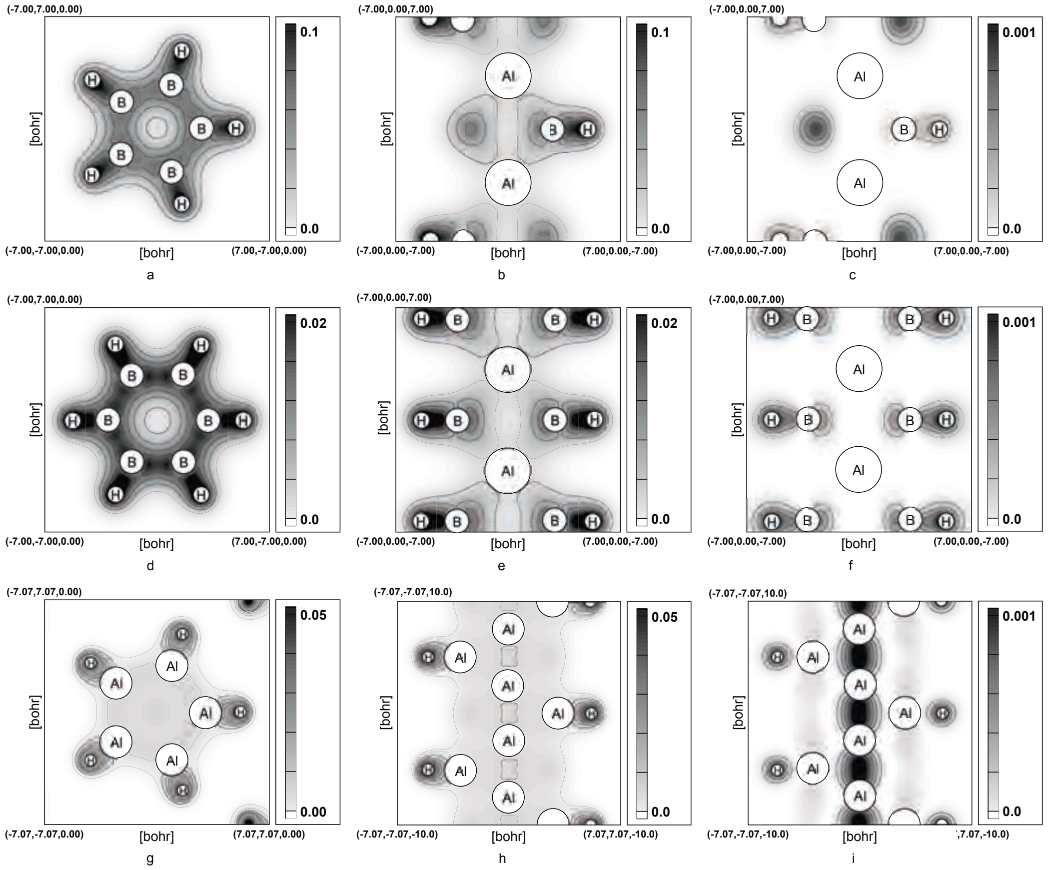

Figure 14: Electron density of nanowire models after H adsorption. The region in the circle is pseudopotential. Electron density of the sum of all occupied states in (a) and (b) AlB pentagonal, (d) and (e) AlB hexagonal, and (g) and (h) Al pentagonal nanowire models. Electron density of the highest occupied states (c) AlB pentagonal, (f) AlB hexagonal and (i) Al pentagonal nanowire models.

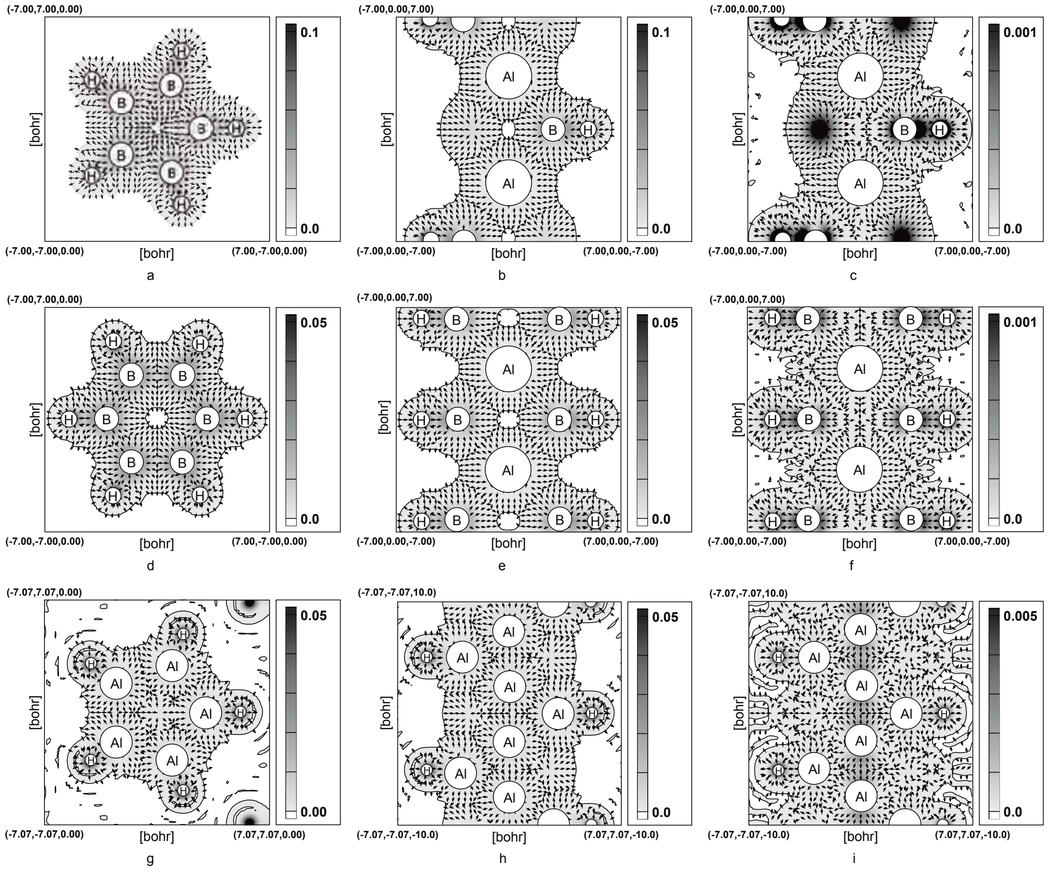

Figure 15: Kinetic energy density and tension density of nanowire models after H adsorption. The region in the circle is pseudopotential. The tension density is showed only on the region where the kinetic energy is positive. Kinetic energy density and tension density of the sum of all occupied states in (a) and (b) AlB pentagonal, (d) and (e) AlB hexagonal, and (g) and (h) Al pentagonal nanowire models. Light (dark) gray region means positive (negative) kinetic energy density. Kinetic energy density and tension density of the highest occupied states (c) AlB pentagonal, (f) AlB hexagonal, and (i) Al pentagonal nanowire models.

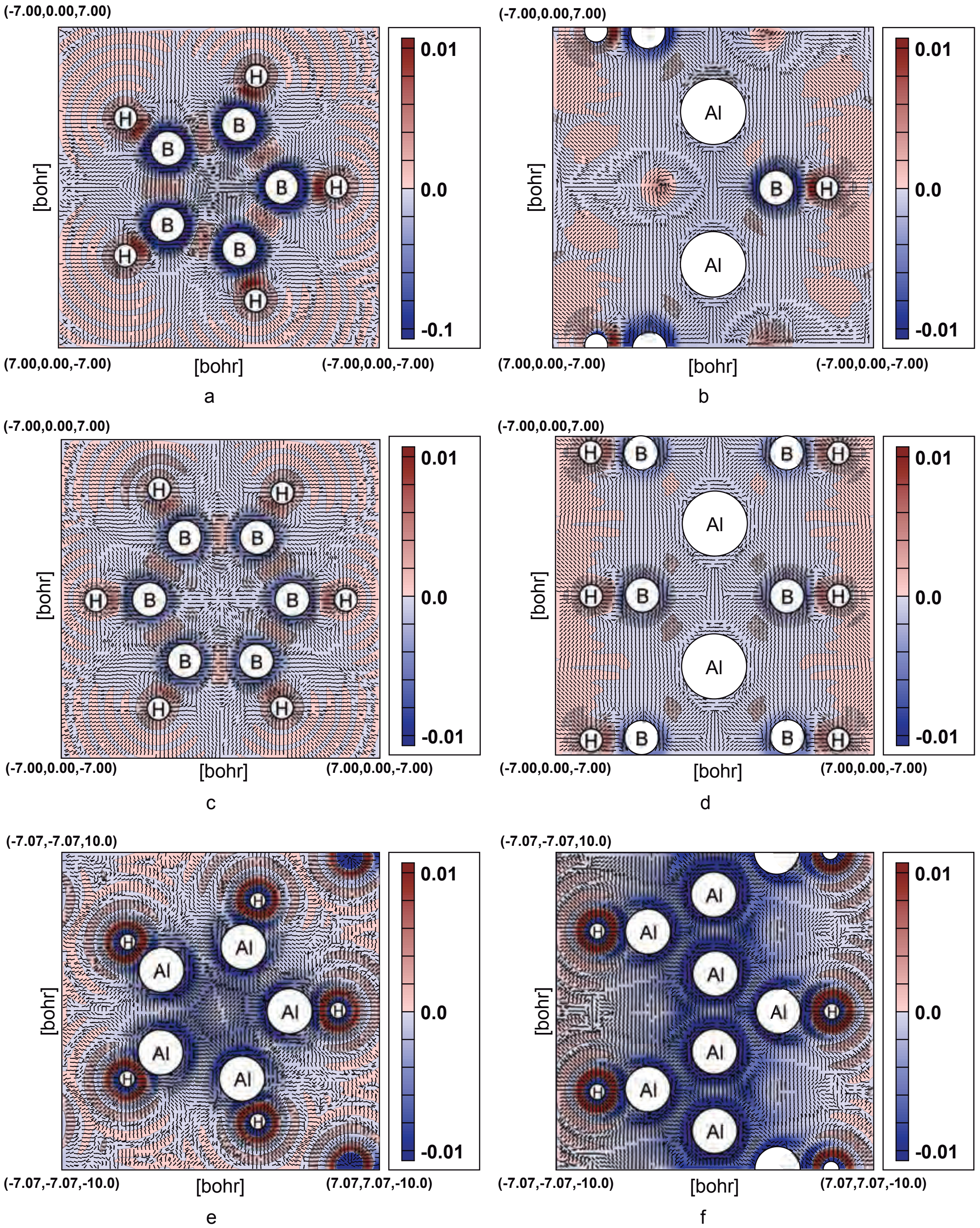

Figure 16: The largest eigenvalues of stress-tensor density. Red (blue) region means positive (negative) stress density. The eigenvectors are normalized. The largest eigenvalues and eigenvectors of stress-tensor density in (a) and (b) AlB pentagonal, (d) and (e) AlB hexagonal, and (g) and (h) Al pentagonal nanowire models.

Chapter 2

Theoretical study of the migration of the hydrogen atom adsorbed on aluminum nanowire

I Introduction

Recently, the development of experimental methods allows us to fabricate nanostructures experimentally. In these nanostructures, nanowire and nanotube, which have periodicity along one dimension, have remarkable characters compared with bulk system. In particular, nanowires are fabricated for various species of atoms, and hence it attracts much attention theoretically and industrially [1–15]. Nanowire has high ratio of surface area to its mass and therefore it is considered that nanowire structures are good candidates for hydrogen storage material which is a key ingredient for hydrogen energy system. Among various species of metal atoms, the aluminum atom exists abundantly on the earth and is available easily. Hydrogen storage material should have higher weight percent storage ability so that hydrogen energy is comparable with fossil fuel. The aluminum atom has also smaller mass than those of most metal atoms. Therefore aluminum nanowire is a promising material for hydrogen storage.

From this viewpoint, we study aluminum nanowire in this work following previous works in our laboratory. Makita et al. showed stable geometries of aluminum nanowires based on Au nanowire [5]. Kawakami et al. showed that a hydrogen molecule is adsorbed on a pentagonal aluminum nanowire model as two separate hydrogen atoms [8]. Nakano et al. suggested to wrap aluminum species in carbon materials such as carbon nanotube to enhance the hydrogen adsorption on their surfaces [11]. In addition, geometry and hydrogen adsorption energy for AlB nanowire whose structure was based on aluminum nanowire was reported [15]. The aluminum nanowire with pentagonal ring is studied in this work following these works, since this structure is stable and has high ratio of surface area to the density.

A hydrogen atom is stabilized by about -3.6 eV after the adsorption on the nanowire [15]. Hence, it is not easy task to detach the adsorbed hydrogen atom from the nanowire. The hydrogen atom has high barrier for the direction perpendicular to the nanowire and the motion to the direction is not unlikely, and nevertheless hydrogen atoms may move along the nanowire. Therefore, in this work, we focus on the dynamics of hydrogen and deuterium atoms adsorbed on the aluminum nanowire. We calculate potential energy surface (PES) of a hydrogen atom adsorbed on the pentagonal aluminum nanowire. Using this result, we discuss the behavior of a hydrogen atom on the nanowire. Particularly, we compare the activation energies of the hydrogen move toward angular and axial directions. In addition, we focus on quantum effects of a hydrogen atom. We also study those of a deuterium atom for comparison. Since their masses are small, quantum effects, such as large zero-point vibrational energy and non-localization, are important for these atoms [13, 16, 17]. These phenomena affect the adsorption and activation energy of hydrogen and deuterium atoms. We calculate the wave functions of hydrogen and deuterium atoms with our PES. We also perform quantum energy density analysis, which is proposed by one of the authors, to discuss the surface of aluminum nanowire from a new physical viewpoint [16].

II Computational Details

Total energy and electronic structure calculations are carried out based on density functional theory (DFT) with the projector augmented wave method by the Vienna ab initio simulation package [19, 20]. Electron wave functions are expanded by plane wave basis sets and the kinetic energy cut off is set to 250 eV. The exchange-correlation functional we used in this calculation is the generalized gradient approximation of Perdew, Burke, and Ernzerhof [21]. All calculations are carried out in the spin-polarized condition.

We show an aluminum nanowire model used in this study in fig. 1. The radius of nanowire (R) and the distance between an aluminum pentagonal ring and an aluminum atom on the axis (D) are derived as 2.47 Å and 1.23 Å, respectively, from the optimization calculation. The differences from those of our previous papers are arisen from the difference of program code [1, 15]. The boundary condition of this nanowire model is imposed as periodic one. In our calculation, 15.0 Å × 15.0 Å × $8D$ Å super cell is taken for all electronic structure calculations. This cell has a large enough vacuum region so that the interaction with next cells is negligible. The number of aluminum atoms in the unit cell is counted as twenty-four. A $1 \times 1 \times 4$ k-point set is used to sample the Brillouin zone. For the density of state (DOS) calculations, a $1 \times 1 \times 51$ k-point set is adopted.

This model has pentagonal rings whose angles are different by $\pi/5$ from each other. For the PES calculation, the position of the hydrogen atom is parametrized in a cylindrical coordinate system taking the symmetry of the nanowire model into account. We can reduce the number of points in the PES calculation along axial and angular directions. The parameters of the hydrogen coordinate are taken as shown in fig. 1, and their ranges are given as follows,

$$0 \leq \rho \leq R_D, \tag{1}$$

$$0 \leq \theta \leq \frac{\pi}{5}, \tag{2}$$

$$0 \leq z \leq 1.23\text{Å}. \tag{3}$$

Here a new radial constant R_D is taken as $R_D = R + 2.50 = 4.97$ Å. Once energies are calculated only for this region, the PES for the required region can be derived. The adsorption energy (ΔE) is defined as follows,

$$\Delta E = E_{\mathrm{NW+H}} - E_{\mathrm{NW}} - E_{\mathrm{H_2}}/2, \tag{4}$$

where E_{X} means the total energy of the system X. The definition of ΔE is calculated for the hydrogen molecule instead of the hydrogen atom for comparison with other works. At the dissociation limit, the adsorption energy in this system is 2.24 eV. In the calculation of the PES, the deformation of the nanowire is not taken into account, since the motivation of this work is the study of the dynamics of hydrogen and deuterium atoms on the nanowire. The aluminum atom is much heavier than the hydrogen atom. Hence, the motion of the aluminum atom is negligible during the motion of the hydrogen atom. The calculation mesh size of the radial direction is taken as 0.1 Å, that of the angular direction is $\pi/50$, and that of the axial direction is 0.123 Å.

For the calculation of the wave function of hydrogen and deuterium atoms, we solve the three dimensional Schrödinger equation. The PES calculated in this work is used as the potential term of this calculation. Periodic boundary conditions are imposed on axial and angular directions. For the radial direction, the boundary condition is given as,

$$\Psi_{\mathrm{H}}(R_D, \theta, z) = 0. \tag{5}$$

We choose R_D, instead of the infinity, as the boundary condition of the radial direction for simplicity. This choice of the boundary condition is sufficient for this work. The length of this unit cell in the axial direction is $4D$, which is half as long as that of the super cell used in electronic structure calculation. The wave function is expanded by plane wave and Bessel function basis sets as follows,

$$\begin{aligned}
\Psi_{\mathrm{H}}(\rho, \theta, z) &= \sum_{l,m,n} C_{lmn}\psi_{lmn}(\rho, \theta, z), && (6)\\
\psi_{lmn}(\rho, \theta, z) &= \frac{\sqrt{2}}{R_D J_{m+1}(x_{mn})} J_m\left(x_{mn}\frac{\rho}{R_D}\right)\\
&\times \frac{1}{\sqrt{2\pi}}\exp\left(im\theta\right)\\
&\times \frac{1}{\sqrt{4D}}\exp\left(il2\pi\frac{z}{4D}\right), && (7)
\end{aligned}$$

where J_m means the first kind Bessel function of order m and x_{mn} is the nth zero point of the Bessel function of order m. The expansion coefficient, C_{lmn}, is derived from the diagonalization of the Hamiltonian. Considering the symmetry of this model,

$$\Psi_{\mathrm{H}}(\rho, \theta + \pi/5, z + 2D) = \Psi_{\mathrm{H}}(\rho, \theta, z). \tag{8}$$

Accordingly, wave vectors of axis and radial directions can be given as,

$$m\frac{\pi}{5} + l2\pi\frac{2D}{4D} = 2N\pi \ (l, m, N = 0, \pm 1, \pm 2.....). \tag{9}$$

This equation is simplified to

$$m' + l = 2N \ (m' = 0, \pm 1, \pm 2.....), \tag{10}$$

$$m = 5m'. \tag{11}$$

In this calculation, the ranges of the parameters (n, m', l) are applied as follows,

$$n = 1, ..., 10, \tag{12}$$

$$m' = 0, \pm 1, \pm 2, \pm 3, \pm 4, \tag{13}$$

$$l = 0, \pm 1, ..., \pm 40. \tag{14}$$

Thus the number of the basis functions is 3730. In addition, $\psi_{nml}(\rho, \theta, z)$ is an orthogonal system,

$$\langle \psi_{nml} | \psi_{n'm'l'} \rangle = \delta_{nn'} \delta_{mm'} \delta_{ll'}. \tag{15}$$

The term of the kinetic energy can be calculated analytically,

$$\langle \psi_{nml} | K | \psi_{nml} \rangle = \frac{\hbar^2}{2m_X} \left[\left(\frac{x_{nm}}{R_D} \right)^2 + \left(l \frac{2\pi}{4D} \right)^2 \right], \tag{16}$$

where m_X means the mass of a hydrogen atom or a deuterium atom. The integration of the potential energy term is carried out using Gauss-Legendre method.

We analyze electronic states and properties using quantum energy density, which is proposed by one of the authors [16]. One of the quantity of the quantum energy density, the electronic kinetic energy density $n_T(\vec{r})$, is defined as

$$n_T(\vec{r}) = \frac{1}{2}\sum_i \nu_i \left\{ \left[-\frac{\hbar^2}{2m_e}\Delta\psi_i^*(\vec{r}) \right] \psi_i(\vec{r}) + \psi_i^*(\vec{r}) \left[-\frac{\hbar^2}{2m_e}\Delta\psi_i(\vec{r}) \right] \right\}, \tag{17}$$

where m_e is the mass of the electron, $\psi_i(\vec{r})$ is the ith natural orbital, and ν_i is the occupation number of $\psi_i(\vec{r})$. The electronic kinetic energy of the system is obtained by integration of kinetic energy density over the whole space. In classical mechanics, only positive kinetic energy is allowed, and however negative kinetic energy appears in quantum mechanics. This means that electrons can exist also in regions with the negative kinetic energy density with quantum effects. The surface of zero kinetic energy density can be interpreted as the boundary of a molecule.

In the calculation of the kinetic energy density, we use two program codes for each boundary condition, respectively. The electronic state is calculated by fhi98md program package [22] for the periodic system and Gaussian 03 program package [23] for the molecular system. The kinetic energy density is calculated based on these electronic states by Periodic Regional DFT (PRDFT) program package [24] for the periodic system and Molecular Regional DFT (MRDFT) program package [25] for the molecular system. The calculation of the nanowire model uses, of course, the periodic boundary condition. On the other hand, the calculation of the molecular system is also performed for the cluster system, Al_{13}, which has the same structure of a part of the nanowire. This calculation is for a comparison with the nanowire.

III Result and Discussion

III-i Electronic structure of aluminum nanowire model

Before the discussion of the migration of the hydrogen atom, we discuss the electronic structure and charge transfer of the nanowire model without and with the adsorbed hydrogen. In our previous paper, we have shown that electron density is higher for aluminum atoms on the axis compared to those of rings [15].

In fig. 2, we show total DOS (TDOS) and partial DOS (PDOS) of aluminum atoms of pentagonal rings and those on the axis for the aluminum nanowire model without the adsorbed hydrogen. The Fermi level is taken to be 0.0 eV shown as vertical dotted lines in figures. In both TDOS and PDOS, some peak structures are seen, which may be characteristic for one dimensional metallic nanowire. Comparing figs. 2(b) and (c), contributions from p and d orbitals are large for aluminum atoms on the axis in the low-energy region. This is because electron density is distributed along the axial direction as shown in our previous paper [15].

In fig. 3, we show TDOS of the nanowire model with the adsorbed hydrogen and PDOS of the aluminum atom adsorbed by the hydrogen atom, those on the axis, and those of the hydrogen atom. The Fermi level is taken to be 0.0 eV shown as vertical dotted lines in figures. Compared with fig. 2, the shape of the peak near the Fermi level in TDOS is modified significantly after the hydrogen adsorption. This modification originates in the aluminum atom adsorbed by the hydrogen atom as can be seen in the figure of its PDOS. The changes of TDOS and PDOS in the low energy region are not significant. PDOS of the hydrogen atom is distributed over wide range of the energy.

In order to study the electronic structure of these models, we study also the amount of charge transfer. We calculate the number of valence electrons for aluminum atoms on the ring and on the axis for the aluminum nanowire model without the adsorbed hydrogen atom. To do so, we use the PDOS in this work. These results are shown in table 1. Al(ring) means atoms on the pentagonal rings and Al(axis) means atoms on the axis. As seen in this table, the charge is transfered from pentagonal rings to the axis. In particular, electrons in p and d orbitals increase, while there is little difference for those of s orbital.

Next, we consider the charge transfer caused by the hydrogen adsorption. In this calculation, we consider that the hydrogen atom is adsorbed on the top site of the aluminum nanowire, which is the most stable site as shown in the next subsection. The results of the charge transfer is shown in table 2. In this table, Al(ring)$_1$ represents the aluminum atom on which the hydrogen is adsorbed, Al(ring)$_2$ represents aluminum atoms on pentagonal rings except for Al(ring)$_1$, and Al(axis) represents those on the axis. Since the distances from the hydrogen atom to the aluminum atoms are different for each atom in Al(ring)$_2$ and Al(axis), only the range of values is dictated in table 2. After the hydrogen adsorption, the number density of electrons on Al(ring)$_1$ increases as seen by comparing with table 1. This increase is compensated by the decrease of that on the hydrogen atom. Significant changes for Al atoms on the axis are not seen. Focusing on each orbital in Al(ring)$_1$, the number densities of electrons on p and d orbital increase and that on s orbital decreases. In other words, electrons are transfered to orbitals which have directionality.

In the following, we discuss the migration of the adsorbed hydrogen atom. The hydrogen atom is slightly charged, and hence, we can roughly estimate how large electric field drives the hydrogen atom, once we know the potential barrier. However, this is not so straightforward, since the potential barrier will be modified by electric fields. We do not discuss further this point.

III-ii Potential energy surface and diffusion path of a hydrogen atom

Results of PES calculations are shown in fig. 4 for $z = 0D$, $4D/5$, and $1D$ surfaces, which are characteristic ones. The position of the most stable point is $(\rho, \theta, z) = (4.07\ \text{Å}, 0, 0D)$ and its adsorption energy is calculated as 0.12 eV. This means that the depth of this PES in the radial direction is large and the hydrogen desorption is not easy. As seen in fig. 4, the gradient of the PES along the radial direction is much larger than that along the angular and axial directions. This means that we can parametrize adsorption points by θ and z. The difference of the adsorption energy from the most stable point $(\theta, z) = (0, 0D)$ is shown as a function of θ and z in fig. 5(a). The value of ρ is taken so that the adsorption energy is minimum, which is shown in fig. 5(b). It can be seen that the range of ρ is almost limited within 1 Å. The adsorption energy has a strong correlation with the value of ρ. The most stable point on $z = 1D$ surface is given for $(\rho, \theta, z) = (3.47 \text{ Å}, \pi/10, 1D)$. The most stable point as a function of z is shifted from $\theta = 0$ to $\theta = \pi/10$ around $z = 4D/5$. This is due to the difference of the angle between pentagonal rings.

We consider two paths of the hydrogen diffusion, axial and angular directions, as shown in fig. 6. Path A is the move toward the axial direction and path B shows that toward the angular direction. For path A, we consider the shift of θ together, since the most stable point for $z = 1D$ is given by $\theta = \pi/10$. The energy curves along path A and B are shown as a function of z and θ, respectively, which are normalized by D and $\theta_0 = \pi/5$. In the case of path A, the activation energy is the highest at $z = 4D/5$ whose energy is 0.19 eV. Then the hydrogen atom is in a metastable state at $(\rho, \theta, z) = (3.47 \text{ Å}, \pi/10, 1D)$. In this position, the distances from the hydrogen atom to the two nearest aluminum atoms on the different pentagonal rings are the same. On the other hands, the peak of energy of path B is given at $\theta = 4\theta_0/5$, and the activation energy is 0.57 eV. As in the case of path A, the hydrogen atom is in a metastable state at $(\rho, \theta, z) = (3.07 \text{ Å}, \pi/5, 0D)$, and the distances from the hydrogen atom to the two nearest aluminum atoms on the same pentagonal ring are the same. From these results, the hydrogen atom can move to the axial direction more easily. The distance from one aluminum atom on a pentagonal ring to another atom on the same pentagonal ring is equal to that on the next different pentagonal rings (2.90 Å). However the activation energies for the hydrogen diffusion along the path A and B are quite different. One difference is the distance from the initial position. To compare the distances, we consider simply the cylinder of the radius 4.07 Å, the distance from one adsorption point to another point on the same pentagonal ring is 5.11 Å. On the other hands, the distance from one adsorption point to the next different pentagonal rings is 3.58 Å. Thus the length of path A is shorter than that of the other.

The difference between two paths can also be seen in the viewpoint of the kinetic energy density. The kinetic energy density calculation is carried out for the aluminum nanowire without the hydrogen atom. Figures 7(a) and (b) show the value of ρ and the potential energy, where the kinetic energy density is zero, as a function of θ and z. Compared to fig. 5, the surface of the zero kinetic energy density and that of the minimum potential energy surface have the pattern similar to each other. In both isosurfaces of ρ, there is a deeper dent for the radial direction between aluminum atoms on the same pentagonal ring than that on different pentagonal rings. The values of the adsorption energy are almost the same as those for PES, since ρ is also almost the same. The zero kinetic energy density surface is originally proposed as a surface of a molecule [16]. This implies that the minimum potential energy surface is quite similar to the nanowire surface. Hence the hydrogen diffusion path may be roughly identified with the shortest path on this surface. This character of the zero kinetic energy density surface can also be seen in Al_{13} cluster model which has two pentagonal rings and three Al atoms on the axis. This surface is obtained by a molecular system calculation [23, 25]. Hence this character is due to two pentagonal rings structure and not peculiar to a nanowire model.

III-iii Wave function of hydrogen and deuterium atoms

In fig. 8, we show the probability densities of the hydrogen atom from the ground state to the ninth excited state. The isosurfaces are depicted for the value, $0.01[1/\mathrm{\AA}^3]$, and ϵ is the energy eigenvalue. In the ground state, the probability density is localized around the top site of an aluminum atom. This position corresponds to that of the minimum of the PES. The energy eigenvalue of the ground state is 0.34 eV, so that the zero-point vibrational energy is estimated as 0.22 eV. Patterns of probability densities in excited states are divided into two kinds. In one of patterns, the probability densities are distributed around the top site of an aluminum atom ($z \sim 0$ and $\theta \sim 0$). In the other pattern, the probability densities are seen around the intermediate point of the axial migration path, i.e. between aluminum pentagonal rings, ($z \sim D$ and $\theta \sim 10/\pi$). Note that the migration path to the axial direction is accompanied by the angular rotational shift of $\pi/5$. The latter group consists of, the sixth, seventh, and eighth excited states. The density is high enough at the intermediate point of the migration path of the axial direction, where the potential energy surface has high value as seen in fig. 6. Their energy eigenvalues are 0.42 eV (sixth) and 0.43 eV(seventh and eighth), respectively. (The seventh and the eighth excited states are not degenerate, though they can be seen so within this accuracy.) The energy difference between the sixth excited state and the ground state is 0.08 eV. This energy difference is much smaller than the activation energy of the PES calculation, 0.19 eV. As a result, the diffusion of the hydrogen atom to the axial direction through excited states in the quantum picture requires smaller energy compared to the estimate by the classical picture. In addition, the diffusion to the angular direction is seen to be not favored even in the quantum picture.

In fig. 9, we also show the probability densities of a deuterium atom. The value of isosurfaces is the same as fig. 8. The energy eigenvalue of the ground state is 0.31 eV, which is less than that for the hydrogen atom by 0.03 eV. The difference originates in the difference of the mass between the hydrogen and deuterium atoms and results in the decrease of the zero-point vibrational energy. In the ground state, the distribution of the probability density is almost the same as in the case of the hydrogen atom, while the order of the distribution pattern is replaced in some excited states. Specifically, the pattern of sixth excited state in the hydrogen atom appears in the eighth excited state. These states are the lowest among states that the probability densities are seen between aluminum pentagonal rings. The energy difference between the ground state and this excited state is 0.09 eV. The discrepancy from that of the hydrogen atom is not so large. Therefore, deuterium atoms also travel to the axial direction through excited states.

IV Summary

We have studied the behavior of a hydrogen atom on aluminum nanowire based on density functional theory. First we have calculated the potential energy surface. The most stable position of the adsorbed hydrogen atom is the top site of an aluminum atom, and the adsorption energy is 0.12 eV. The activation energy of the hydrogen diffusion to the axis direction is 0.19 eV, while that to the angular direction is 0.57 eV. Thus the hydrogen can travel to the axial direction more easily. We have also studied quantum effects of the adsorbed hydrogen and deuterium atoms. The probability density of the hydrogen atom in the ground state is localized at the top site of an aluminum atom. In some excited state, the probability density is distributed between pentagonal rings. The energy difference from the ground state is 0.08 eV, which is much smaller than the activation energy in the PES calculation. On the other hand, in the case of the deuterium atom, the energy eigenvalues are lowered slightly. The energy difference between the ground state and the excited state distributed between pentagonal rings increases slightly and is calculated as 0.09 eV. These results imply that the diffusion of the hydrogen and deuterium atoms to the axial direction through excited states in the quantum picture requires smaller energy compared to the estimate by the classical picture.

Reference

[1] Y. Kondo and K. Takayanagi, Science **289**, 606 (2000).

[2] V. Rodrigues, T. Fuhrer, D. Ugarte, Phys. Rev. Lett. **85**, 4124 (2000).

[3] A. Nakamura, M. Brandbyge, L. B. Hansen, K. W. Jacobsen, Phys. Rev. Lett. **82**, 1538 (1999).

[4] O. Gülseren, F. Ercolessi, E. Tosatti, Phys. Rev. Lett. **80**, 3775 (1998).

[5] T. Makita, K. Doi, K. Nakamura, A.Tachibana, J. Chem. Phys. **119**, 538 (2003).

[6] M. Suzuki, K. Nagai, S. Kinoshita, K. Nakajima, K. Kimura, T. Okano, K. Sasakawa, Appl. Phys. Lett. **89**, 133103 (2006).

[7] M. Saka and R. Ueda, J. Mater. Res. **20**, 10 (2005).

[8] Y. Kawakami, T. Kikura, K. Doi, K. Nakamura, and A. Tachibana, Mater. Sci. Forum., **426-432**, 2399 (2003).

[9] A. Goldberg, I. Yarovsky, Phys. Rev. B **75**, 195403 (2007).

[10] M. F. Luo, G.R. Hu, Surf. Sci. **603**, 1081 (2009).

[11] H. Nakano, H. Ohta, A. Yokoe, K. Doi, A. Tachibana, J. Power Sources **163**, 125 (2006).

[12] R. M. Nieminen, M. J. Pusuka, Physica **127B**, 417 (1984).

[13] M. J. Pusuka, R. M. Nieminen, Surf. Sci. **157**, 413 (1985).

[14] P. Sen, O. Gülseren, T. Yildirium, I. P. Batra, and S. Ciraci, Phys. Rev. B **65**, 235433 (2002).

[15] A. Fukushima, K. Doi, M. Senami, A. Tachibana, J. Power Source **184**, 60 (2008).

[16] G. Källén, G. Wahnström, Phys. Rev. B **65**, 033406 (2001).

[17] K. Nobuhara, H. Nakanishi, H. Kasai, A. Okiji, Surf. Sci. **493**, 271 (2001).

[18] A. Tachibana, Int. J. Quantum Chem. Symp. **21**, 181 (1987); A. Tachibana, R.G. Parr, Int. J. Quantum Chem. **41**, 527 (1992); A. Tachibana, Int. J. Quantum Chem. **57**, 423 (1996); A. Tachibana, Theor. Chem. Acc. **102**, 188 (1999); A. Tachibana, J. Chem. Phys. **115**, 3497 (2001); A. Tachibana, Stress Induced Phenomena in Metallization, American Institute of Physics, New York, p. 105 (2002); A. Tachibana, in: E. Brändas, E. Kryachko (Eds.), Fundamental Perspectives in Quantum Chemistry: A Tribute to the Memory of Per-Olov Löwdin, vol. II, Kluwer Academic, Dordrecht, p.211 (2003); A. Tachibana, J. Mol. Model **11**, 301 (2005); A. Tachibana, J. Mol. Struct. (THEOCHEM) **943**, 138 (2010).

[19] G. Kresse and J. Hafner, Phys. Rev. B **47**, 558 (1993); G. Kresse and J. Hafner, Comput. Mater. Sci. **6**, 15 (1996); G. Kresse and J. Furthmüller, Phys. Rev. B **54**, 11169 (1996).

[20] G. Kresse and D. Joubert, Phys. Rev. B **59**, 1758 (1999).

[21] J. P. Perdew, K. Burke, M. Ernzerhof, Phys. Rev. Lett. **77**, 3865 (1996).

[22] M. Bockstedte, A. Kley, J. Neugebauer, M. Scheffler, Comp. Phys. Comm. **107**, 187 (1997).

[23] M. J. Frisch *et al.*, Gaussian 03, Revision B.05,Gaussian, Inc., Pittsburgh PA (2003).

[24] Periodic Regional DFT Program Package, ver. 3, Tachibana Lab., Kyoto University, Kyoto (2008); For example see, K. Doi, K. Nakamura and A. Tachibana, The proceedings of 2006 International Workshop on Nano CMOS 209 (2006).

[25] Molecular Regional DFT Program Package, ver. 3, Tachibana Lab., Kyoto University, Kyoto (2008); For example see, K. Doi, K. Nakamura and A. Tachibana, The proceedings of 2006 International Workshop on Nano CMOS 209 (2006).

Table 1: Number of valence electrons calculated from PDOS. Al(ring) and Al(axis) mean an aluminum atom on a pentagonal ring and on the axis, respectively.

Atom	s-orbital	p-orbital	d-orbital	total
Al(ring)	1.245	1.285	0.289	2.820
Al(axis)	1.228	2.014	0.659	3.902

Table 2: Number of valence electrons calculated from PDOS. Al(ring)$_1$ is the aluminum atom on which the hydrogen is adsorbed and Al(ring)$_2$ is aluminum atoms on pentagonal rings except for Al(ring)$_1$. For Al(ring)$_2$ and Al(axis), only the range of values is given.

Atom	s-orbital	p-orbital	d-orbital	total
Al(ring)$_1$	1.156	1.616	0.409	3.181
Al(ring)$_2$	1.241-1.254	1.260-1.301	0.281-0.291	2.813-2.834
Al(axis)	1.225-1.230	1.987-2.030	0.650-0.678	3.895-3.905
H	0.620	0.010	0.001	0.630

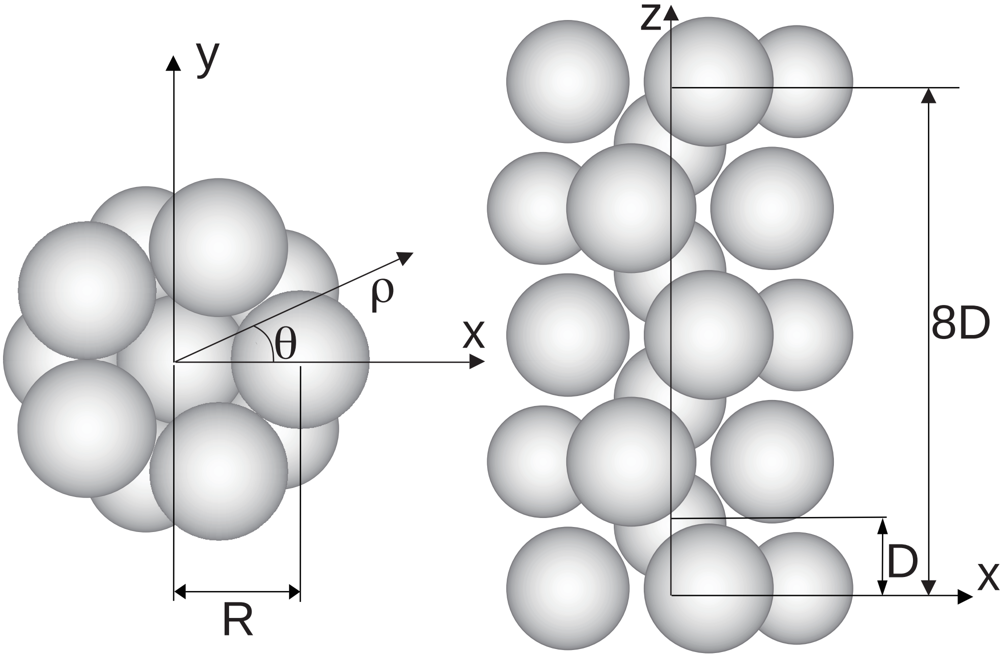

Figure 1: Calculation model of aluminum nanowire. This model has pentagonal rings whose angles are different by $\pi/5$ from each other. R is the radius of the pentagonal ring, D is the half-distance between aluminum atoms on the axis, and $8D$ is the unit cell length. ρ, θ, and z are used for a cylindrical coordinate system in PES calculations.

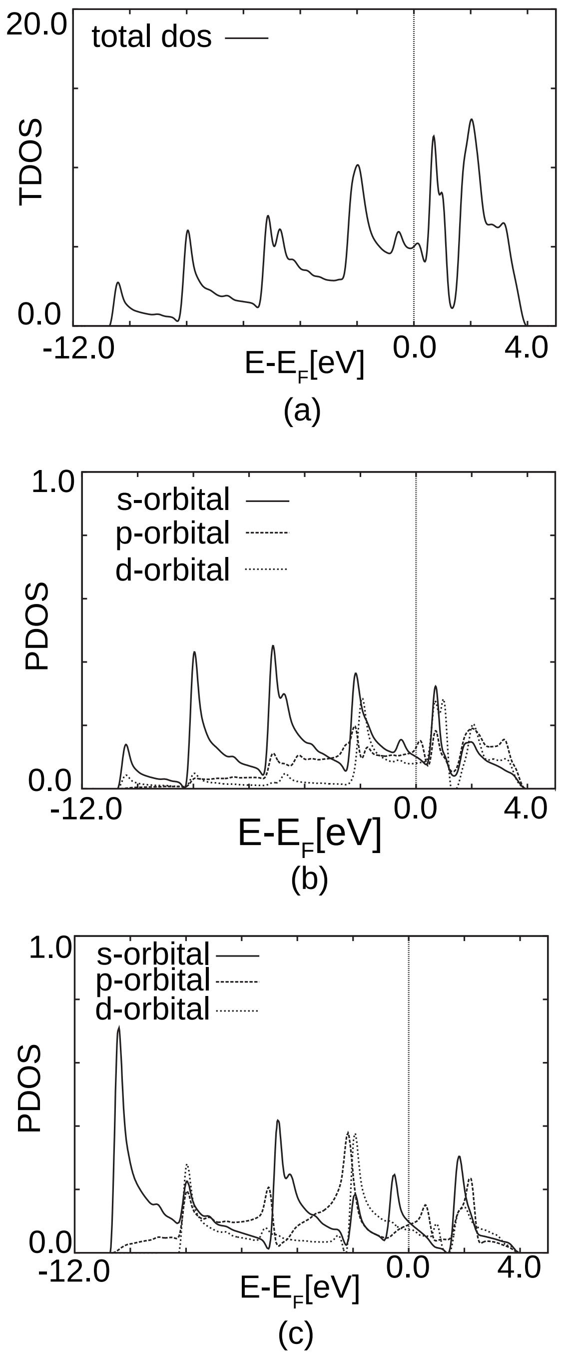

Figure 2: TDOS and PDOS of the nanowire model, (a) TDOS of this model, (b) PDOS of atoms on the pentagonal ring, and (c) PDOS of atoms on the axis, respectively. The Fermi level is taken to be 0.0 eV shown as vertical dotted lines.

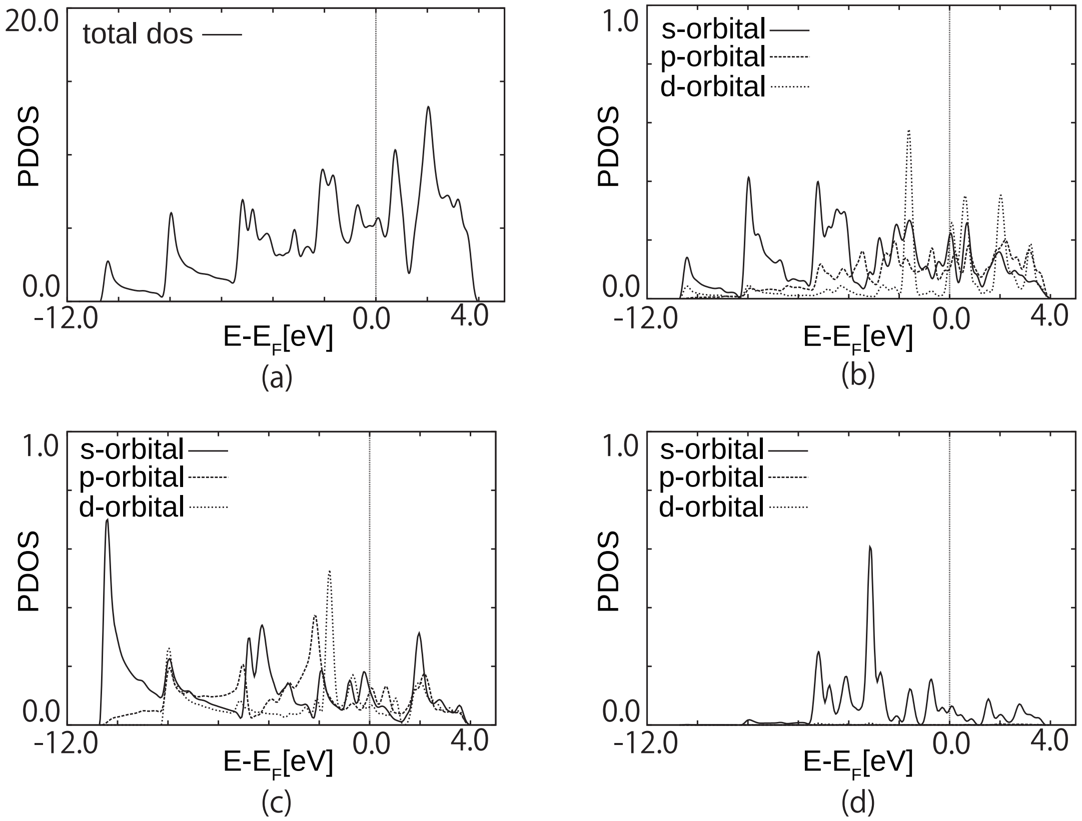

(a)

(b)

(c)

(d)

Figure 3: TDOS and PDOS of the nanowire model, (a) TDOS of this model, (b) PDOS of the aluminum atom on which the hydrogen is adsorbed, (c) PDOS of aluminum atoms on the axis, and (d) PDOS of the hydrogen atom, respectively. The Fermi level is taken to be 0.0 eV shown as vertical dotted lines.

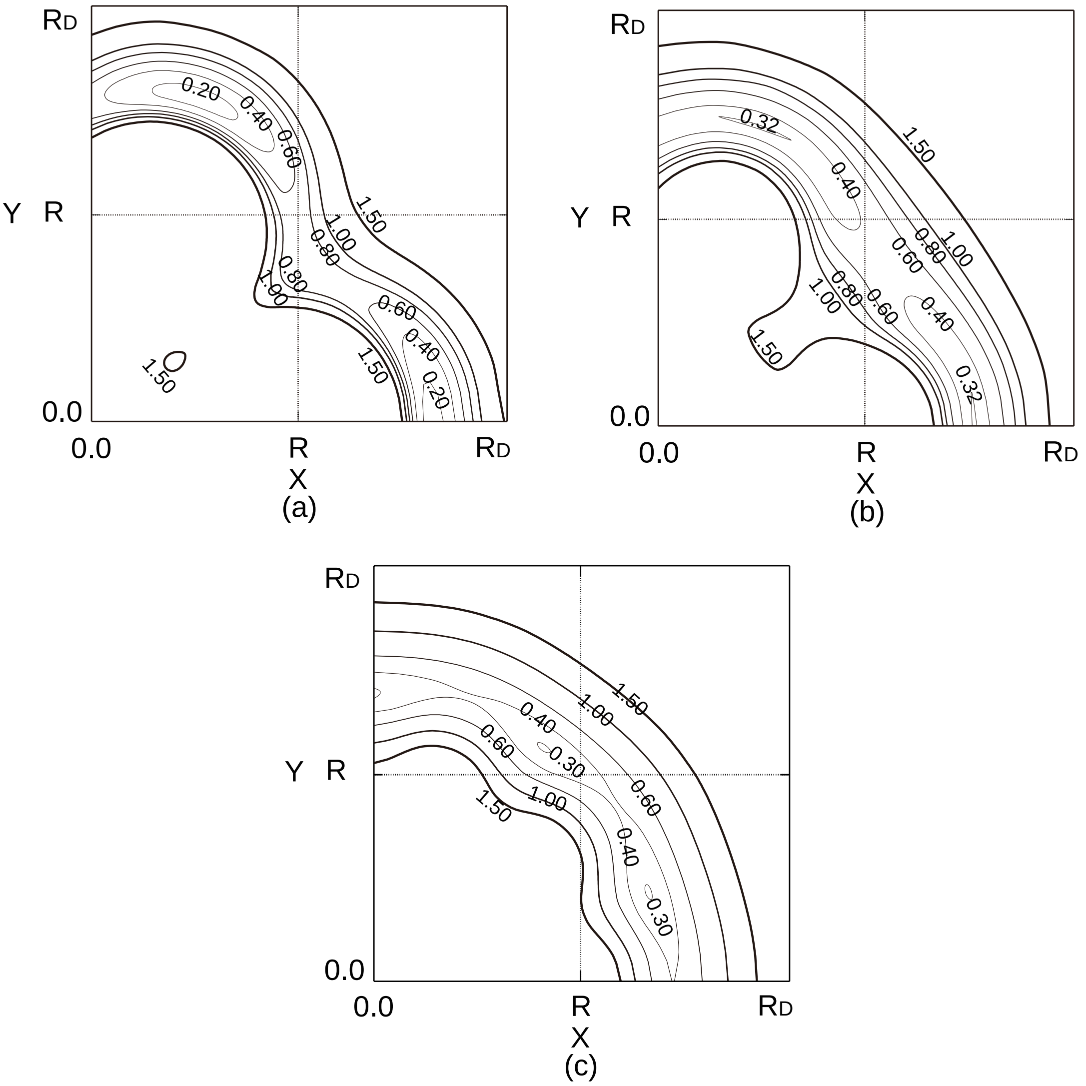

Figure 4: Potential energy surface of the hydrogen atom adsorption. (a) $z = 0D$ surface, (b) $z = 4D/5$ surface, and (c) $z = 1D$ surface. The unit of the energy is eV.

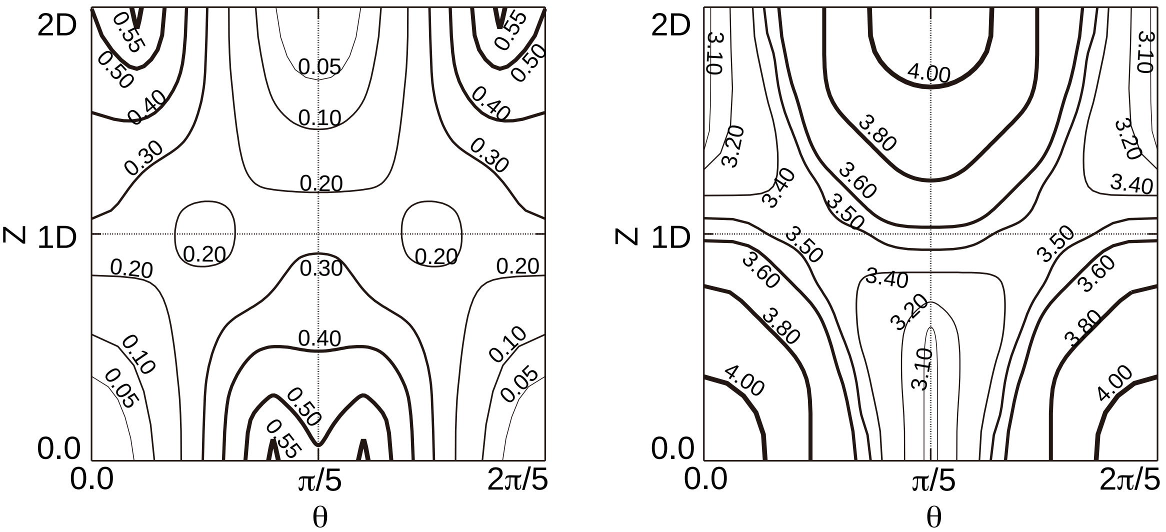

(a) (b)

Figure 5: (a) The difference of the potential energy surface as a function of θ and z. The unit of the energy is eV. The value of ρ is taken as that in figure (b). (b) The value of ρ so that the adsorption energy is minimum as a function of θ and z. The unit of ρ is Å

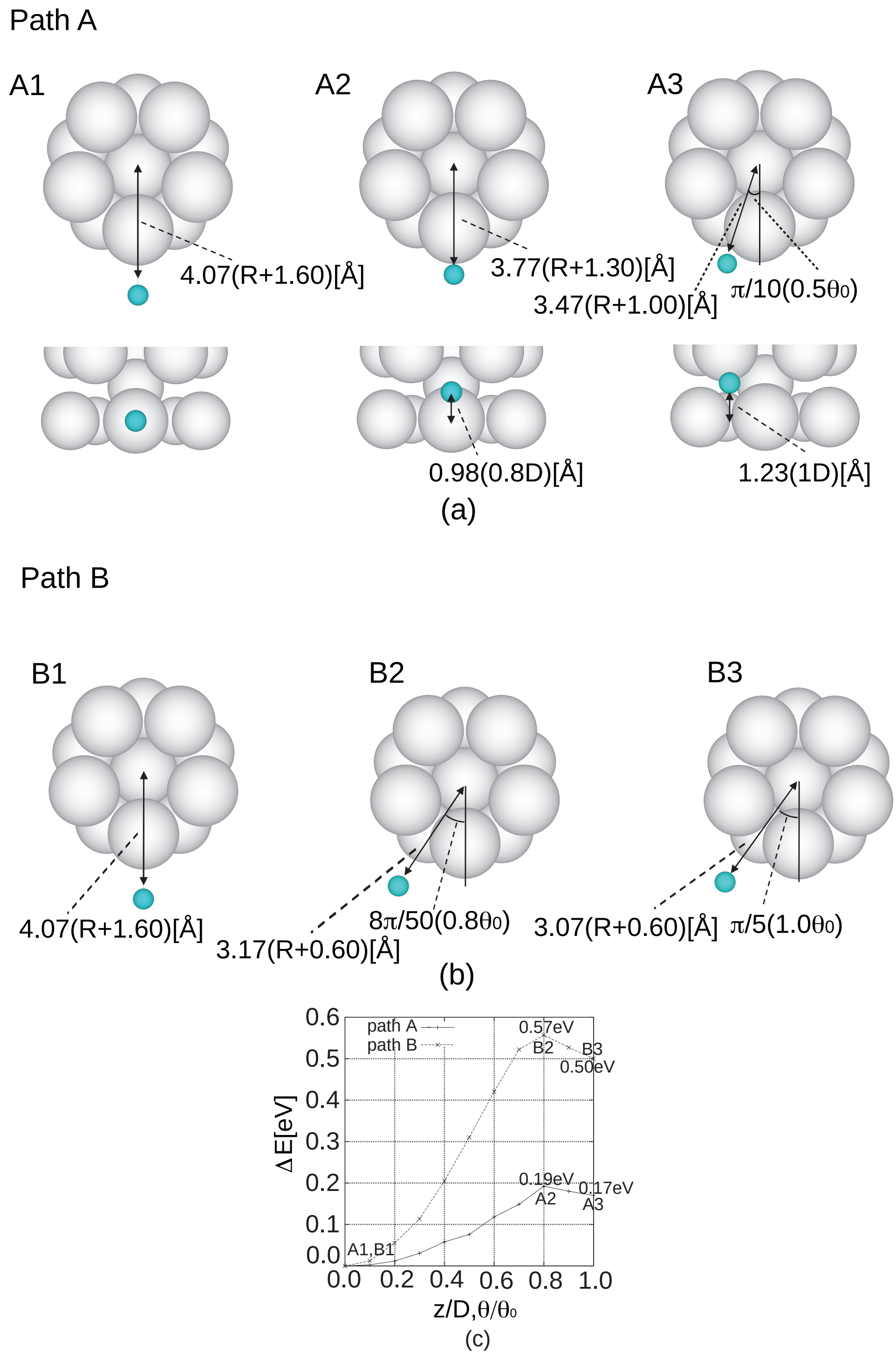

Figure 6: Paths for the move of a hydrogen atom and the energy along these paths. (a) three typical points in path A, (b) three typical points in path B, and (c) the energy curves of paths A and B as a function of z and θ ($\theta_0 = \pi/5$), respectively. A(1,2,3) and B(1,2,3) correspond to points in figures (a) and (b).

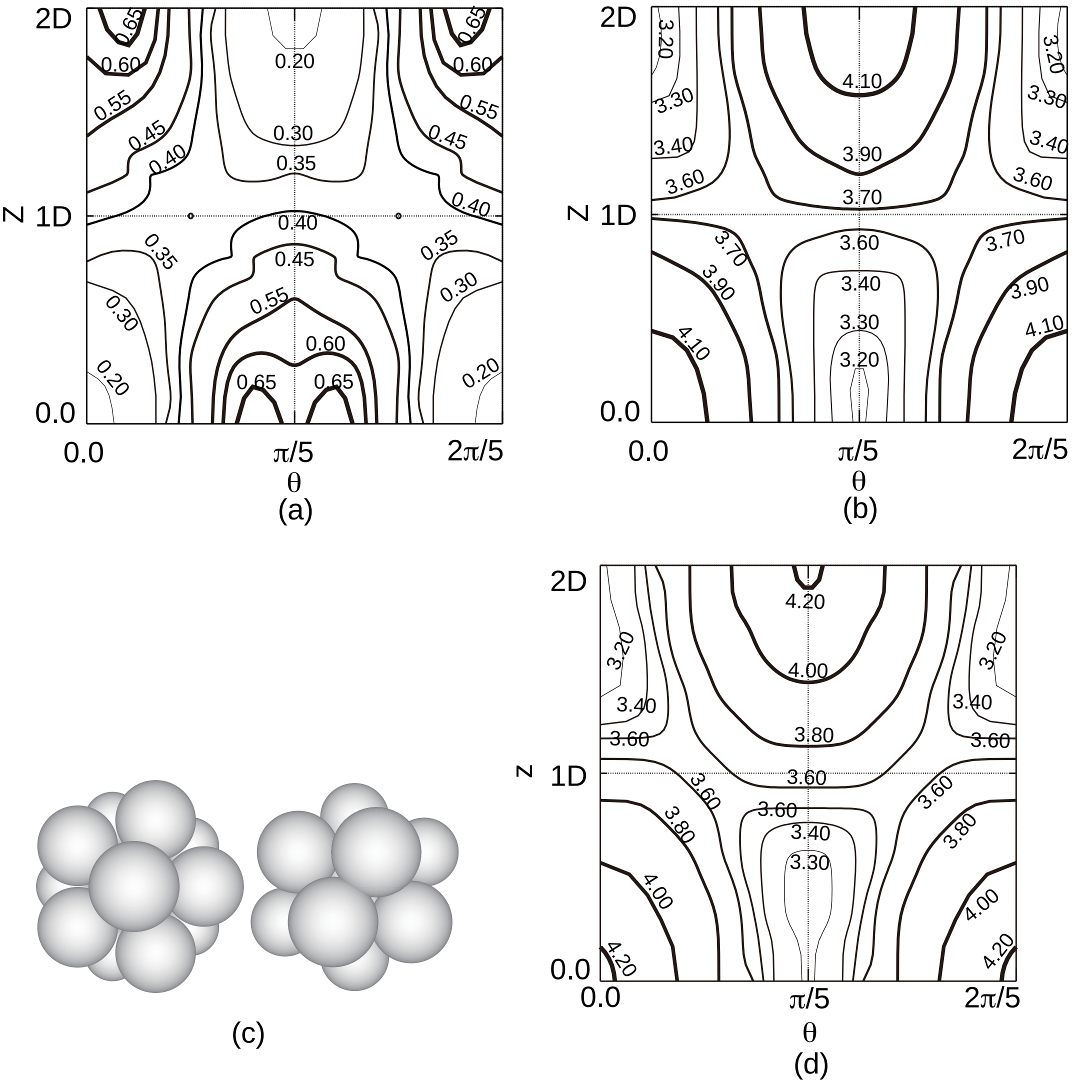

Figure 7: (a) The potential energy as a function of θ and z. The unit of energy is eV. The value of ρ is taken as that in figure (b). (b) The value of ρ where the kinetic energy density is zero, as a function of θ and z. The unit of ρ is Å. (c) The calculation model of Al_{13} cluster. The radial parameter (R) and the half-distance between aluminum atoms on the axis (D) are the same as those of the nanowire model. (d) The value of ρ where the kinetic energy density is zero, as a function of θ and z for the Al_{13} cluster model.

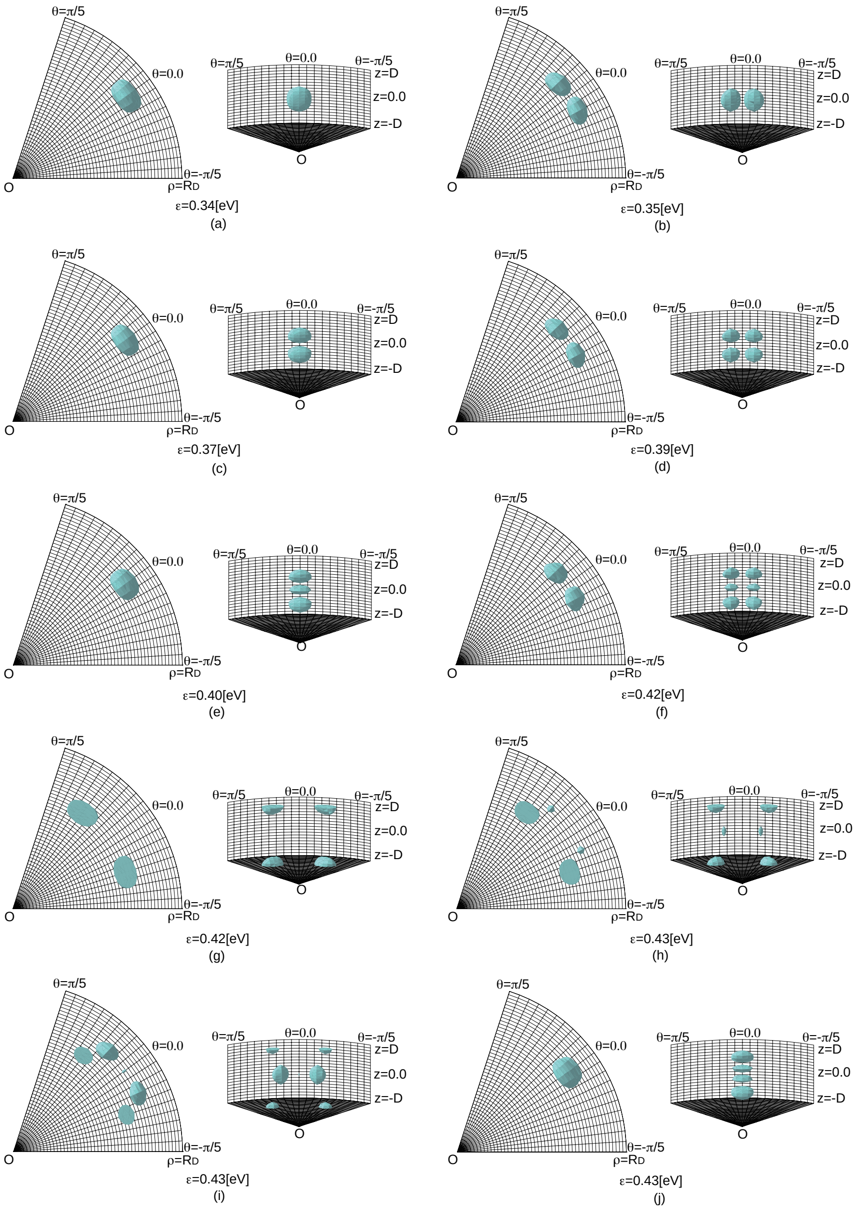

ε=0.34[eV]
(a)

ε=0.35[eV]
(b)

ε=0.37[eV]
(c)

ε=0.39[eV]
(d)

ε=0.40[eV]
(e)

ε=0.42[eV]
(f)

ε=0.42[eV]
(g)

ε=0.43[eV]
(h)

ε=0.43[eV]
(i)

ε=0.43[eV]
(j)

Figure 8: The distribution of the probability densities of the hydrogen atom from the ground state to the ninth excited state. The isosurfaces are depicted for the value, $0.01[1/\mathring{A}^3]$, and ϵ is the energy eigenvalue.

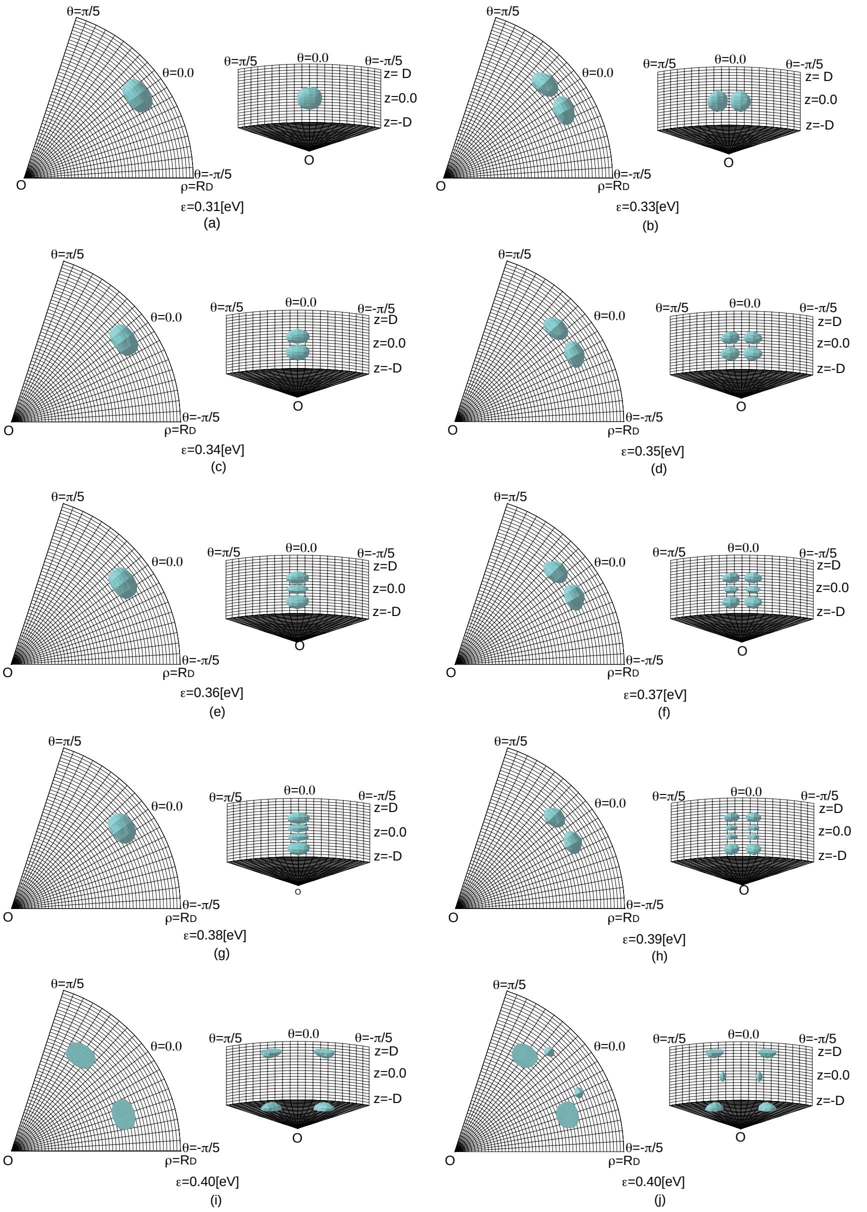

ε=0.31[eV]
(a)

ε=0.33[eV]
(b)

ε=0.34[eV]
(c)

ε=0.35[eV]
(d)

ε=0.36[eV]
(e)

ε=0.37[eV]
(f)

ε=0.38[eV]
(g)

ε=0.39[eV]
(h)

ε=0.40[eV]
(i)

ε=0.40[eV]
(j)

Figure 9: The distribution of the probability densities of the deuterium atom from the ground state to the ninth excited state. The isosurfaces are depicted for the value, $0.01[1/\mathring{A}^3]$, and ϵ is the energy eigenvalue.

Chapter 3

Local dielectric property of cubic hafnia

I Introduction

The leak current in complementary metal-oxide-semiconductor (CMOS) is a serious problem in viewpoints of, e.g., the reliability of advanced electronic devices and the loss of electric power. Recently, many researchers have argued that hafnium oxide (HfO_2) materials are superior to silicon dioxide (SiO_2) for the gate insulator due to their high dielectric constants [1, 2].

The hafnia has several structures of crystal and their dielectric constants are dependent on the structures. The dielectric constant of the most stable monoclinic structure is reported as about 16, while the metastable phase, e.g., the cubic and tetragonal structures (or these structures are stable at very high temperature), have higher dielectric constants. In a work of computational science, the dielectric constant of the cubic and tetragonal hafnia is predicted to be about 20-30 and 40-70, respectively.[3, 4] Experimentally, the cubic or tetragonal hafnia derived by yttrium-doped hafnia or a mixture film of HfO_2 and ZrO_2, shows a higher dielectric constant, about 30 [5, 6]. While the cubic (and tetragonal) hafnia has an advantage of a higher dielectric constant, it is metastable structure below 1700°C. Nevertheless, many experimental attempts to fabricate the cubic hafnia are made as mentioned above. Hence, the cubic hafnia may be available as device material in the near future.

Very high-k materials such as the cubic hafnia will be important for very small CMOS chips, which have a few nanometer thickness. To study the dielectric property of nanosize materials, the macroscopic dielectric constant is not appropriate, which is derived as the average of dielectric responses from the whole region of a material. Hence, one of the authors has defined the dielectric constant density tensor for the analysis of nano-materials [7, 8]. In our laboratory, we have studied high-k materials in terms of this dielectric constant density [9]. In our previous work, we have clarified the relation between local dielectric property and electron population on a lanthanum atom in a lanthanum oxide cluster.

In this work, we investigate the dielectric property of the cubic hafnia in terms of the electronic contribution to the static dielectric constant density tensor. We show that the cubic hafnia show complicated responses to external electric field, particularly, rotational responses. Of course, the existence of oxygen vacancies is an important topic for hafnium oxide gate thin films [3–5, 9, 13]. Hence, the analyses of models with oxygen vacancies is important for hafnium oxide materials. For the analyses, the comprehension of the model without vacancies is of course a first step. Therefore, we study the dielectric property of the cubic hafnia crystal without oxygen vacancies. In this work, we consider only the electronic contribution to the dielectric response. It is well known that the lattice contribution dominates over the electronic one and is more sensitive to the structure of the material. [3, 4, 14, 15]. One of the purposes of this work is to clarify the electronic contribution to the local dielectric response before we include the lattice contribution.

This article is organized as follows. In the next section, we show the formalism of the polarizability density tensor and the local dielectric constant density tensor operator. In § III, the calculation models and conditions are explained. Our results are shown in § IV. The local dielectric properties are discussed for the cubic hafnia. In some region, the eigenvalues of the dielectric constant density tensor show complex values. We pay particular attention to this region, where the dielectric response show rotational behavior. We also study the dependence of results on the termination condition of cluster models. The last section is devoted to the summary.

II Theory

In this section, we show our formalism of the dielectric constant density operator, defined in the Rigged QED theory [7, 8]. A system (A) is embedded in an environmental background medium (M). The corresponding scalar potentials are given as the regional integrals of the electrical charge,

$$\hat{A}_{0_{A,M}}(\vec{r}) = \int_{A,M} d^3\vec{s}\frac{\hat{\rho}(\vec{s})}{|\vec{r}-\vec{s}|}. \tag{1}$$

Here, $\hat{\rho}(\vec{r})$ is the charge density defined as,

$$\hat{\rho}(\vec{r}) = Z_e e \sum_a \hat{\psi}_a^{\dagger}(\vec{r})\hat{\psi}_a(\vec{r}), \tag{2}$$

where $Z_e = -1$ for the electron. The electric field $\hat{\vec{E}}(\vec{r})$ is given as the sum of the electric displacement $\hat{\vec{D}}(\vec{r})$ of the medium M and the polarization $\hat{\vec{P}}(\vec{r})$ of the system A. These are defined as follows,

$$\hat{\vec{D}}(\vec{r}) = -\mathrm{grad}\hat{A}_{0_M}(\vec{r}), \tag{3}$$

$$\hat{\vec{P}}(\vec{r}) = \frac{1}{4\pi}\mathrm{grad}\hat{A}_{0_A}(\vec{r}), \tag{4}$$

where the time variation of the vector potential is neglected since only steady states are considered in this work. As a result, the electric field is given as,

$$\hat{\vec{E}}(\vec{r}) = \hat{\vec{D}}(\vec{r}) - 4\pi\hat{\vec{P}}(\vec{r}). \tag{5}$$

The electric displacement $\hat{\vec{D}}(\vec{r})$ of the medium M works as the external electric field for the system A. The polarization of the system A is, hence, considered to be linear response to $\hat{\vec{D}}(\vec{r})$,

$$\hat{\vec{P}}(\vec{r}) = \hat{\overset{\leftrightarrow}{\alpha}}(\vec{r})\hat{\vec{D}}(\vec{r}), \tag{6}$$

where $\hat{\overset{\leftrightarrow}{\alpha}}(\vec{r})$ is the polarizability density tensor. The dielectric constant density tensor $\hat{\overset{\leftrightarrow}{\epsilon}}(\vec{r})$ is, therefore, defined as

$$\hat{\vec{D}}(\vec{r}) = \hat{\overset{\leftrightarrow}{\epsilon}}(\vec{r})\hat{\vec{E}}(\vec{r}) = \frac{1}{1-4\pi\hat{\overset{\leftrightarrow}{\alpha}}(\vec{r})}\hat{\vec{E}}(\vec{r}). \tag{7}$$

These operators of the polarizability density tensor and the dielectric constant density tensor are Hermite operators, and all the elements of these tensors are real. However, these tensors are not symmetric tensor, and hence, its eigenvalues have three real values, or one real and two complex values. The case with the complex eigenvalues is interesting, since the dielectric response shows rotational behavior. We show the absolute values and the arguments for these complex eigenvalues, while the eigenvalues and eigenvectors are shown for real eigenvalues. Note that the complex eigenvalues can be correctly described only in the analysis using tensor, since it is due to off-diagonal elements. The off-diagonal elements of the ordinary global dielectric constant tensor are negligible for large enough amorphous materials and crystals with high symmetry, such as cubic hafnia. However, the off-diagonal elements cannot be neglected for nano-materials and in a local region even for the materials and crystals. Hence, the local and tensor analyses are important for very thin dielectric films.

III Calculation Models and Conditions

In this section, we explain our calculation models and conditions. In Fig. 1, the cluster models of cubic hafnia are shown. The left panel shows the structure of the point charge model. The gray and red spheres mean hafnium and oxygen atoms, respectively. The point charge model is embedded in the sea of point charges, which are used as the termination condition for the realization of the situation that the analyzed system in a large crystal is surrounded by other atoms in the crystal. In this model, there are 13 Hf and 56 O atoms, and 606 point charges are put on surrounding Hf and O sites. The distance between Hf and O atoms are determined as 2.200 Å by our geometrical optimization calculations. In the calculations, only the Hf-O length is varied with keeping the structure. This Hf-O length is well consistent with the values by experimental results and other computational works [3, 17, 18]. The spin multiplicity is determined so that the Mulliken charges of the

Hf atoms in the system are distributed uniformly as well as those of the O atoms. As a result, the spin multiplicity is chosen as 1. The charges of the point charges are determined as follows. The point charges on the Hf sites have a positive charge, while those on the O sites have a negative charge, whose value is the half of that on the Hf sites. The values of these charges are determined again so that the Mulliken charges of the atoms in the analyzed system are uniformly distributed. As a result, the charges of the hafnium and oxygen sites are determined as 1.0 and -0.5, respectively.

For comparison, we consider the model with hydrogen termination shown in the right panel in Fig. 1. The light blue spheres in the right panels are hydrogen atoms. In this model, the number of the oxygen atoms are 32, and the 24 outer oxygen atoms are terminated by hydrogen atoms instead of point charges. The different number of oxygen atoms are taken for this model, since the condensed features are realized better. The distance between the hydrogen and oxygen atoms is determined as 0.958 Å and the spin multiplicity is determined as 13. This model represents an extreme case that the moves of the electrons in the system is restricted strongly due to covalent bonds between oxygen and hydrogen atoms. In our previous work, we used silicon termination models [9]. The silicon termination (exactly SiH_3 termination) is superior to the hydrogen termination in viewpoints of the representation of the condensed analyzed system. However, the geometric optimization is required for the silicon termination model and hence the cubic structure never remains. In other viewpoint, our model is interpreted as hafnium terminated model for the inner one Hf and eight oxygen atoms, which is superior to the silicon termination.

The electronic state calculations are performed by using the Gaussian 03 program package [19]. The Hartree-Fock method is chosen to derive the electronic state for the dielectric constant density tensor calculation, since the density functional theory (DFT) is known to overestimate the dielectric constant. [34–38] The basis sets are chosen as the LanL2DZ basis set for Hf atoms [28–30] and the 6-31G** basis sets for O and H atoms. [25, 28] Then, we calculate the dielectric constant density tensor and the polarizability density tensor using these derived electronic states. These calculation are performed by the Molecular Regional DFT program package [16], which is developed in our laboratory.

IV Results

We show the polarizability density tensor for the point charge model in Fig. 2. The result is shown on the plane with one hafnium atom at the center of the model and four oxygen atoms next to the hafnium atom. Figures 2(a)-2(c) show the first, second, and third eigenvalues ($\alpha_{1,2,3}$) of the polarizability density tensor. The eigenvalues are sorted into the descending order. If there are complex eigenvalues, they are arranged as the second and third eigenvalues. The solid line segments show the directions of the eigenvectors. The black blob at the center shows the pseudopotential of the Hf atom. The eigenvalues in the green contours have complex values. We show the absolute value of the complex eigenvalues and their arguments in the figures. Figure 2(d) shows the eigenvalues and their average on the Hf-O line, which is shown in panels (a)-(c) as the solid line. The upper part of this panel is the real part of three eigenvalues and their average. The horizontal dotted line is drawn for $1/4\pi$. The lower part of this panel is the argument.

In these figures, it can be seen that large polarizability density is distributed uniformly in the almost whole region. The slightly larger values can be seen around atoms, particularly oxygen atoms. Small variations around $1/4\pi$ result in significant changes of the dielectric constant density tensor, since it is divergent and changes the sign at $\alpha_i = 1/4\pi$ as seen in eq. (6). The complex eigenvalues are widely seen in Figs. 2(b) and 2(c). Hence, the polarization response to external electric fields should have rotational behavior. These properties cannot be seen in the global and averaged scalar polarization analysis. It can only be described correctly in the local and tensor analysis, as stressed above.

In Fig. 3, we show the dielectric constant density tensor on the same plane and model as Fig. 2. The panels (a)-(c) show the inverse of the first, second, and third eigenvalues

($\epsilon^{-1}_{1,2,3}$) of the dielectric constant density tensor. Figure 3(d) shows the eigenvalues and their average on the Hf-O line, which is shown in panels (a)-(c) as the solid line. The eigenvalues are sorted for not ϵ_i^{-1} but ϵ_i. Other depicting way of these four panels are also the same as Fig. 2. The pattern of the distribution of the dielectric constant density is not simple compared to the polarizability density, since $1/(1-4\pi\alpha_i)$ is divergent at $\alpha_i = 1/4\pi$ as mentioned above. As seen in Fig. 3, we can see the negative values of the dielectric constant density around the oxygen atoms. In the region, the polarization overcomes external electric fields. The global response shows positive dielectric constant as well known, while the local response can have negative dielectric constant density. The pattern of the region with complex eigenvalues is of course the same as Fig. 2, while the rotational angle is much larger than that of the polarizability density. Hence, the small rotational response in the polarizability density induces the large rotational one for the dielectric constant density. As a result, the analyses of the dielectric constant and polarizability as local quantity clarify the complicated response dependent on positions in a system.

Next, we calculate the average of the polarizability density and the dielectric constant density over the cubic cell which has one hafnium atom on its center and eight oxygen atoms on its vertexes. To calculate the averages, the global polarizability is derived by integration over the region V,

$$\langle \overleftrightarrow{\alpha} \rangle = \frac{1}{V} \int_V \hat{\overleftrightarrow{\alpha}}(\vec{r}) d\vec{r}. \tag{8}$$

The global dielectric constant density are calculated with the eigenvalues of the global polarizability as follows,

$$\langle \overleftrightarrow{\epsilon} \rangle = 1/(1 - 4\pi \langle \overleftrightarrow{\alpha} \rangle). \tag{9}$$

The result is summarized in Table 3. The static electronic contribution to the dielectric constant is derived as 3.57. Though the ratio of hafnium and oxygen atoms is different from that of the unit cell, this result is well similar to the values of previous works.[4] Our average is also consistent with the results by Momida et al.[14, 15] Although their results are for the monoclinic hafnia, the electronic contribution is considered to be almost independent of the structure of models. Our global α_i are well isotropic, while the second and third components have small imaginary part. This small anisotropy is due to the usage of the cluster model, which does not have the exactly same symmetry of the crystal.

We also show the results for the model with hydrogen termination for comparison. In this model, moves of electrons in the system are restricted compared to the point charge model, due to covalent bonds between the hydrogen and oxygen atoms. In Fig. 4, we show the local polarizability density on the same plane as Fig. 2. The depicting way of eigenvalues and eigenvectors are also the same as Fig. 2. As seen in these figures, the polarizability density is much smaller compared to that of the point charge model. Since the outer hydrogen atoms fix some electrons in outer oxygen atoms, the sensitivity of electrons to external electric fields is low compared to the point charge model. Moreover, the pattern of the polarizability density is significantly different from that of the point charge model. The regions around atoms have larger values than other regions. The complex eigenvalues are seen in very restricted regions in Figs. 2(b) and 2(c). This is in salient contrast to the point charge model. These results show that the choice of models is important for the calculations to represent the dielectric thin film. In this work, we consider that the hydrogen termination is too restrictive for the move of electrons in the system, and hence, we chose the point charge model.

In addition to the polarizability density, we show the dielectric constant density tensor on the same plane for the model with hydrogen termination in Fig. 5. The depicting way of eigenvalues and eigenvectors are also the same as Fig. 3. As seen in Fig. 5, the typical value of dielectric constant density tensor is much smaller than that of the point charge model. This difference also arises from the difference of the sensitivity of electrons to external electric fields. The results of this model show that the dielectric response is much stronger around atoms than the other region.

The averages of the polarizability and dielectric constant densities are also shown in

Table 3. The average of the dielectric constant is too small compared to those of the point charge model and other works. [4, 14, 15] This smallness of the dielectric constant also confirms the bad boundary condition by the hydrogen termination. The isotropy of α_i and ϵ_i are well realized in this model and better than the point charge model. As a result, in spite of a better property about isotropy, the model with hydrogen termination results in failure to realize the electrons in the dielectric thin films.

We consider that the difference between the results of these two termination models is due to not the electron density itself, but the sensitivity of electrons to external electric fields. To confirm this, we show the electron density on the same plane in Fig. 6. The electron density is almost the same in these two figures. The difference of the density is small by three order of magnitude. Hence, the difference of the dielectric property is almost independent of the electron density itself. As a result, we should pay attention to the termination condition of models in order to realize the condense state of dielectric thin films by using cluster models.

V Conclusions

We have investigated the dielectric property of the cubic hafnia in terms of the polarizability density and the dielectric constant density by using the cluster model embedded in point charges. It is seen that the cubic hafnia shows complicated response to external electric field. Particularly, the dielectric response shows rotational behavior in wide regions. These properties are only correctly clarified in the local and tensor analyses. In the ordinary global and averaged scalar polarization analyses, these properties cannot be described. We have also shown that the choice of models, in particular, termination condition, is important for these analyses. In this work, we have compared the result of the point charge model and that of the hydrogen termination model. The result of the hydrogen termination model have not reproduced the dielectric constant of the cubic hafnia. We speculate that the difference between the results is attributed to the sensitivity of electrons to the external fields. Electrons in the hydrogen termination model are considered to be restricted too much. We have checked this by comparing the electron densities of these two models and the difference of the electron density is negligible. As a result, we consider that the sensitivity of electrons to the external fields is a key quantity for the description of dielectric property, and hence, the choice of the termination condition of model should be paid much attention to realize the condensed state as a dielectric film when we use a cluster model.

Reference

[1] G. D. Wilk, R. M. Wallace, and L. M. Anthony, J. Appl. Phys. **89**, 5243 (2001).

[2] J. Robertson, Eur. Phys. J. Appl. Phys. **28**, 265 (2004).

[3] X. Zhao and D. Vanderbilt, Phys. Rev. B **65**, 233106 (2002).

[4] E. Cockayne, J. App. Phys. **103**, 084103 (2008).

[5] K. Kita, K. Kyuno, and A. Toriumi, Appl. Phys. Lett. **86**, 102906 (2005).

[6] D. H. Triyoso, R. I. Hegde, K. K. Schaeffer, D. Roan, P. J. Tobin, S. B. Samavedam, and B. E. White, Jr., Appl. Phys. Lett. **88**, 222901 (2006).

[7] A. Tachibana, J. Mol. Model., **11**, 301 (2005).

[8] A. Tachibana, J. Mol. Struct. THEOCHEM **943**, 138 (2010).

[9] K. Doi, Y. Mikazuki, S. Sugino, T. Doi, P. Szarek, M. Senami, K. Shiraishi, H. Iwai, N. Umezawa, T. Chikyo, K. Yamada, and A. Tachibana: Jpn. J. Appl. Phys. **47**, 205 (2008); errata, Ph.D. thesis, Pawel Szarek, Theoretical Study of Electronic States of Chemical Bonds, http://hdl.handle.net/2433/66212.

[10] S. Zafar, A. Callegari, E. Gusev, and M. V. Fischetti, J. Appl. Phys. **93**, 9298 (2003).

[11] C. C. Hobbs, L. R. C. Fonseca, A. Knizhnik, V. Dhandapani, S. B. Samavedam, W. J. Taylor, J. M. Grant, L. G. Dip, D. H. Triyoso, R. I. Hegde, D. C. Gilmer, R. Garcia, D. Roan, M. L. Lovejoy, R. S. Rai, E. A. Hebert, H.-H. Tseng, S. G. H. Anderson, B. E. White, and P. J. Tobin, IEEE Trans. Electron Devices **51**, 978 (2004).

[12] K. Shiraishi, K. Yamada, K. Torii, Y. Akasaka, K. Nakajima, M. Konno, T. Chikyow, H. Kitajima, and T. Arikado, Jan. J. Appl. Phys. **43**, L1413 (2004).

[13] X. P. Wang, M. F. Li, A. Chin, C. X. Zhu, J. Shao, W. Lu, X. C. Shen, X. F. Yu, R. Chi, C. Shen, A. C. H. Huan, J. S. Pan, A. Y. Du, P. Lo, D. S. H. Chan, and D. L. Kwong, Solid-State Electron. **50**, 986 (2006).

[14] N. Umezawa, K. Shiraishi, S. Sugino, A. Tachibana, K. Ohmori, K. Kakushima, H. Iwai, T. Chikyow, T. Ohno, Y. Nara, and K. Yamada, Appl. Phys. Lett. **91**, 132904 (2007).

[15] H. Momida, T. Hamada, T. Yamamoto, T. Uda, N. Umezawa, T. Chikyow, K. Shiraishi, and T. Ohno, Appl. Phys. Lett. **88**, 112903 (2006).

[16] H. Momida, T. Hamada, and T. Ohno, Jpn. J. Appl. Phys. **46**, 3255 (2007).

[17] J. Wang, H. P. Li, and R. Stivens, J. Mater. Sci. **27**, 5397 (1992).

[18] A. A. Demkov, Phys. Status, Solidi B **226**, 57 (2001).

[19] M. J. Frisch *et al.*, Gaussian 03, Revision B.05, Gaussian, Inc., Pittsburgh PA 2003.

[20] S. Baroni and R. Resta, Phys. Rev. B **33**, 7017 (1986).

[21] Z. H. Levine and D. C. Allan, Phys. Rev. B **43**, 4187 (1991).

[22] Z. H. Levine and D. C. Allan, Phys. Rev. B **44**, 12781 (1991).

[23] Z. H. Levine and D. C. Allan, Phys. Rev. Lett. **63**, 1719 (1989).

[24] Z. H. Levine and D. C. Allan, Phys. Rev. Lett. **66**, 41 (1991).

[25] P. J. Hay and W. R. Wadt, J. Chem. Phys. **82**, 270 (1985).

[26] W. R. Wadt and P. J. Hay, J. Chem. Phys. **82**, 284 (1985).

[27] P. J. Hay and W. R. Wadt, J. Chem. Phys. **82**, 299 (1985).

[28] W. J. Hehre, R. Ditchfield, and J. A. Pople, J. Chem. Phys. **56**, 2257 (1972).

[29] P. C. Hariharan and J. A. Pople, Theo. Chim. Acta. **28**, 213 (1973).

[30] M. Senami, K. Ichikawa, K. Doi, P. Szarek, K. Nakamura, and A. Tachibana, Molecular Regional DFT program package, ver. 3 (Tachibana Lab., Kyoto University, Kyoto, 2008).

Table 1: The average of the polarizability and the dielectric constant.

Model	α_1 ϵ_1	α_2 ϵ_2	α_3 ϵ_3	Average of α_i Average of ϵ_i
Point charge	0.0604	$0.0569 + 0.0060i$	$0.0569 - 0.0060i$	0.0581
	4.14	$3.28 + 0.87i$	$3.28 - 0.87i$	3.57
Hydrogen termination	0.0116	0.0116	0.0115	0.0116
	1.17	1.17	1.17	1.17

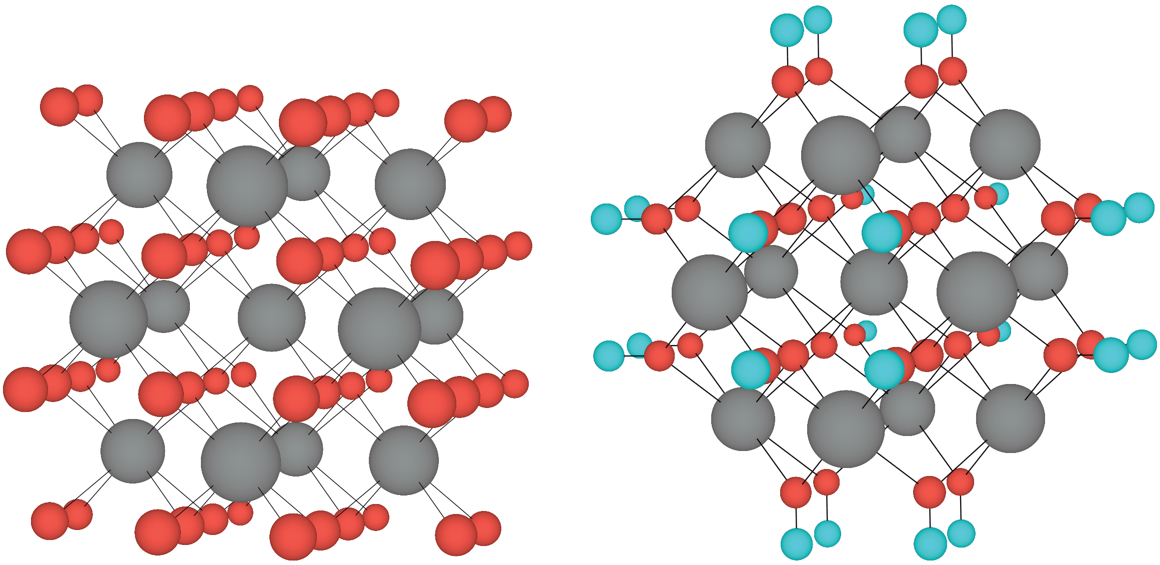

Figure 1: The cluster models of cubic hafnia are shown. The gray and red spheres mean hafnium and oxygen atoms, respectively. The left and right panels show the structure of the point charge model and the hydrogen termination model. The light blue spheres in the hydrogen termination model are hydrogen atoms.

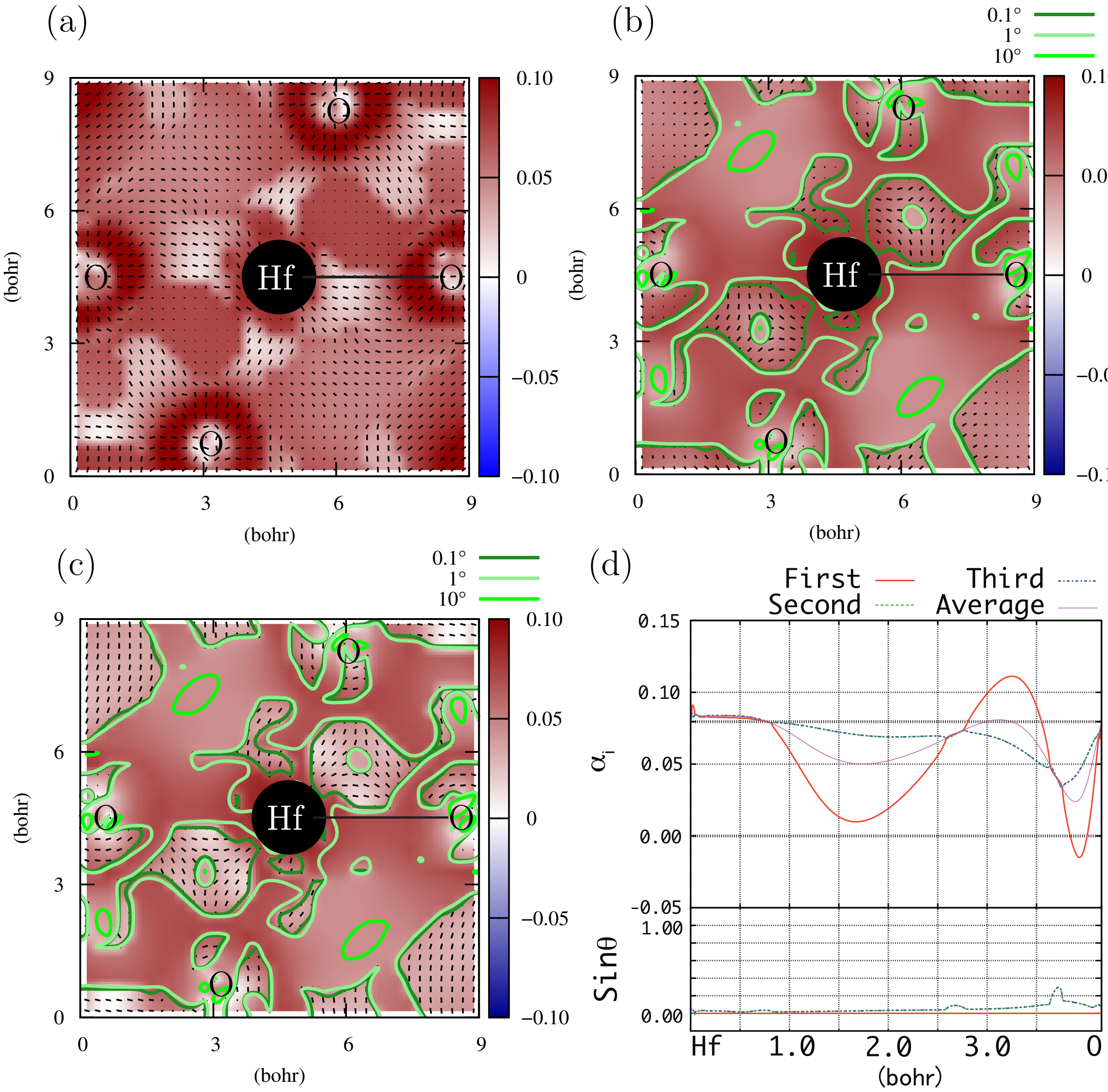

Figure 2: The eigenvalues and eigenvectors of the polarizability density tensor of the point charged model. Panels (a)-(c) show the eigenvalues, the eigenvectors, and the arguments on the plane with one hafnium atom at the center of the model and four next oxygen atoms. The solid line segments show the directions of the eigenvectors. The eigenvalues in the green contours show complex values. The black blob at the center shows the pseudopotential of the Hf atom. Panel (d) shows the eigenvalues and their average on the Hf-O line, which is shown in panels (a)-(c) as the solid line. The upper part of this panel is the real part of three eigenvalues and their average. The horizontal dotted line is drawn for $1/4\pi$. The lower part of this panel is the argument.

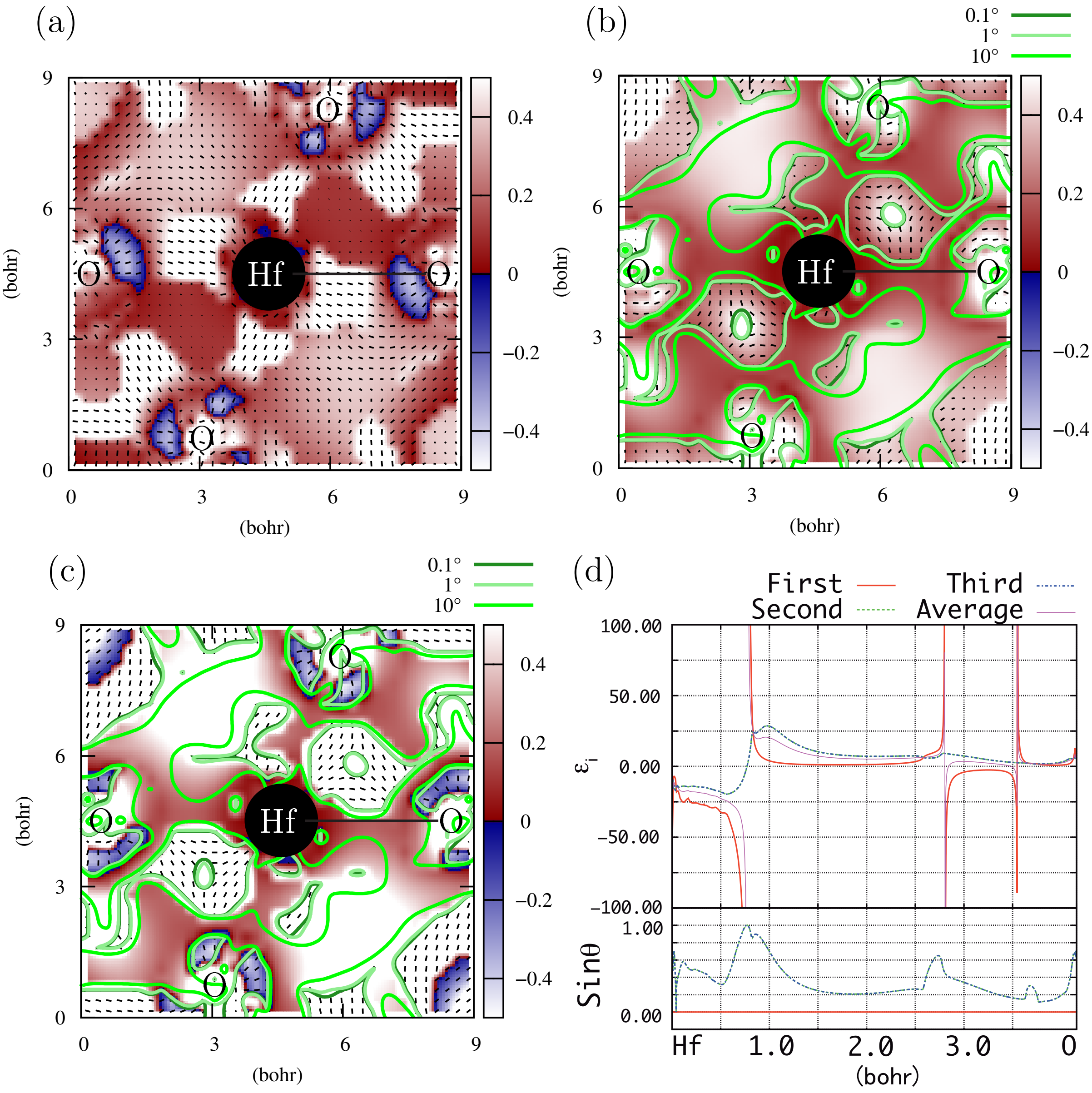

Figure 3: The inverse of eigenvalues and their eigenvectors of the dielectric constant density tensor of the point charged model. Panels (a)-(c) show the inverse of the eigenvalues, the eigenvectors, and the arguments on the same plane as Fig. 2. The solid line segments show the directions of the eigenvectors. The eigenvalues in the green contours show complex values. The black blob at the center shows the pseudopotential of the Hf atom. Panel (d) shows the eigenvalues on the Hf-O line, which is shown in panels (a)-(c) as the solid line. The upper part of this panel is the real part of three eigenvalues and their average, while the lower part of this panel is the argument.

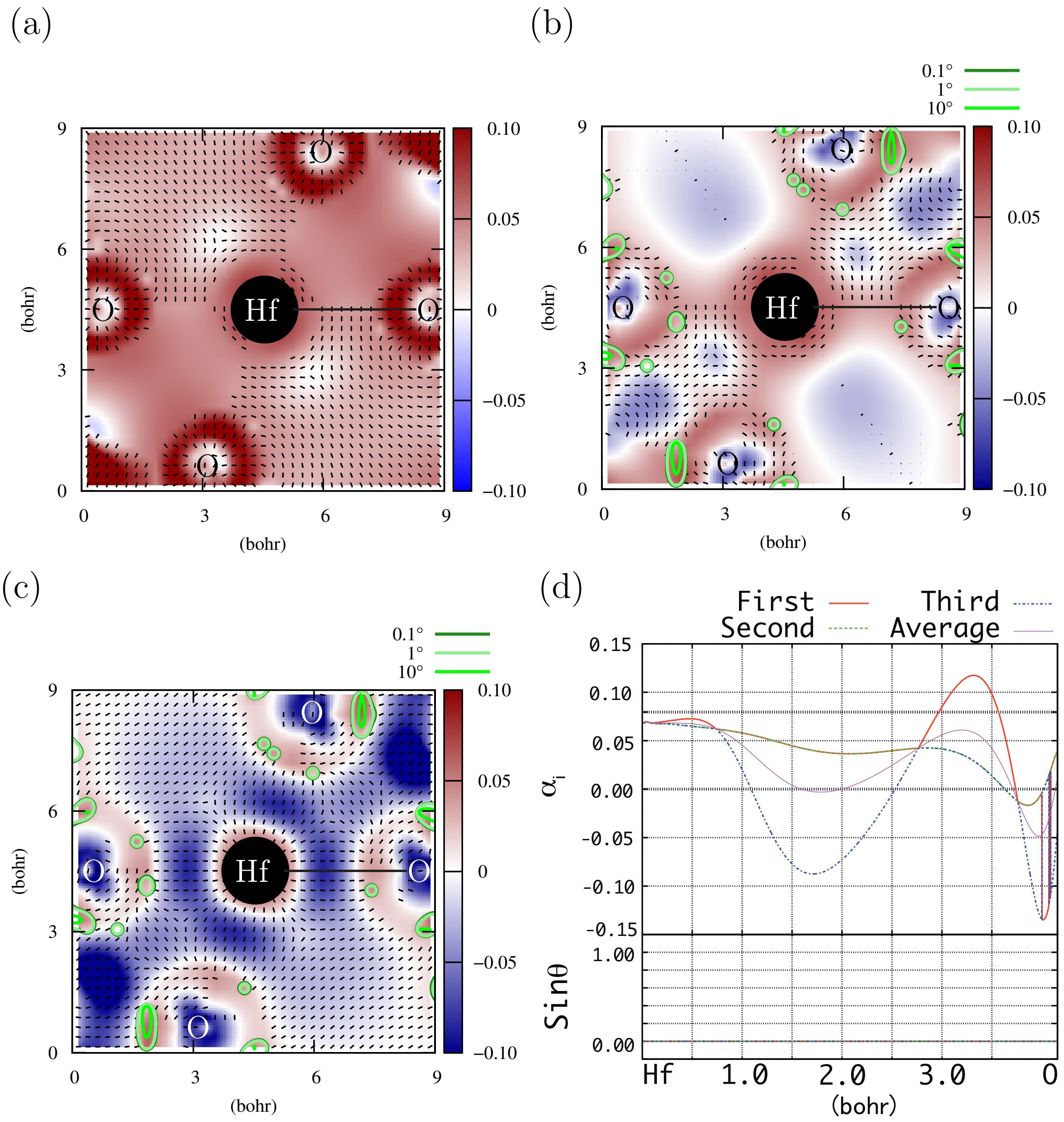

Figure 4: The eigenvalues and eigenvectors of the polarizability density tensor of the hydrogen termination model. Panels (a)-(c) show the eigenvalues, the eigenvectors, and the arguments on the plane with one hafnium atom at the center of the model and four next oxygen atoms. The solid line segments show the directions of the eigenvectors. The eigenvalues in the green contours show complex values. The black blob at the center shows the pseudopotential of the Hf atom. Panel (d) shows the eigenvalues and their average on the Hf-O line, which is shown in panels (a)-(c) as the solid line. The upper part of this panel is the real part of three eigenvalues and their average. The horizontal dotted line is drawn for $1/4\pi$. The lower part of this panel is the argument.

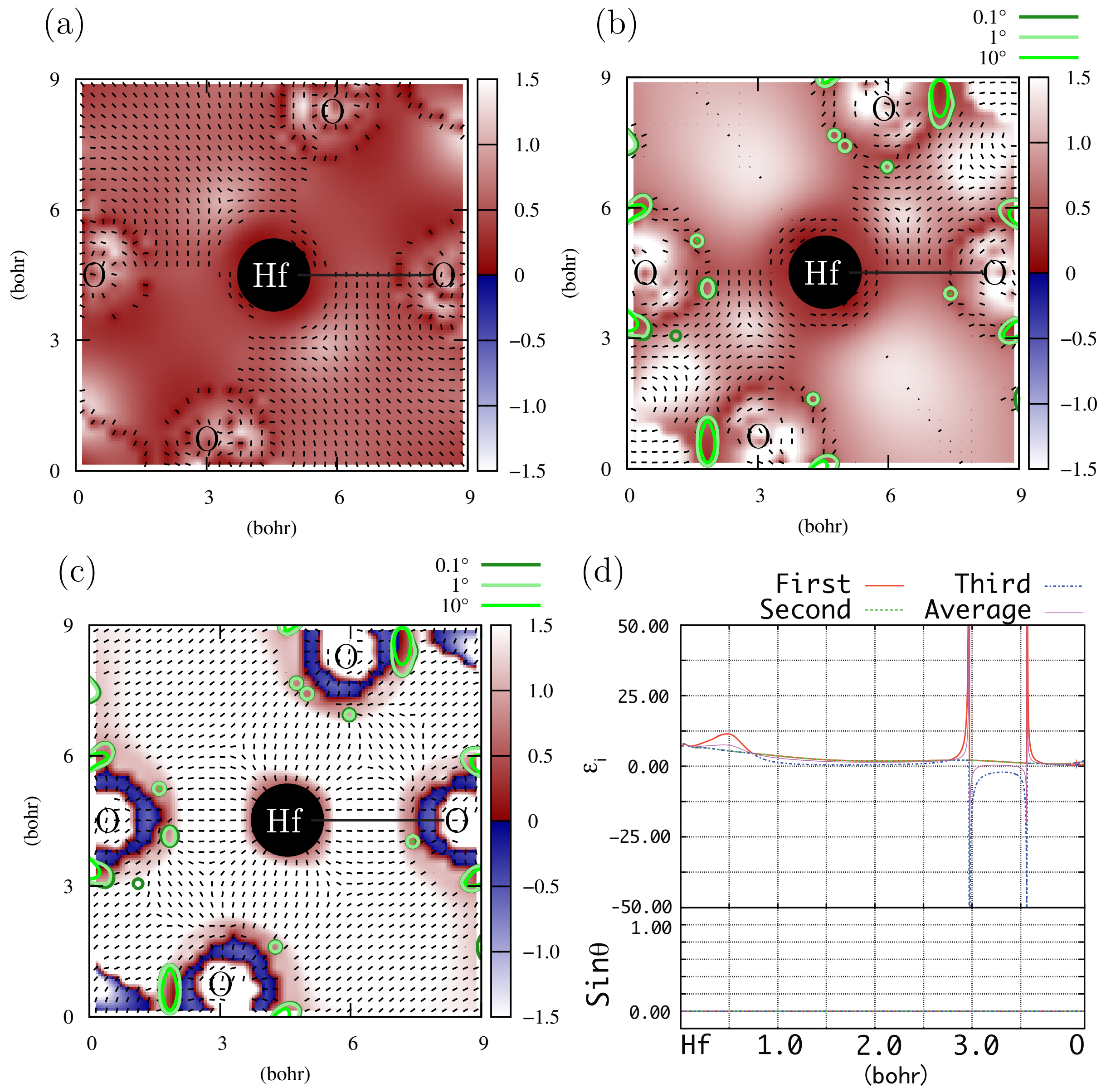

Figure 5: The inverse of eigenvalues and their eigenvectors of the dielectric constant density tensor of the hydrogen termination model. Panels (a)-(c) show the inverse of the eigenvalues, the eigenvectors, and the arguments on the same plane as Fig. 4. The solid line segments show the directions of the eigenvectors. The eigenvalues in the green contours show complex values. The black blob at the center shows the pseudopotential of the Hf atom. Panel (d) shows the eigenvalues and their average on the Hf-O line, which is shown in panels (a)-(c) as the solid line. The upper part of this panel is the real part of three eigenvalues and their average, while the lower part of this panel is the argument.

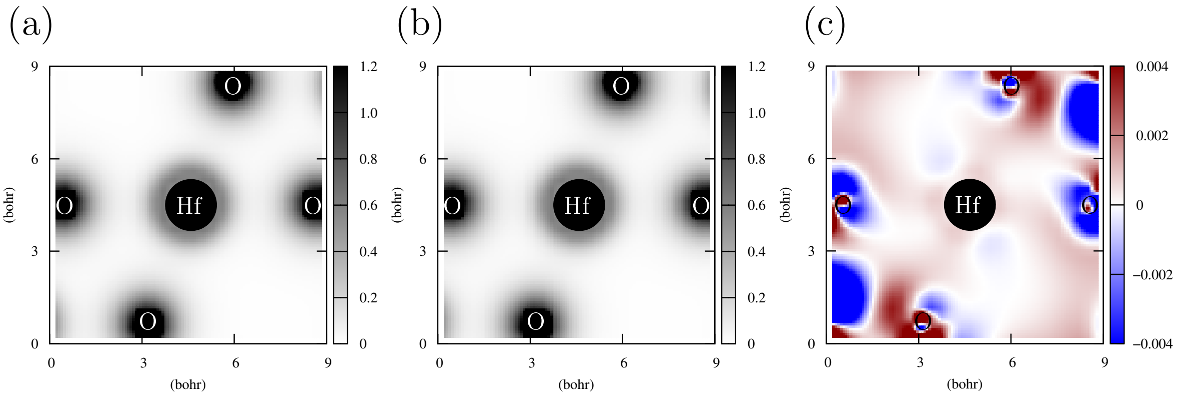

Figure 6: The electron density of the point charge model (ρ_{PC}) (a), the model with hydrogen termination (ρ_{HT}) (b), and the difference of the electron density (ρ_{PC} - ρ_{HT}) (c). The filled circle at the center shows the pseudopotential of the Hf atom.

Chapter 4

Local dielectric property of hafnium and lanthanum atoms in HfLaO$_x$

I Introduction

Hafnia is a promising candidate for an alternative gate insulator of field-effect transistor [1, 2]. Some issues to resolve are known for HfO_2 gate thin films, such as the low crystallization temperature and the instability of the threshold voltage caused by the Fermi level pinning [3]. Particularly, recent studies revealed that oxygen vacancies in HfO_2 films caused the threshold voltage shift in polycrystalline silicon (poly-Si)/HfO_2 gate structures[4, 5]. Shiraishi *et al.* suggested that oxygen vacancies near the Si/HfO_2 interface in a p+poly-Si/HfO_2 gate structure caused reduction of the effective work function of the gate insulator and the formation of oxygen vacancies in HfO_2 films significantly deteriorated their performance[5].

The incorporation of lanthanum into hafnium oxide has attracted attention as a solution of these problems. Yamamoto *et al.* have shown that the introduction of La_2O_3 into HfO_2 rises the crystallization temperature without lowering the permittivity[6]. Wang *et al.* have reported that the incorporation of lanthanum into hafnium oxide suppresses the Fermi level pinning[7, 8]. This improvement is considered to originate in the suppression of oxygen vecancies. Following these works, Umezawa *et al.* have reported that introduced lanthanum atoms bond to oxygen atoms more strongly than hafnium atoms by first principles calculations[9].

In our previous work[10, 11], the static dielectric property of lanthanum oxide clusters has been studied using the local dielectric constant density tensor of electrons, which is defined by one of the authors[12, 13]. We have shown the local dielectric constant of $La(OH)_4$ and a lanthanum silicate cluster. As a result, it is found that the dielectric property of the $La(OH)_4$ cluster becomes similar to that of the $Hf(OH)_4$ cluster by doping a negative charge to the $La(OH)_4$ cluster.

In this work, we investigate the electronic contribution to the local static dielectric properties of the lanthanum oxide and the hafnium oxide, and the effect of the incorporation of the lanthanum oxide into the hafnium oxide on the local dielectric property. In particular, we pay attention to the features, the incorporation of the lanthanum into hafnia suppresses the production of the oxygen vacancy and does not lower the dielectric constant of the hafnia. For this study, we discuss the difference between La-O and Hf-O bonds from atomic viewpoints by quantum ab initio calculation. The formation of an oxygen vacancy is necessarily accompanied with breaking a chemical bond between a metallic atom and an oxygen atom. Hence, we study bonding states of a metallic atom with oxygen atoms. The dielectric properties are investigated in terms of the static dielectric constant density and polarizability density tensors of electrons. The study by our local quantities is efficient for the analysis of the effect of impurities. By using these local quantities, we show one of the reasons why the dielectric constant of the hafnia is not lowered by the incorporation of lanthanum atoms. Of course, it is known that the lattice contribution to the dielectric constant dominates over the electronic contribution and depends on the model structure compared to the electronic contribution[14, 15]. Nevertheless, the effect of the electronic polarization is worth investigating, since the calculations of the electronic contribution have less ambiguity than the lattice contribution and are easy to handle, before we study the lattice contribution.

II Dielectric Constant Density Tensor

First, we show our formulation of the dielectric constant density operator, which is defined in the Rigged QED theory [12, 13]. The system (A) for analyses is embedded in an environmental background medium (M). The corresponding scalar potentials are given as the regional integrals of the electrical charge,

$$\hat{A}_{0_{A,M}}(\vec{r}) = \int_{A,M} d^3\vec{s}\,\frac{\hat{\rho}(\vec{s})}{|\vec{r}-\vec{s}|}, \tag{1}$$

where $\hat{\rho}(\vec{r}) \equiv -e\hat{\psi}^{\dagger}(\vec{r})\hat{\psi}(\vec{r})$ is the charge density operator. The electric field $\hat{\vec{E}}(\vec{r})$ is given as the sum of the electric displacement $\hat{\vec{D}}(\vec{r})$ of the medium and the polarization $\hat{\vec{P}}(\vec{r})$ of the electrons in the system,

$$\hat{\vec{E}}(\vec{r}) = \hat{\vec{D}}(\vec{r}) - 4\pi\hat{\vec{P}}(\vec{r}). \tag{2}$$

These $\hat{\vec{D}}(\vec{r})$ and $\hat{\vec{P}}(\vec{r})$ are defined as follows,

$$\hat{\vec{D}}(\vec{r}) = -\mathrm{grad}\hat{A}_{0_M}(\vec{r}), \tag{3}$$

$$\hat{\vec{P}}(\vec{r}) = \frac{1}{4\pi}\mathrm{grad}\hat{A}_{0_A}(\vec{r}), \tag{4}$$

where the time variation of the vector potential is dropped since we consider only steady states. The electric displacement $\hat{\vec{D}}(\vec{r})$ of the medium is interpreted as the external electric field for the system.

Since the polarization of the electrons in the system is the linear response to $\hat{\vec{D}}(\vec{r})$, it is given as

$$\hat{\vec{P}}(\vec{r}) = \hat{\vec{\alpha}}(\vec{r})\hat{\vec{D}}(\vec{r}), \tag{5}$$

where $\hat{\vec{\alpha}}(\vec{r})$ is the polarizability density tensor. The static contribution to the dielectric constant density tensor is, therefore, defined as

$$\hat{\vec{D}}(\vec{r}) = \hat{\vec{\epsilon}}(\vec{r})\hat{\vec{E}}(\vec{r}) = \frac{1}{1 - 4\pi\hat{\vec{\alpha}}(\vec{r})}\hat{\vec{E}}(\vec{r}). \tag{6}$$

All elements of these two dielectric tensors have real values, since these tensor operators are Hermite. However, these tensors are not symmetric tensor, and hence, its eigenvalues have three real values, or one real and two complex values. Complex eigenvalues of dielectric constant or polarizability tensor do not mean dissipation and induce a rotational response to an external electric field. The complex eigenvalues are correctly described only in the tensor analysis, since it is caused by off-diagonal elements. Hence, the appearance of complex eigenvalues indicates the necessity that the dielectric constant and the polarizability should be treated as tensor quantity for the study of nano-material. The dielectric constant density tensor and the polarizability density tensor are calculated by Molecular

Regional DFT program package[16], which has been developed in our laboratory.

III Computational Details

III-i Formation energy of oxygen vacancy

In this section, we explain our calculation models and conditions. Electronic states are calculated by using GAUSSIAN03 program package[17]. Figure 1 shows the small cluster models for $\mathrm{La(OH)}_n$ and $\mathrm{Hf(OH)}_n$ ($n = 4 - 8$). By these models, we analyze the strength of the M-O bond (M=La or Hf) depending on the number of the OH groups. On these models of $\mathrm{M(OH)}_n$, we impose the symmetry, T_d, C_{4v}, O_h, C_{3v}, O_h for n = 4, 5, 6, 7 and 8, respectively. The geometrical optimization calculation is performed for M-O and O-H bond lengths (and angles for n = 5 and 7) with keeping the symmetry. In the calculations of these models, we use Møller-Plesset's second-order perturbation theory (MP2)[18–22]. The CEP-31G basis set with effective core potentials is chosen for Hf and La atoms[23, 24], and the 6-31G** basis set is taken for oxygen and hydrogen atoms[25, 26]. For La atoms, unoccupied $4f$ orbitals should be treated as the valence functions, though the fully occupied $4f$ orbitals in Hf atoms are stabilized into deep enough levels and do not affect the chemical bond. In our calculations, $4f$ functions are added for La atoms in terms of the polarization function whose exponent coefficient (α) of the Gaussian function is 0.525 for the CEP−31G basis set[10]. For these cluster models, we calculate the binding energy (E_b) of one OH group, which is defined as

$$E_b = \frac{1}{n}(E[\mathrm{M(OH)}_n] - E[\mathrm{M}] - nE[\mathrm{OH}]), \tag{7}$$

where $E[\mathrm{M}]$, $E[\mathrm{OH}]$, and $E[\mathrm{M(OH)}_n]$ are the total energies of one metallic atom, one OH group, and one $\mathrm{M(OH)}_n$ molecule, respectively.

The large cluster models are used for the study of the formation energy of oxygen vacancies and the local dielectric property of La_2O_3 and HfO_2. These models are shown in Fig. 2. The left panel is the La_2O_3 cluster model and the right one is the HfO_2 cluster model. These cluster models of La_2O_3 and HfO_2 are based on their hexagonal and monoclinic crystal structures, respectively. In order to realize their condensed phases, where nuclei and electrons are influenced by the surrounding atoms, we put point charges on surrounding atom sites. In other words, these cluster models are embedded in point charges, which represents that the analyzed system in a large crystal is surrounded by other atoms in the crystal. We put about 2000 (La_2O_3) and 2800 (HfO_2) point charges around the cluster models. The values of these point charges are determined so that the Mulliken charges of the atoms in the analyzed system are uniformly distributed. As a result, the charges for the La_2O_3 model are determined as 0.3 for La sites and -0.2 for oxygen sites, while those for the HfO_2 model are 1.0 for Hf sites and -0.5 for oxygen sites, respectively.

First, we calculate the formation energy (E_f) of an oxygen vacancy for these cluster models. The formation energy is defined as

$$E_f = E_{\mathrm{v}} + \frac{1}{2}E[\mathrm{O}_2] - E_0, \tag{8}$$

where E_{v}, $E[\mathrm{O}_2]$, and E_0 are the total energies of the cluster with an oxygen vacancy, one oxygen molecule, and the cluster without the vacancy, respectively. The oxygen vacancy is set on the center of these models, i.e., the total energy is calculated by removing the central oxygen atom. The total energy calculation is performed by the density functional theory (DFT) based on the Lee-Yang-Parr gradient-corrected functional[31, 32] with Becke's three hybrid parameters [33] (B3LYP). The basis functions are chosen as LanL2DZ[27–30] for La and Hf atoms and D95** for O and H atoms[27]. In addition, we add $4f$ polarization functions to that of lanthanum atom, whose exponent coefficients is 0.441 for the LanL2DZ basis set[10].

III-ii Local polarizability and dielectric constant densities

The Hartree-Fock (HF) method is used to derive the electronic state for the dielectric constant density tensor calculation, since the DFT is known to overestimate the dielectric constant [34–38]. The basis functions are taken as the same to the energy calculation. The dielectric constant density tensor is calculated for these electronic states by using Molecular Regional DFT program package[16]. In this work, the external electric field $\vec{D}(\vec{r})$ is assumed to be universal vector, $\vec{D}$. The calculation procedure of the dielectric constant density tensor is summarized as follows. First we calculate electronic states with two different external electric fields $D^i_{1,2}$ ($i = x, y, z$). (We take $D^i_{1,2} = \pm 0.001$ a.u. in this work). This calculation is carried out for three directions. The scalar potential and polarization are calculated by eqs. (1) and (4) for these electronic states. The difference of the polarization $[\Delta\vec{P}^i(\vec{r})]$ between these two results is divided by the difference of the external fields ($\Delta D^i \equiv D^i_1 - D^i_2$), and thus, the polarizability density tensor can be derived as

$$\Delta P^i(\vec{r}) = \alpha^{ij}(\vec{r})\Delta D^j. \tag{9}$$

Only the response to external fields can be extracted by this procedure. For the dielectric constant density tensor, we calculate only the eigenvalues (and their eigenvectors). These are easily derived by eq. (6) after the eigenvalues of the polarizability density tensor are calculated. Note that the lattice polarization effects have not been included in this calculation, though the quantum states of nuclei are well defined in the Rigged QED.

We also study the effects of the lanthanum incorporation by using the HfLaO$_x$ cluster model, which shown in Fig. 3. The structure is based on the model used by Umezawa *et al.*[9], in which the hafnium oxide has the cubic structure as reported by Yamamoto *et al.*[6] We put about 560 point charges around the cluster model, whose surroundings are assumed as the cubic HfO$_2$ structure without lanthanum atoms. The value of charges are taken as 0.6 for Hf sites and -0.3 for oxygen sites. Other calculation conditions are taken as the same for La_2O_3 and HfO_2 cluster models.

To display eigenvalues of the polarizability and dielectric constant density tensor, we defined the order of them as follows. When all eigenvalues are real, the order of the eigenvalues is the descending order of their values. On the other hand, when the eigenvalues include complex values, the real eigenvalue is set as the first one and two complex values are the second and third ones. The magnitude of the imaginary part is represented by the argument (θ) defined as follow,

$$\theta = \cos^{-1}\left[\frac{|\mathrm{Re}(\lambda_i)|}{|\lambda_i|}\right], \tag{10}$$

where λ_i is the corresponding eigenvalue.

As an advantage of our density quantity, we can also calculate the local averages of the polarizability density and the dielectric constant density, which mean the contributions to these values of a whole material from the corresponding region. Hence, we can compare contributions from some particular regions. To calculate the averages, we consider a region with the volume, V, and integrate the local polarizability density as follows,

$$\langle\vec{\alpha}\rangle = \frac{\int_V \hat{\vec{\alpha}}(\vec{r})dV}{V}. \tag{11}$$

This result is the average polarizability of the region, V, since this integration is given as the integration of the polarization density of the region, V, and the constant $1/D^i$. Then, the average of the dielectric constant is given by

$$\langle\vec{\epsilon}\rangle = \frac{1}{1-4\pi\langle\vec{\alpha}\rangle}. \tag{12}$$

In this work, we investigate the contributions from two particular regions. One is the contribution from the region around an oxygen atom and the other is the contribution from the metal-oxygen bond, i.e., the region between metal and oxygen atoms. Of course, if we calculate the average of the unit cell of a crystal material, we can know the dielectric constant of the material. However, the cluster models in this work are not so large, and hence, we cannot calculate the averages of the unit cell. The integration regions are chosen as follows, for these two contributions. First, for the region around an oxygen atom, the sphere whose radius is the metal-oxygen distance is chosen for the oxygen atom at the center of a model. For the contribution from the bond region, the cylinder is chosen, whose radius is 1.0 bohr and axis is the line between the central oxygen atom and a next metal atom

IV Results and Discussion

Results of E_b are shown in Table 1. These results show that E_b of $\mathrm{Hf(OH)}_n$ are larger than those of $\mathrm{La(OH)}_n$ for n = 4-7, while this trend is reversed for n = 8. This can be considered to be one of the reasons why the cubic structure is favored in the HfO_2 with the lanthanum incorporation[6]. Since Hf atoms are bonded to eight oxygen atoms in the cubic structure of HfO_2 crystal, HfO_2 is deformed into the cubic phases by the larger binding energy of the lanthanum atoms. Since lanthanum atoms are more strongly bonded to oxygen atoms in the cubic phase than Hf atoms, the incorporation of the La atoms also suppresses the production of oxygen vacancies.

The results for the formation energy of the oxygen vacancy are shown in Table 2. The central oxygen atom is removed for this calculation. Our results of the formation energy are roughly consistent with those of previous works[9, 39]. Our results show that E_f of La_2O_3 is slightly smaller than that of HfO_2, though the previous work[39] reported these two values were almost the same. Our result, the Hf-O bond is stronger than the La-O one, is consistent with the results for the small cluster model, $\mathrm{M(OH)}_n$ ($n < 8$).

In Figs. 4 and 5, the polarizability density tensor are shown for the large cluster models of La_2O_3 and HfO_2. The results are shown on a plane with the central oxygen atom and a next metal atom. The solid line segments show the directions of the eigenvectors. The filled circle shows the pseudopotential of the metal atom. The eigenvalues in the green contours have complex values. We show the absolute value of the complex eigenvalues and their arguments in the figure. Panels (a)-(c) show the first, second, and third eigenvalues ($\alpha_{1,2,3}$), respectively. Panel (d) shows all eigenvalues and their average, on the line between the metal and oxygen atoms, which is explicitly shown in panels (a)-(c).

Comparing Figs. 4 and 5, the similarity between them can be seen clearly. The large polarizability density is distributed uniformly in the almost whole region for the first eigenvalue. Especially, the larger values concentrate around the oxygen atoms. The polarizability near oxygen (accepter) atoms is larger than that near metal (donor) atoms. The electrons around metal atoms weakly respond to external electric fields, since electrons are tightly bounded by the metal atom due to the reduced number of screening electrons and the electric field between the metal and oxygen atoms by the charge transfer. On the other hand, the response of electrons around oxygen atoms to the external electric fields is strong due to the weak bound in the oxygen atom by the increased number of screening electrons. As a distinct feature in the figures for the second and third eigenvalues, the complex eigenvalues are also seen in some regions. As mentioned above, the direction of the polarization response to an external field is not the same direction of the external field, i.e., the polarization response has rotational behavior. Larger arguments result in larger angles of this rotational response. Although this rotational response is not seen for large crystal, the response in local regions can have rotational behavior. This rotational response can never be analyzed in the global scalar polarization analysis. The local and tensor analysis is mandatory as stressed above. These similarities as above are considered to be key ingredients that the permittivity of HfO_2 is not lowered by the lanthanum incorporation, though these structures of our models is hexagonal (La_2O_3) and monoclinic (HfO_2).

Next, we pay attention to the difference between the results of La_2O_3 and HfO_2. By comparing Figs. 4 and 5, the polarizability density of La_2O_3 is larger than that of HfO_2. In particular, the large value $\gtrsim 1/4\pi$ is seen to be distributed widely in the result of La_2O_3, while it is very restricted around oxygen atoms for HfO_2. Particularly, this can be clearly seen in Figs. 4(d) and 5(d). The dielectric constant density is divergent and changes the sign at $\alpha_i = 1/4\pi$ as seen in eq. (6). Hence, the regions where $\alpha_i \sim 1/4\pi$ give divergently large dielectric constant density, and the internal polarization cancels out with an external electric field. For the regions where $\alpha_i > 1/4\pi$, the internal polarization overcomes the external electric field, and then, the net internal electric field turns out to be opposite direction to the external field. These phenomena are discussed further in the later. For the third eigenvalue of HfO_2, the negative polarizability can be seen in some regions, especially, around the Hf atom. In these regions, the polarization response to an external field has the opposite direction. Although this opposite direction response cannot occur as an average response of macroscopic material, this can do due to a complicated electronic response around an atom in a local region. However, we consider that this response in our result is attributed to an insufficient accuracy of our calculations. This lack of accuracy of the polarizability density is not serious for the analysis of the dielectric constant density. This is because the regions where the value of the polarizability density is around $1/4\pi$, are important for dielectric constant as discussed later, and the negative polarizability density gives only negligibly small dielectric constant density.

In Tables 3 and 4, we show the average of the polarizability density around the central oxygen atom and between the metal and oxygen atoms, respectively. As shown in Table 3, the average for the La_2O_3 model is 0.057 and that for the HfO_2 model is 0.041, around the central oxygen atom. On the other hand, between the metal and oxygen atoms, the averages for the La_2O_3 and HfO_2 models are 0.033 and 0.026, respectively. In both models, the averaged polarizability between the metal and oxygen atoms is smaller than that around the central oxygen atom. This may mean that the contribution to the global polarizability of the whole material from the electrons around the bond region is less than that around the oxygen atoms. It may be speculated the reason why the move of the electrons around the central oxygen atom is easier than that around the bond region. For the La_2O_3 model, the first and second eigenvalues are much larger than the third eigenvalue, while the first eigenvalue is much larger than the second and third eigenvalues for the HfO_2 model. These features are due to the local structure of the models. The average value of the La_2O_3 is larger than the HfO_2 model. This originates in the difference of the first and second eigenvalues.

In Figs. 6 and 7, the inverse of the dielectric constant density tensor is shown for the La_2O_3 and HfO_2 models. The results are shown on the same plane as Figs. 4 and 5. Panels (a)-(c) show the inverse of the first, second, and third eigenvalues ($\epsilon^{-1}_{1,2,3}$), respectively. The solid line segments show the directions of the eigenvectors. The filled circles show the pseudopotential of the metal atoms. The eigenvalues in the green contours have complex values. We show the absolute value of the complex eigenvalues and their arguments in the figures. Panel (d) shows all eigenvalues and their average, on the line between the metal and oxygen atoms, which is explicitly shown in panels (a)-(c).

Comparing Figs. 6 and 7, the similarity between them can clearly be seen as the polarizability density tensor. The large value of dielectric constant density is uniformly distributed in the almost whole region for the first eigenvalues. In the results for third eigenvalues, the large negative dielectric constant density can be seen. For the regions, the internal electric fields turns out to have opposite directions to the external fields, since the internal polarizations overcome the external electric fields. Of course, the averaged dielectric constants of macroscopic materials do not have negative value. However, the large response can be allowed in restricted local regions. Hence, this property cannot also be described in the averaged global scalar analysis, and it requires that the dielectric property of nanosize material should be analyzed by the local quantity. Due to the similarity of the polarizability around oxygen atoms, the dielectric constant density is also similar to each other. The large negative and positive response of the radial direction and weaker positive response of the angular directions. Around metal atoms, the similarity between these two atoms also remains due to the similarity of the polarizability. The large dielectric constant density appears between the metal and oxygen atoms. In our previous study[10, 11], the $La(OH)_4$ cluster has different dielectric constant density property compared to $Hf(OH)_4$, and the doping the charge into $La(OH)_4$ makes the dielectric constant density similar to that of $Hf(OH)_4$. Hence, it is considered that the lanthanum atom in the larger cluster of this work receives charges from the surroundings. Since these larger models are far better than the previous isolated cluster models, we conclude that dielectric property of the lanthanum oxide is similar to that of the hafnium oxide. As a result, these similarities of dielectric property may also be one of the reasons why the permittivity of HfO_2 is not lowered by the lanthanum incorporation.

Then, we mention the difference of the dielectric constant density between La_2O_3 and HfO_2. The dielectric constant density of La_2O_3 is larger than that of HfO_2 as the polarizability density. In addition, the region with negative dielectric constant density is wide. In our previous study[10, 11], the area of negative dielectric constant density are also large for the $La(OH)_4$ cluster model compared to the $Hf(OH)_4$ model. Since the density of states of the small cluster models, $M(OH)_4$, and the large ones in this work, were roughly similar to each other, we consider that this may be an essential difference between the lanthanum and hafnium oxides.

In Tables 3 and 4, we also show the averages of the local dielectric constants around the central oxygen atom and between the metal and oxygen atoms, respectively. As shown in Table 3, the average for the La_2O_3 model is 4.72 and that for HfO_2 model is 2.40, around the central oxygen atom. On the other hand, between the metal and oxygen atoms, the averages for the La_2O_3 and HfO_2 models are 2.07 and 2.03, respectively. In both models, the averaged dielectric constants between the metal and oxygen atoms are similar to each other. This similarity is due to the similarity of the bonding states of lanthanum and hafnium. In the computational works[14, 15, 40], the electronic contributions of dielectric constant of the monoclinic structure of the hafnia are reported as about 5. The dielectric constant around bond regions is much less than this value. Therefore, the contribution to the global dielectric constant of the whole material from the electrons around the bond regions may be speculated to be small. As discussed above, the electrons around the bond regions may not be easier to move compared to other electrons. The average values around the oxygen atoms are significantly different between the La_2O_3 and HfO_2 models. This difference originates in the insufficient accuracy of the calculations of the wave function, which is due to the smallness of the basis sets, the usage of the pseudopotential, and so on. By this lack of the accuracy, quantitative results may have an uncertainty. However, we consider that qualitative aspect of our results are enough confident. The importance of the accuracy and the choice of models is also discussed in our previous paper[41].

Finally, the results of the polarizability density and the dielectric constant density of the $HfLaO_x$ model are shown in Figs. 8 and 9, respectively. The results are shown on the plane containing lanthanum and hafnium atoms, and the oxygen atom bonding to these atoms in panels (a), (b), and (c), which are depicted in the same manner as Figs. 5 and 7, respectively. Panels (d) and (e) show the eigenvalues and their average, on the lines between the metal and oxygen atoms, which is explicitly shown in panels (a), (b), and (c). As seen in Figs. 8 and 9, the behaviors of the local polarizability and dielectric constant around the La atom are similar to those around the Hf atom, those of the La_2O_3 model, and those of the HfO_2 model, as expected. Hence, these results confirm that the incorporation of the lanthanum atom does not lower the permittivity of the HfO_2. Comparing Figs. 7 and 9, the dielectric property is seen to be similar to each other. One distinct difference is that the complex value of the polarizability density and the dielectric constant density are seen in larger regions compared to those of the HfO_2 model. One of the reasons is low symmetry of this $HfLaO_x$ model. This means that dielectric responses are very complex and have rotational behavior in the material containing many impurities. Therefore, our local and tensor analysis is extremely suitable for the study of the effects of impurities on the dielectric material.

In Tables 3 and 4, we show the average of the local dielectric constant around the central oxygen atom and between the metal and oxygen atoms, respectively. The integration radius of the sphere around the central oxygen atom is taken as the distance between the central oxygen atom and a next lanthanum atom, since this distance is longer than that between the oxygen atom and a next hafnium atom. The average values of the polarizability and the dielectric constant show intermediate values between those of the La_2O_3 and HfO_2 models. As seen in Tables 4, the dielectric constant of the region between the lanthanum and oxygen atoms is much larger than that between the hafnium and oxygen atoms. This is due to the ease of the move of the electrons in this region, since the lanthanum atom is an impurity for the hafnia. We will confirm our results in more accurate calculations further. The average dielectric constant between the hafnium and oxygen atoms is the value similar to those of the other models. Hence, this result is consistent with the statement that the contribution to the global dielectric constant of the whole material from the electrons around the bond regions is speculated to be small.

V Conclusions

We have investigated the local dielectric property of lanthanum and hafnium oxides using cluster models, and the effects of the lanthanum incorporation on the hafnium oxide has been studied using the local polarizability density and the local dielectric constant density. The relation between the coordinate number and binding energy of M-O (M=La, Hf) bonds have shown that hafnia takes the cubic structure by the incorporation of La_2O_3 in HfO_2 due to the stability of the La-O bonds at eight coordinates compared to the Hf-O one. It is seen that the polarizability and dielectric constant density of La_2O_3 and HfO_2 have many common properties. It can be considered that the incorporation of lanthanum atoms does not lower the permittivity of HfO_2 due to this similarity. Finally, we confirm this speculation by the study of the local dielectric property of the $HfLaO_x$ cluster model. In $HfLaO_x$, the dielectric constant density around the lanthanum atom in the $HfLaO_x$ is similar to those around the hafnium atoms in the $HfLaO_x$ and HfO_2 models. We have also compared the dielectric properties around the central oxygen atom and that between the central oxygen atom and a next metal atom. Our results have shown that the contribution to the dielectric response from the bond regions is not so large. We will check further this property in more accurate calculations.

As future work, we must also take the lattice contribution to the dielectric property as local density quantity in order to reveal the dielectric property of nano-materials, since the lattice contribution to the dielectric constant dominates over the electronic one and depends on the model structure strongly. In addition, more accurate calculations support the clarification of the local dielectric property of nano-materials.

Reference

[1] G. D. Wilk, R. M. Wallace, and L. M. Anthony, J. Appl. Phys. **89**, 5243 (2001).

[2] J. Robertson, Eur. Phys. J. Appl. Phys. **28**, 265 (2004).

[3] S. Zafar, A. Callegari, E. Gusev, and M. V. Fischetti, J. Appl. Phys. **93**, 9298 (2003).

[4] C. C. Hobbs, L. R. C. Fonseca, A. Knizhnik, V. Dhandapani, S. B. Samavedam, W. J. Taylor, J. M. Grant, L. G. Dip, D. H. Triyoso, R. I. Hegde, D. C. Gilmer, R. Garcia, D. Roan, M. L. Lovejoy, R. S. Rai, E. A. Hebert, H.-H. Tseng, S. G. H. Anderson, B. E. White, and P. J. Tobin, IEEE Trans. Electron Devices **51**, 978 (2004).

[5] K. Shiraishi, K. Yamada, K. Torii, Y. Akasaka, K. Nakajima, M. Konno, T. Chikyow, H. Kitajima, and T. Arikado, Jan. J. Appl. Phys. **43**, L1413 (2004).

[6] Y. Yamamoto, K. Kita, K. Kyuno, and A. Toriumi, Appl. Phys. Lett. **89**, 032903 (2006).

[7] X. P. Wang, M. F. Li, A. Chin, C. X. Zhu, J. Shao, W. Lu, X. C. Shen, X. F. Yu, R. Chi, C. Shen, A. C. H. Huan, J. S. Pan, A. Y. Du, P. Lo, D. S. H. Chan, and D. L. Kwong, Solid-State Electron. **50**, 986 (2006).

[8] X. P. Wang, C. Shen, M. Li, H. Y. Yu, Y. Sun, Y. P. Feng, A. Lim, H. W. Sik, A. Chin, Y. C. Yeo, P. Lo, and D. L. Kwong, Tech. Dig. VLSI Symp 2006, p. 12.

[9] N. Umezawa, K. Shiraishi, S. Sugino, A. Tachibana, K. Ohmori, K. Kakushima, H. Iwai, T. Chikyow, T. Ohno, Y. Nara, and K. Yamada, Appl. Phys. Lett. **91**, 132904 (2007).

[10] K. Doi, Y. Mikazuki, S. Sugino, T. Doi, P. Szarek, M. Senami, K. Shiraishi, H. Iwai,

N. Umezawa, T. Chikyo, K. Yamada, and A. Tachibana, Jpn. J. Appl. Phys. **47**, 205 (2008).

[11] P. Szarek, Dr. thesis, Dept. of Micro Engineering, Kyoto University, Kyoto, Japan, 2008.

[12] A. Tachibnana, J. Mol. Modeling **11**, 301 (2005).

[13] A. Tachibana, J. Mol. Struct., THEOCHEM **943**, 138 (2010).

[14] H. Momida, T. Hamada, T. Yamamoto, T. Uda, N. Umezawa, T. Chikyow, K. Shiraishi, and T. Ohno, Appl. Phys. Lett. **91**, 132904 (2007).

[15] H. Momida, T. Hamada, and T. Ohno, Jpn. J. Appl. Phys. **46**, 3255 (2007).

[16] M. Senami, K. Ichikawa, K. Doi, P. Szarek, K. Nakamura, and A. Tachibana: Molecular Regional DFT program package, ver. 3 (Tachibana Lab., Kyoto University, Kyoto, 2008).

[17] Gaussian 03, Revision B.05 (Gaussian, Inc., Pittsburgh, PA, 2003)

[18] M. Head-Gordon, J. A. Pople, and M. J. Frisch, Chem. Phys. Lett. **153**, 503 (1988).

[19] M. J. Frisch, M. Head-Gordon, and J. A. Pople, Chem. Phys. Lett. **166**, 275 (1990).

[20] M. J. Frisch, M. Head-Gordon, and J. A. Pople, Chem. Phys. Lett. **166**, 281 (1990).

[21] M. Head-Gordon and T. Head-Gordon, Chem. Phys. Lett. **220**, 122 (1994).

[22] S. Saebo and J. Almlof, Chem. Phys. Lett. **154**, 83 (1989).

[23] W. J. Stevens, M. Krauss, H. Basch, and P. G. Jasien, Can. J. Chem. **70**, 612 (1992).

[24] T. R. Cundari and W. J. Stevens, J. Chem. Phys. **98**, 5555 (1993).

[25] W. J. Hehre, R. Ditchfield, and J. A. Pople, J. Chem. Phys. **56**, 2257 (1972).

[26] P. C. Hariharan and J. A. Pople, Theor. Chim. Acta **28**, 213 (1973).

[27] C. H. Dunning, Jr. and P. J. Hay, in *Modern Theoretical Chemistry*, ed. H. F. Schaefer III (Plenum, New York, 1976).

[28] P. J. Hay and W. R. Wadt, J. Chem. Phys. **82**, 270 (1985).

[29] W. R. Wadt and P. J. Hay, J. Chem. Phys. **82**, 284 (1985).

[30] P. J. Hay and W. R. Wadt, J. Chem. Phys. **82**, 299 (1985).

[31] C. Lee, W. Yann, and R. G. Parr, Phys. Rev. B **37**, 785 (1988).

[32] B. Miehlich, A. Savin, H. Stoll, H. Preuss, Chem. Phys. Lett. **157**, 200 (1989).

[33] A. D. Becke, J. Chem. Phys. **98**, 5648 (1993).

[34] S. Baroni and R. Resta, Phys. Rev. B **33**, 7017 (1986).

[35] Z. H. Levine and D. C. Allan, Phys. Rev. B **43**, 4187 (1991).

[36] Z. H. Levine and D. C. Allan, Phys. Rev. B **44**, 12781 (1991).

[37] Z. H. Levine and D. C. Allan, Phys. Rev. Lett. **63**, 1719 (1989).

[38] Z. H. Levine and D. C. Allan, Phys. Rev. Lett. **66**, 41 (1991).

[39] J. X. Zheng, G. Ceder, and W. K. Chim, Phys. Status Solidi: Rapid Res. Lett. **2**, 227 (2008).

[40] E. Cockayne, J. App. Phys. **103**, 084103 (2008).

[41] A. Fukushima, M. Senami, Y. Tsuchida, and A. Tachibana, Jpn. J. Appl. Phys. **49**, 111504 (2010).

Table 1: The binding energy of $M(OH)_n$ molecules. The unit of the energy is eV. In the parenthesis, the binding energy per one (OH) group is shown.

Metal atom	n=4	n=5	n=6	n=7	n=8
La	-15.8 (-3.96)	-19.5 (-3.91)	-18.6 (-3.09)	-19.5 (-2.78)	-30.3 (-3.79)
Hf	-23.9 (-5.97)	-22.3 (-4.45)	-24.9 (-4.14)	-20.6 (-2.94)	-24.7 (-3.09)

Table 2: Formation energy of the oxygen vacancy. The unit of the energy is eV.

Model	Formation energy
La_2O_3	5.47
HfO_2	6.22

Table 3: The average of the polarizability and dielectric constant around the oxygen atom at the center of the models.

Models	α_1	α_2	α_3	$\sum_i \alpha_i/3$	ϵ_1	ϵ_2	ϵ_3	$\sum_i \epsilon_i/3$
La_2O_3	0.067	0.067	0.030	0.057	6.28	6.25	1.61	4.72
HfO_2	0.059	0.033	0.030	0.041	3.88	1.70	1.61	2.40
$HfLaO_x$	0.053	$0.044+0.004i$	$0.044-0.004i$	0.047	3.06	$2.22 +0.24i$	$2.22 -0.24i$	2.50

Table 4: The volume average of the polarizability and dielectric constant between the metal and oxygen atoms.

Models	α_1	α_2	α_3	$\sum_i \alpha_i/3$	ϵ_1	ϵ_2	ϵ_3	$\sum_i \epsilon_i/3$
La_2O_3	0.051	0.046	0.000	0.033	2.83	2.38	1.00	2.07
HfO_2	0.058	0.019	0.002	0.026	3.77	1.31	1.03	2.03
$HfLaO_x$(La-O)	0.071	0.066	0.045	0.060	9.34	6.03	2.23	5.88
$HfLaO_x$(Hf-O)	0.058	0.054	-0.013	0.033	3.84	3.09	0.86	2.60

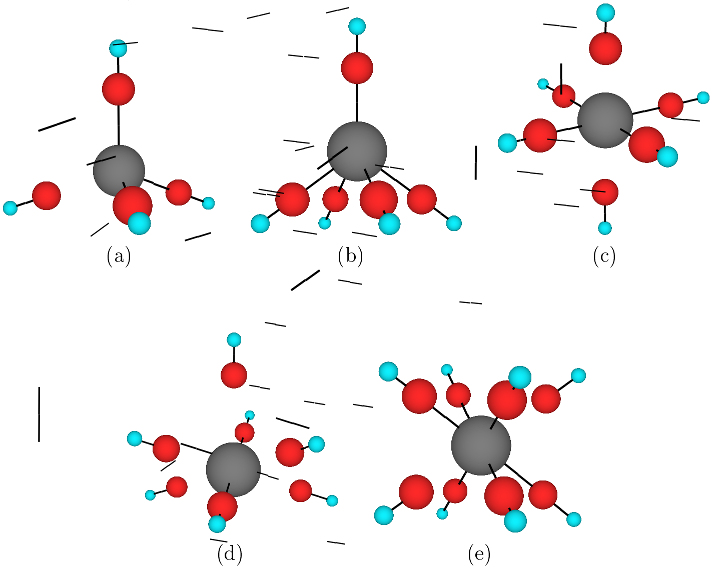
(a) (b) (c) (d) (e)

Figure 1: The small cluster models of $La(OH)_n$ and $Hf(OH)_n$ ($n = 4-8$). The gray (large) spheres mean hafnium or lanthanum atoms. The red (middle) and blue (small) spheres are oxygen and hydrogen atoms, respectively.

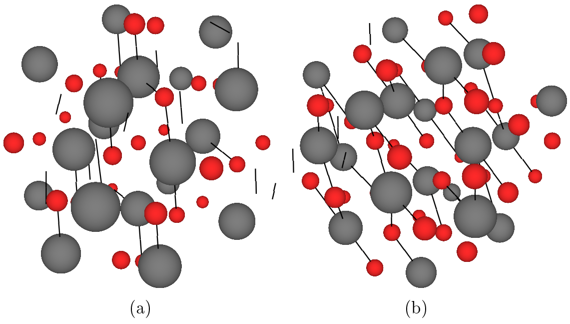
(a) (b)

Figure 2: The large cluster models of La_2O_3 (left) and HfO_2(right). The gray (large) spheres are hafnium or lanthanum atoms and the red (small) ones are oxygen atoms. Point charges surrounding these clusters are not shown in these figures, which mean the medium.

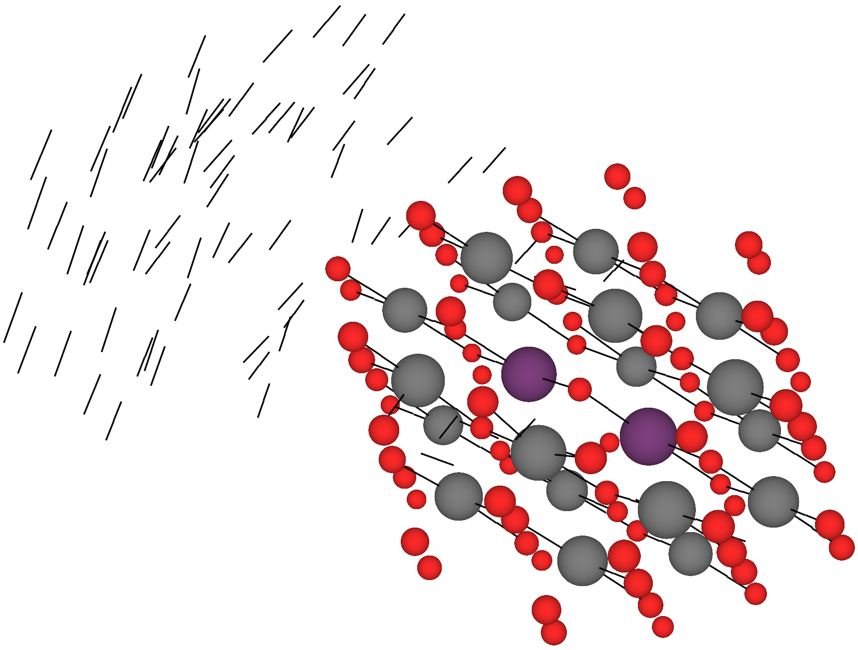

Figure 3: The cluster model of $HfLaO_x$. The gray (large light) and purple (large dark) spheres are hafnium and lanthanum atoms, respectively, and the red (small) ones are oxygen atoms. Point charges surrounding this cluster are not shown.

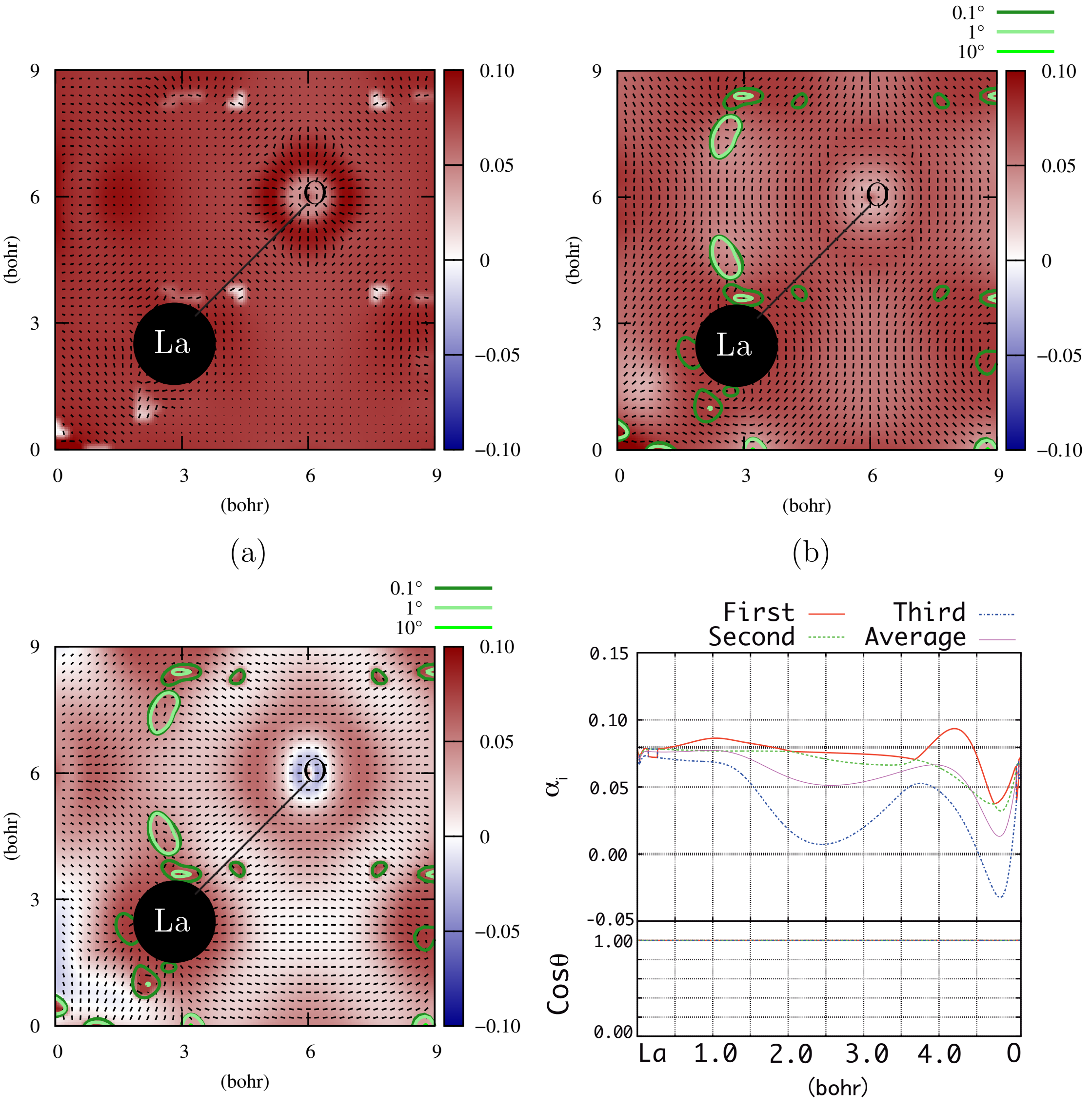

(a) (b)

(c) (d)

Figure 4: The eigenvalues of the polarizability density tensor of the large cluster models of La_2O_3. Panels (a), (b), and (c) are the results of the first, second, and third eigenvalues ($\alpha_{1,2,3}$), respectively, on a plane with the central oxygen atom and a next lanthanum atom. Panels (a)-(c) shows also the eigenvectors and the arguments. The order of values and the definition of the argument is shown in the text. The solid line segments show the directions of the eigenvectors. The filled circle shows the pseudopotential of the La atom. The eigenvalues in the green contours have complex values. We show the absolute value of the complex eigenvalues and their arguments. Panel (d) shows all eigenvalues and their average on the La-O line between the La and O atoms, which is explicitly shown in panels (a)-(c) as the solid line. The upper part of this panel is the real part of three eigenvalues and their average. The horizontal dotted line means $1/4\pi$. The lower part of this panel is the argument.

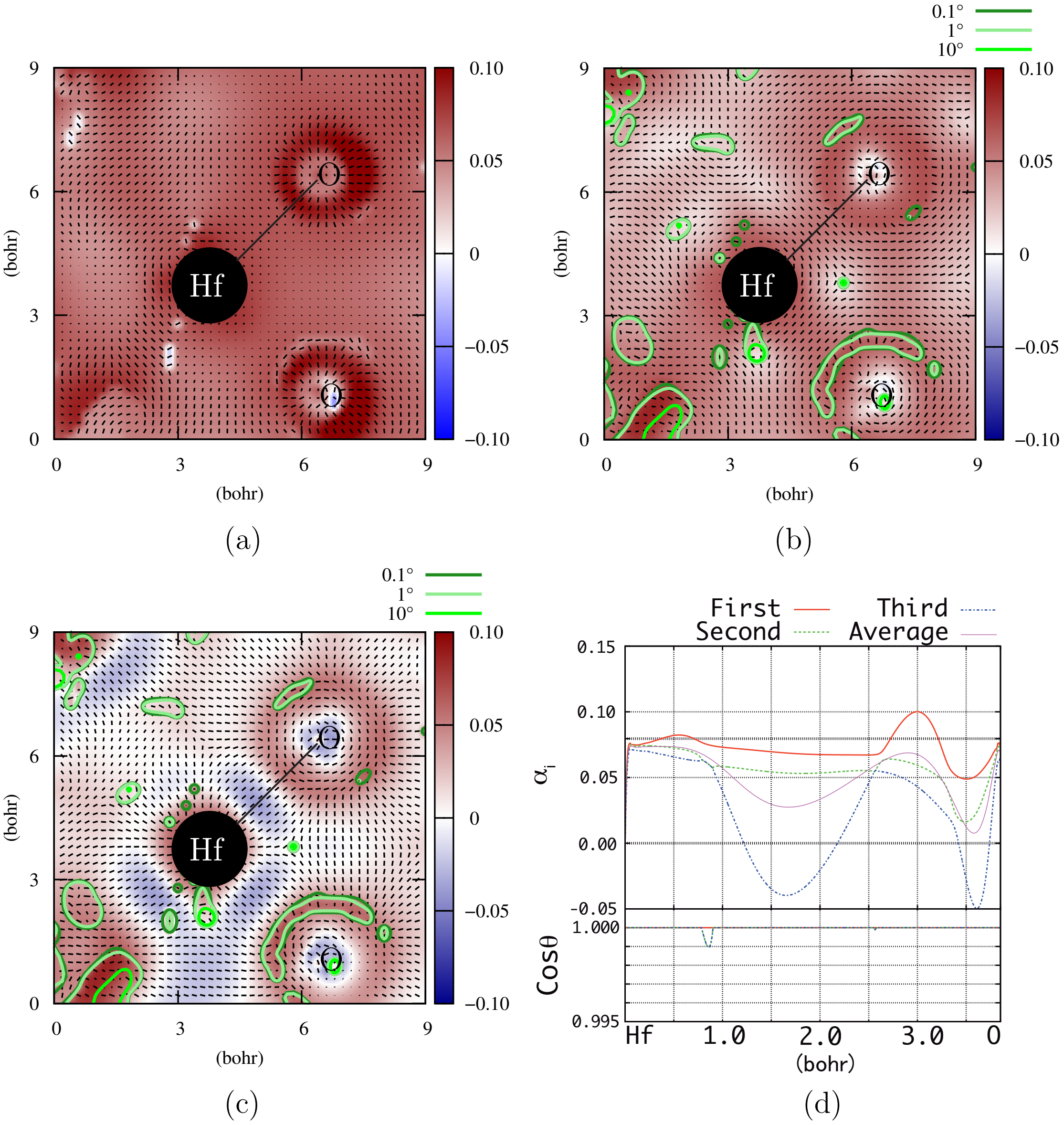

(a) (b) (c) (d)

Figure 5: The eigenvalues of the polarizability density tensor of the large cluster models of HfO_2. Panels (a), (b), and (c) are the results of the first, second, and third eigenvalues ($\alpha_{1,2,3}$), respectively, on a plane with the central oxygen atom and a next lanthanum atom. Panels (a)-(c) shows also the eigenvectors and the arguments. The order of values and the definition of the argument is shown in the text. The solid line segments show the directions of the eigenvectors. The filled circle shows the pseudopotential of the Hf atom. The eigenvalues in the green contours have complex values. We show the absolute value of the complex eigenvalues and their arguments. Panel (d) shows all eigenvalues and their average on the Hf-O line between the Hf and O atoms, which is explicitly shown in panels (a)-(c) as the solid line. The upper part of this panel is the real part of three eigenvalues and their average. The horizontal dotted line means $1/4\pi$. The lower part of this panel is the argument.

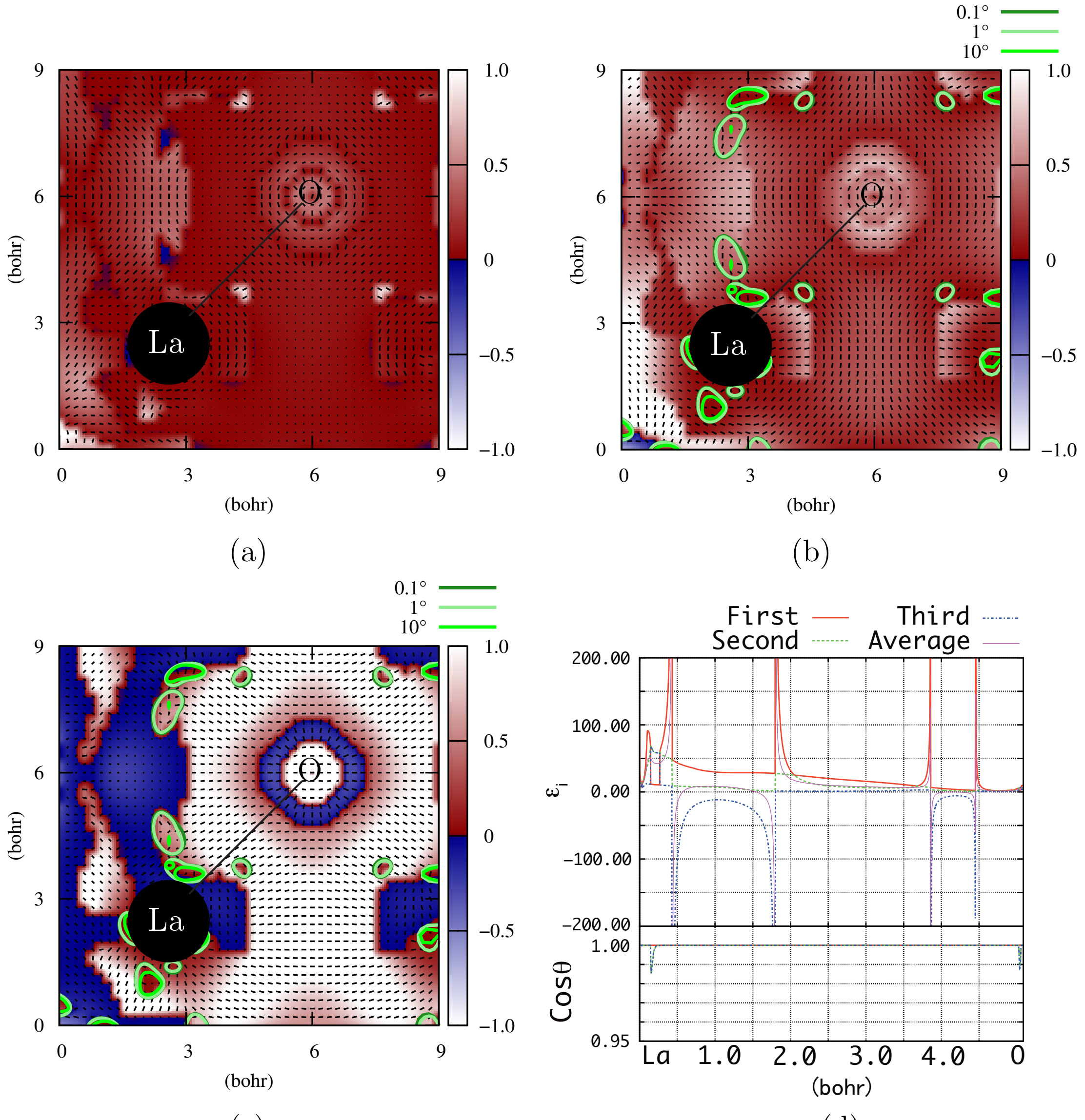

(a) (b) (c) (d)

Figure 6: The inverse of the eigenvalues of the dielectric constant density tensor of the large cluster models of La_2O_3. Panels (a), (b), and (c) show the inverse of the first, second, and third eigenvalues $(\epsilon^{-1}_{1,2,3})$, respectively. on a plane with the central oxygen atom and a next lanthanum atom. Panels (a)-(c) show also the eigenvectors and the arguments. The order of values and the definition of the argument is shown in the text. The solid line segments show the directions of the eigenvectors. The eigenvalues in the green contours have complex values. We show the absolute value of the complex eigenvalues and their arguments. The filled circle shows the pseudopotential of the La atom. Panel (d) shows all eigenvalues and their average on the La-O line which is explicitly shown in panels (a)-(c) as the solid line. The upper part of this panel is the real part of three eigenvalues and their average. The lower part of this panel is the argument.

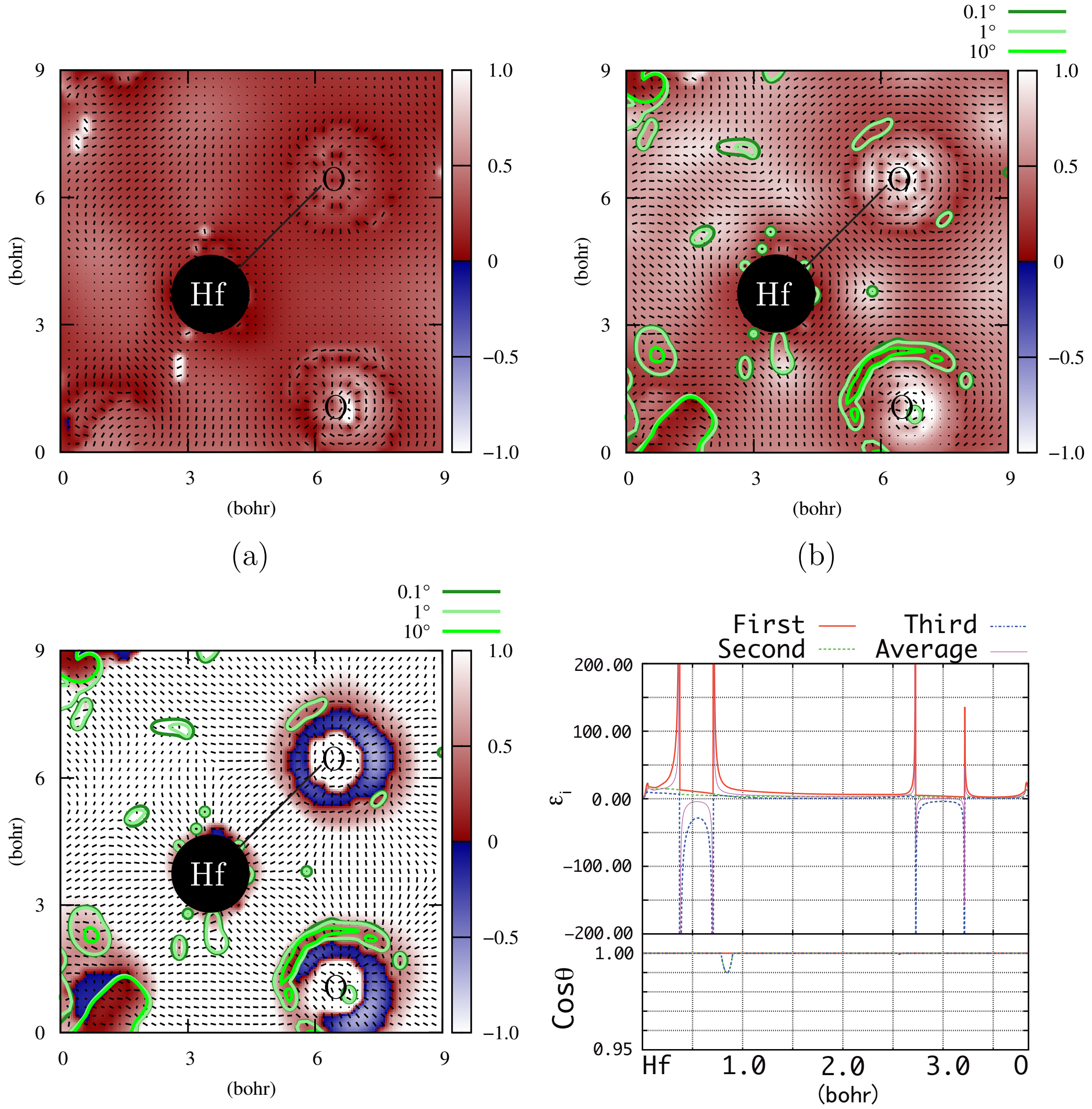

(a) (b) (c) (d)

Figure 7: The inverse of the eigenvalues of the dielectric constant density tensor of the large cluster models of HfO$_2$. Panels (a), (b), and (c) show the inverse of the first, second, and third eigenvalues ($\epsilon^{-1}_{1,2,3}$), respectively. on a plane with the central oxygen atom and a next hafnium atom. Panels (a)-(c) show also the eigenvectors and the arguments. The order of values and the definition of the argument is shown in the text. The solid line segments show the directions of the eigenvectors. The eigenvalues in the green contours have complex values. We show the absolute value of the complex eigenvalues and their arguments. The filled circle shows the pseudopotential of the Hf atom. Panel (d) shows the eigenvalues on the Hf-O line. The upper part of this panel is the real part of three eigenvalues and their average. The lower part of this panel is the argument.

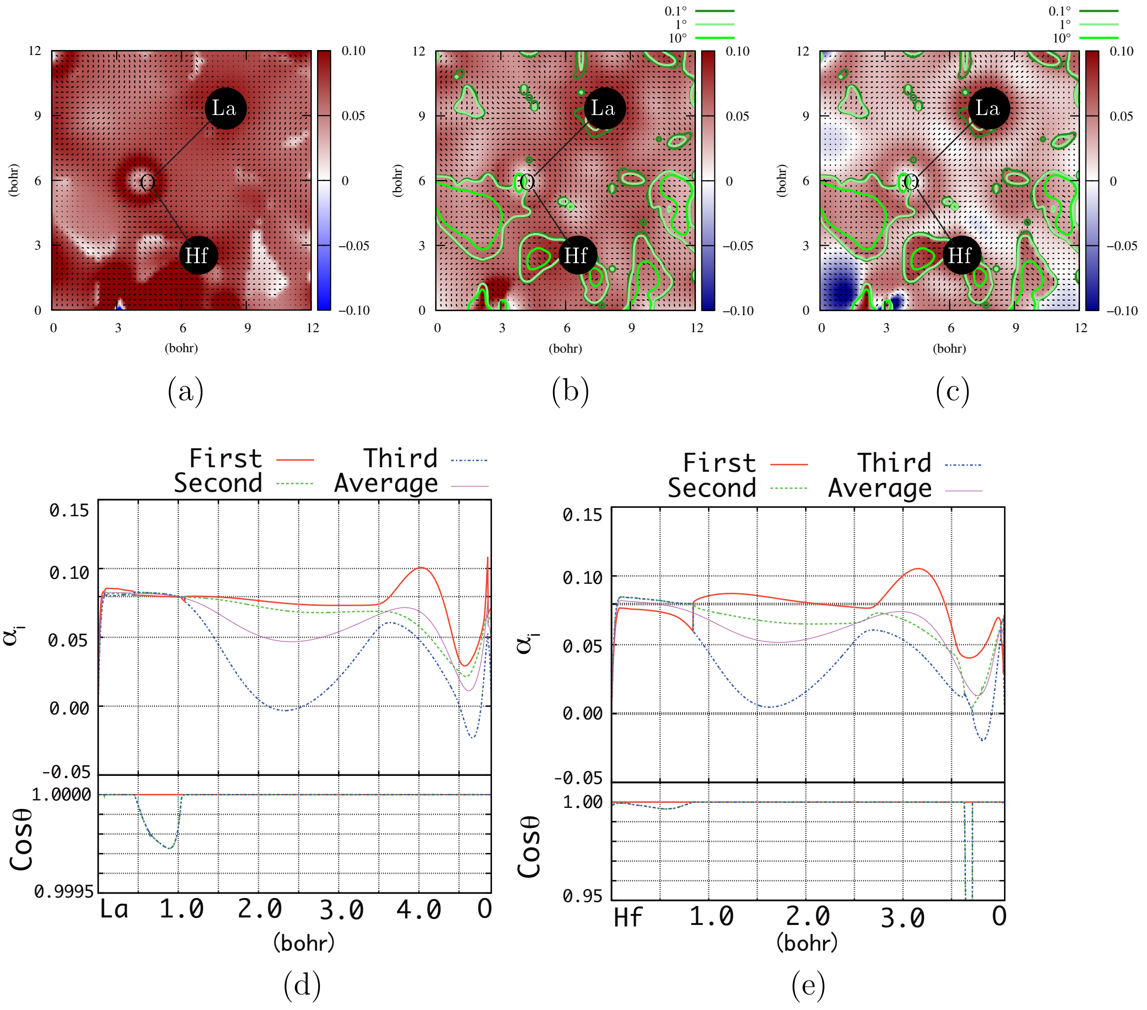

(a) (b) (c)

(d) (e)

Figure 8: The eigenvalues of the polarizability density tensor of the large cluster models of HfLaO$_x$. Panels (a), (b), and (c) are the results of the first, second, and third eigenvalues ($\alpha_{1,2,3}$), respectively, on the Hf-La-O plane. Panels (a)-(c) shows also the eigenvectors and the arguments. The order of values and the definition of the argument is shown in the text. The solid line segments show the directions of the eigenvectors. The filled circles show the pseudopotential of the Hf and La atoms. The eigenvalues in the green contours have complex values. We show the absolute value of the complex eigenvalues and their arguments. Panels (d) and (e) show all eigenvalues and their averages on the La-O and Hf-O lines, respectively. These lines are explicitly shown in panels (a)-(c) as the solid line. The upper part of this panel is the real part of three eigenvalues and their average. The horizontal dotted line means $1/4\pi$. The lower part of this panel is the argument.

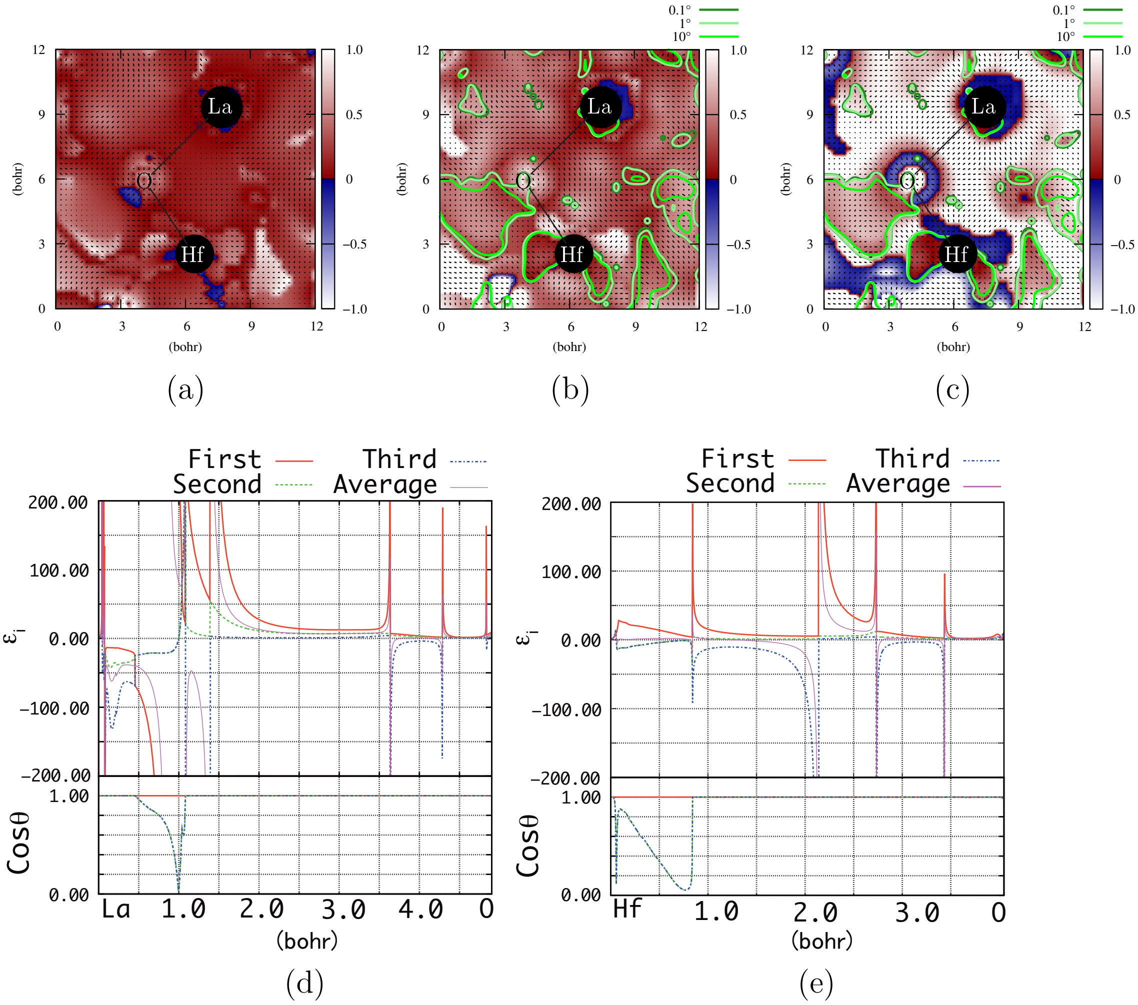

(a) (b) (c)

(d) (e)

Figure 9: The inverse of the eigenvalues of the dielectric constant density tensor of the large cluster models of HfLaO$_x$. Panels (a), (b), and (c) show the inverse of the first, second, and third eigenvalues ($\epsilon^{-1}_{1,2,3}$), respectively. on the Hf-La-O plane. Panels (a)-(c) show also the eigenvectors and the arguments. The order of values and the definition of the argument is shown in the text. The solid line segments show the directions of the eigenvectors. We show the absolute value of the complex eigenvalues and their arguments. The eigenvalues in the green contours have complex values. The filled circles shows the pseudopotential of the Hf and La atoms. Panels (d) and (e) show the eigenvalues on the La-O and Hf-O lines, respectively. The upper part of this panel is the real part of three eigenvalues and their average. The lower part of this panel is the argument.

Chapter 5

A theoretical study on a reaction of iron(III) hydroxide with boron trichloride

by ab initio calculation

I Introduction

In this paper, we investigate a reaction of boron trichloride (BCl_3) with iron(III) hydroxide ($Fe(OH)_3$) by ab initio quantum chemical calculation. The purpose of the paper is two fold. One is to present how $Fe(OH)_3$ reacts in BCl_3 gas which could be relevant to an industrial process. Secondly, by applying newly-developed interaction energy density concept to the reaction, we would like to test its validity in particular regarding its ability to describe stabilization through chemical reaction.

Let us start from describing some industrial background. Boron trichloride is one of the semiconductor gases, which is used, for example, as a preferential plasma etching gas for aluminum and a source of boron for p-type doping in the process of chemical vapor deposition [1–3]. High purity is required for semiconductor gases to be used in the production process of recent high integrated device and thin insulating film. Required impurity level in recent years has been lower and lower. In the future, it is expected to be parts-per-trillion (ppt) level [4]. To achieve lower impurity level, it is necessary to remove all causes which might contaminate the gases in the whole process including gas transportation. As examples of concerned impurities, there are water and metal. Once water or metallic impurities are mixed in BCl_3, they can deteriorate the product performance and the process yield. Generally, to remove impurities from ultra high purity gases, ceramic or synthetic resin filters are used. However, metallic impurities in boron containing gases, including BCl_3 gas, are not removed well through these types of filters [5] and reason for this is not known. It may mean that metallic impurities in boron containing gases have structures which easily pass through these filters as the result of the interaction between gases and metal. So far, methods for removing impurities in high purity gases have been discussed in the literatures, but structures or states of impurities have not been studied. In particular, it is difficult to directly observe the structure of impurities in gas phase. Therefore, we consider that it is worthwhile to investigate the molecular states of impurities by a computational method as a precursory study toward establishing a more effective method for removing impurities.

Among several metallic impurities, since most abundant one is iron, we focus on iron-including impurities. We can think of several possible sources for iron impurities. The prime suspect is rust from the welded spots in the ductwork. Although the ductwork for semiconductor gases has corrosion resistance, the welded spots are relatively weak against halogen-contained gases, especially, under the presence of water [6]. Note that at most a few parts-per-million (ppm) of water is mixed in the ductwork.

As a first step to guess how iron impurities react with BCl_3 gas, we consider a reaction of $Fe(OH)_3$ with BCl_3. The first reason why we pick up this iron compound is that we would like to see a reaction with a hydroxyl function since hydrochloric (HCl) gas is known to exist in BCl_3 gas. Such HCl gas may come from the reaction with the iron impurities. The second reason is that rust mentioned above is likely to be in the form of goethite (α-FeO(OH)) [7–9], and its monohydrated form can be described as $Fe(OH)_3$.

This paper is organized as follows. In the next section, we briefly explain our quantum chemical computation method. We also describe our analysis method based on the Regional DFT (Density Functional Theory) and the Rigged QED (Quantum ElectroDynamics), and in particular we define the interaction energy density. In Sec. III, we show our results on the reaction of BCl_3 with water and that with $Fe(OH)_3$. The final section is devoted to our conclusion.

II Calculation Methods

II-i Ab initio electronic structure calculation

We perform ab initio quantum chemical calculation for several chemical reactions using density functional theory. In this calculation, we adopt the Lee-Yang-Parr (LYP) [10] gradient-corrected functionals for the correlation interaction, and it is employed with Becke's hybrid three parameters [11] for generalized-gradient-approximation (GGA) exchange-correlation functions (B3LYP). We employ 6-311G* basis set for Fe, B, O and Cl, which consists of all electron basis set by Wachters-Hay [12, 13], and 6-311G** basis set for H. This calculation shows reasonable results for high-spin states of iron hydroxide clusters. Analytical vibrational frequencies are obtained to calculate the zero-point energy (ZPE) correction. In this work, the geometric optimized structures and the electronic structures of each cluster model are calculated by GAUSSIAN03 program package [14]. The part of visualization in this paper is done using MOLDEN[15] and VMD[16] softwares.

II-ii Interaction energy density analysis

In the following section, we use newly-developed interaction energy density in our laboratory to analyze how and in which part of molecules are (de-)stabilized during the chemical process. This quantity is used in Ref. [17] to describe the stabilization of molecules through covalent bonds and van der Waals bonds. (It is also used in Ref. [18] recently.) It is defined in the framework of the Regional DFT and the Rigged QED[19–26] and can be calculated from the electronic stress tensor density $\overleftrightarrow{\tau}^S(\vec{r})$ whose components are given by

$$\tau^{Skl}(\vec{r}) = \frac{\hbar^2}{4m}\sum_i \nu_i \left[\psi_i^*(\vec{r})\frac{\partial^2\psi_i(\vec{r})}{\partial x^k \partial x^l} - \frac{\partial\psi_i^*(\vec{r})}{\partial x^k}\frac{\partial\psi_i(\vec{r})}{\partial x^l} + \frac{\partial^2\psi_i^*(\vec{r})}{\partial x^k \partial x^l}\psi_i(\vec{r}) - \frac{\partial\psi_i^*(\vec{r})}{\partial x^l}\frac{\partial\psi_i(\vec{r})}{\partial x^k}\right], \quad (1)$$

where $\{k, l\} = \{1, 2, 3\}$, m is the electron mass, and ν_i and $\psi_i(\vec{r})$ is the occupation number and natural orbital of the ith state, respectively. Taking a trace of $\overleftrightarrow{\tau}^S(\vec{r})$ gives energy density of the quantum system at each point in space. The energy density $\varepsilon_\tau^S(\vec{r})$ is given by

$$\varepsilon_\tau^S(\vec{r}) = \frac{1}{2}\sum_{k=1}^{3}\tau^{Skk}(\vec{r}). \quad (2)$$

Now, we can define the interaction energy density. Suppose that the system under consideration formally consists of two parts A and B and that the whole system has the energy distribution as $\varepsilon^S_{\tau,\mathrm{AB}}(\vec{r})$. When the parts A and B are considered separately, they have the energy distribution $\varepsilon^S_{\tau,\mathrm{A}}(\vec{r})$ and $\varepsilon^S_{\tau,\mathrm{B}}(\vec{r})$ respectively and $\varepsilon^S_{\tau,\mathrm{A}}(\vec{r}) + \varepsilon^S_{\tau,\mathrm{B}}(\vec{r}) \neq \varepsilon^S_{\tau,\mathrm{AB}}(\vec{r})$.

The difference stems from stabilization or destabilization due to the reaction between A and B at each point in space and we call it the interaction energy density $\Delta\varepsilon^S_\tau(\vec{r})$. Namely,

$$\Delta\varepsilon^S_\tau(\vec{r}) = \varepsilon^S_{\tau,\mathrm{AB}}(\vec{r}) - \left\{\varepsilon^S_{\tau,\mathrm{A}}(\vec{r}) + \varepsilon^S_{\tau,\mathrm{B}}(\vec{r})\right\}. \tag{3}$$

The region with negative $\Delta\varepsilon^S_\tau(\vec{r})$ corresponds to the stabilized region and the positive region denotes the destabilized region.

We also use conventional electron density difference $\Delta n(\vec{r})$ for the later discussion as defined below.

$$\Delta n_{\mathrm{AB}}(\vec{r}) = n_{\mathrm{AB}}(\vec{r}) - \left\{n_{\mathrm{A}}(\vec{r}) + n_{\mathrm{B}}(\vec{r})\right\}, \tag{4}$$

where $n(\vec{r})$ is the ordinary electron density at $\vec{r}$.

As shown in Ref. [17], in covalent bonding, the larger stabilization accompanies the larger atomic population (the region with negative $\Delta\varepsilon^S_\tau(\vec{r})$ has positive $\Delta n(\vec{r})$). However, note that this is not the case for van der Waals bonds, in which the stabilized region corresponds to the *decrease* in the electron density [17] (the region with negative $\Delta\varepsilon^S_\tau(\vec{r})$ has negative $\Delta n(\vec{r})$).

We use Molecular Regional DFT (MRDFT) package [27] to compute these quantities.

III Results and discussion

III-i Reaction with water

In this section, we study the reaction of BCl_3 with water. Although the hydrolysis of BCl_3, $BCl_3(g) + 3\,H_2O(l) \rightarrow B(OH)_3(aq) + 3\,HCl(aq)$, is a well-known textbook-level reaction, the situation we consider here is slightly different. In our case, since H_2O is much less (ppm level) than BCl_3, a relevant reaction would be $BCl_3 + H_2O \rightarrow BCl_2(OH) + HCl$.

Then, we start by examining how H_2O approach BCl_3 and form a complex Cl_3B—OH_2. We take the distance between B and O as a parameter, D, and for several values of D, we calculate the optimized configuration of the other atoms.

The obtained structures are shown in Fig. 1. We can regard them to be the snapshots of the continuous reaction process. While D is between 4.8 Å and 4.0 Å, we find that H_2O approach with a small angle from the BCl_3 plane. In Fig. 2, we show relative energy and charge transfer as functions of D. The charge transfer is calculated from the Mulliken charge. We obtain the structure of the stable reactant complex Cl_3B—OH_2 as shown in Fig. 3 at $D = 1.693$ Å. Below, we refer to this structure as "RC". This geometry is in good agreement with the one in the literature [28, 29]. We find that when H_2O approaches BCl_3 from an infinite distance, there is no energy barrier and total energy is stabilized by 0.2607 eV. Also note that the reaction proceeds as charge is transferred from BCl_3 to water (electrons from water to BCl_3).

Next, we search a reaction path from RC until the detachment of HCl. The energy along a certain intrinsic reaction coordinate (IRC) is plotted in Fig. 4. Some intermediate structures are also shown. In particular, the one labeled 1 is RC and 3 is the transition state (TS) respectively. This is reorganized in Fig. 5 and Table 1 which show the reaction pathway and relative energy. The activation energy is found to be 0.7300 eV. By detaching HCl, the system stabilizes by 0.6799 eV from RC. In the final step, there is energy increment of 0.0990 eV which corresponds to the strength of the hydrogen bond between H in HCl and O in $BCl_2(OH)$ (the distance between H and O is 2.054 Å). However, since it is rather small, $BCl_2(OH)$ and HCl are expected to be separated away in the gas phase.

Now, we analyze this reaction by using interaction energy density $\Delta\varepsilon^S_\tau(\vec{r})$ and electron density difference $\Delta n(\vec{r})$ as introduced in Sec. II. We first examine the process from $BCl_3 + H_2O$ to RC, namely the reactant complex formation. This is shown in Fig. 6. From $\Delta n(\vec{r})$ of panels (a) and (b), we see that BCl_3 and H_2O are polarized by the existence of the other molecule when they are separated. Then they attract each other by electrostatic interaction. After they approach closely as panel (c), electrons move from H_2O to BCl_3 rapidly as shown by the expansion of pink regions around BCl_3 in panels (d), (e) and (f).

This is consistent with the charge transfer plot in Fig. 2, which shows steepening trend for $D \lesssim 3.5\,\text{Å}$. As for $\Delta\varepsilon^S_\tau(\vec{r})$, general feature we notice is that positive $\Delta n(\vec{r})$ region (colored in pink) roughly corresponds to negative $\Delta\varepsilon^S_\tau(\vec{r})$ region (colored in blue) and vice versa. This indicates that each part in the system is stabilized by the increase in the electron density just as in the usual covalent bonding.

The process from RC to $BCl_2(OH) \cdot HCl$ via TS is next analyzed and results are shown in Fig. 7. We again see the correspondence between positive $\Delta n(\vec{r})$ region and negative $\Delta\varepsilon^S_\tau(\vec{r})$ region. Since we partition the system into $BCl_2(OH)$ and HCl for calculating $\Delta n(\vec{r})$ and $\Delta\varepsilon^S_\tau(\vec{r})$, it is easier to see the process backward from the panel (g). We see that red destabilized region expands from panel (g) to (a). This destabilized region is especially large in TS (panel (c)) around H_2O. Although this partitioning is not so well defined in (a) and (b), we see destabilized region around H_2O too. This is consistent with the energy level relation that RC has higher energy than $BCl_2(OH) \cdot HCl$.

III-ii Reaction with iron hydroxide

In this section, we study the reaction of BCl_3 with $Fe(OH)_3$. $Fe(OH)_3$ is our model of iron impurity and we investigate how this can react with BCl_3 molecules to produce HCl. It should be mentioned that $Fe(OH)_3$ has lower energy than $FeO(OH)\cdot H_2O$. As shown in Table 2, since sextet is the most stable, we adopt this state in the following calculation.

The entire reaction path we have searched is shown in Fig. 8. Table 3 shows relative energy for each step. For convenience, we split this path into four as in Fig. 9 (a)-(d) showing structures for each step. We will give detailed description for each of them below.

The earliest stages in the reaction path are shown in Fig. 9 (a). First, it is shown that BCl_3 approaches $Fe(OH)_3$ with some energy stabilization forming a reaction complex S_2. A possible simple path to detach HCl from S_2 is shown as $S_2 \rightarrow TS_1 \rightarrow S_3$. This is just like the one we have seen in the reaction between BCl_3 and H_2O described in Sec. III-i. We need the activation energy of $1.1653\,\text{eV}$. In the case of BCl_3 and $Fe(OH)_3$, however, the reaction complex S_2 can turn into more stable structure by cutting a bond B—Cl in the ring consists of B, Cl, O, and Fe atoms and leaving a Fe—Cl bond ($S_2 \rightarrow S_4$). Since the activation energy is rather high, it is likely that the latter path is taken in the BCl_3 gas. Also, as we will see below, the presence of many BCl_3 molecules (relative to $Fe(OH)_3$) makes it possible to open more effective paths to detach HCl molecules.

Now, let us consider the case that another BCl_3 approaches S_4. One more bond between BCl_3 and OH is formed to make S_5 and energy is stabilized by 1.1178 eV. To detach HCl from S_5, there are two reaction paths as shown in Fig. 9 (b). One is from S_5 to S_6 via TS_{2a} and another is via TS_{2b}. The former is similar to the BCl_3+H_2O case or the path $S_2 \rightarrow TS_1 \rightarrow S_3$ mentioned just above and its activation energy is relatively high, 0.8665 eV. By contrast, the latter has much lower barrier of 0.15083 eV. In this path, since HCl is detached from Cl and OH which are connected to different B, the distance between H and Cl is shorter in TS and much less energy is needed to form the bond.

The path after that is opened in a similar way (Fig. 9 (c)). Namely, HCl is not likely to be produced from within S_7 but detach after a complex with one more BCl_3 is formed. This complex is shown as S_8. Then HCl is again formed from Cl and OH which are connected to different B with a relatively low activation energy of 0.08919 eV ($S_8 \rightarrow TS_3 \rightarrow S_9$).

So far, we have learned that we can find an energetically more favorable path to detach HCl by attaching BCl_3 beforehand. Then, similar path to $S_2 \rightarrow S_4 \rightarrow S_5$ may take place for S_5 by attaching BCl_3. This turns out to be true and we find a path $S_5 \rightarrow S_{11} \rightarrow S_{12}$ as shown in Fig. 9 (d). S_{11} is stabilized by 0.59024 eV from S_5 by forming another Fe—Cl bond. After that, S_{12} is stabilized by 0.8491 eV from S_{11} by the interaction between BCl_3 and the last OH group bonded to Fe.

Finally, how HCl is detached from S_{12} is described. As shown by the path $S_{12} \rightarrow TS_4 \rightarrow S_{13}$, Cl and OH which are connected to different B bond to form HCl. This is similar to $S_5 \rightarrow TS_{2b} \rightarrow S_6$ and $S_8 \rightarrow TS_3 \rightarrow S_9$. It also has a relatively low activation energy of 0.22614 eV. We further examine whether one more HCl can be detached from

S_{13}. However, we cannot find such a path and we find that BCl_2OH is detached instead. Thus, the final product is $Fe(Cl)_2(OBCl_2)(OHBCl_2)$ shown as S_{14}.

To sum up, we have found

$$\mathrm{Fe(OH)_3 + BCl_3 \rightarrow Fe(OH)_2(OBCl_2) + HCl} \tag{5}$$

has high activation energy and unlikely to occur but there are two reactions with lower energy barriers which produce HCl and more stable Fe-compounds. They can be summarized as

$$\mathrm{Fe(OH)_3 + 3BCl_3 \rightarrow FeCl(OBCl_2)_2(OHBCl_2) + 2HCl} \tag{6}$$

and

$$\mathrm{Fe(OH)_3 + 3BCl_3 \rightarrow FeCl_2(OBCl_2)(OHBCl_2) + HCl + BCl_2OH} \tag{7}$$

In passing, it may be useful to comment on the geometrical structure of each complex in the reaction path. Generally speaking, a four-coordinate complex forms a square-planar or tetrahedral structure. We calculate the skewness of the complex defined as follows [30]:

$$\sigma = \frac{V - V_{\mathrm{opt}}}{V_{\mathrm{opt}}} \tag{8}$$

where V is the volume of the tetrahedron defined by the four atoms directly connected to Fe, and V_{opt} is the volume of a regular tetrahedron which has the common circumsphere to that tetrahedron. If $\sigma = 0$, the tetrahedron is regular and if $\sigma = 1$, it is square planar. The result is shown in Table 3. This result shows that the complexes we have dealt with are very close to regular tetrahedrons.

The analyses using $\Delta n(\vec{r})$ and $\Delta \varepsilon_{\tau}^{S}(\vec{r})$ for some parts of the reaction path are shown in Figs. 10-12. As is the cases which are examined in Sec. III-i, positive $\Delta n(\vec{r})$ region corresponds to negative $\Delta \varepsilon_{\tau}^{S}(\vec{r})$ region in general. Fig. 10 shows the process of BCl_3

approaching a complex $Fe(Cl)(OH)_2(BCl_2OH)$ to form a reaction complex and Fig. 11 shows the process of detaching HCl from the reaction complex. They are respectively similar to what we have seen in Figs. 6 and 7. Namely, we see blue stabilized region grows between BCl_3 and $Fe(Cl)(OH)_2(BCl_2OH)$ as the process proceeds from (a) to (e) in Fig. 10 and red destabilized region develops in the direction from (e) to (a) in Fig. 11. We show in Fig. 12 one more example of $\Delta\varepsilon^S_\tau(\vec{r})$ for the process of detaching HCl from the reaction complex. When we look Fig. 12 in the direction from panel (f) to (a), we see that red destabilized region grows, as is the case of Fig. 11.

IV Conclusion

We have investigated a reaction of BCl_3 with $Fe(OH)_3$ by ab initio quantum chemical calculation as one of the simplest models for a reaction of iron impurities in BCl_3 gas. We have found that compounds such as $Fe(Cl)(OBCl_2)_2(OHBCl_2)$ and $Fe(Cl)_2(OBCl_2)(OHBCl_2)$ are formed while producing HCl. The reaction paths to them are examined in detail and their activation energy is found to be relatively low due to the formation of a Fe-complex coordinated by several BCl_3 before detaching HCl. We have also examined a reaction with a single H_2O molecule (remember that H_2O is rare in the BCl_3 gas) and have found that it has high activation energy. Such difference in energy barriers indicates that it is more likely that the observed HCl originates from the reaction of BCl_3 with iron impurities rather than from the reaction with H_2O.

We have also analyzed the stabilization mechanism of these paths using newly-developed interaction energy density $\Delta\varepsilon^S_\tau(\vec{r})$ in our laboratory derived from electronic stress tensor in the framework of the Regional DFT and Rigged QED. We have compared this with electron density difference $\Delta n(\vec{r})$. We have found correspondence between positive (negative) $\Delta n(\vec{r})$ region and negative (positive) $\Delta\varepsilon^S_\tau(\vec{r})$ region in general. This indicates a covalent bond that a bond is stabilized by the increase in electron density. We believe this interaction energy density is very useful to analyze and visualize how and in which part of molecules are (de-)stabilized during the chemical process. Integrating the interaction energy density over some region would give good quantitative measure of stabilization. This will be investigated in our future work.

Although it is too early to conclude that the reaction paths we have shown are realized in the BCl_3 gas in the ductwork, it is reasonable to imagine iron impurities play some role in producing HCl. More detailed modeling of iron impurities in future would give us more hints for this issue.

Reference

[1] S. B. Herner *et al.*, Electrochemical and Solid-State Letters **7** (5), G108 (2004).

[2] Y. Kunii *et al.*, Applied Surface Science **224**, 68 (2004).

[3] A. Domaracka, E. Ptasińska-Denga, and C. Szmytkowski, Phys. Rev. A **71**, 052711 (2005).

[4] J. F. Briesacher, M. Nakamura and T. Ohmi, J. Electrochem. Soc. **138**, 3717 (1991).

[5] Taiyo Nippon Sanso Corporation, Kokai Tokkyo Koho JP 2008-37712 (2008). (in Japanese)

[6] Y. Ishihara *et al.*, J. Electrochem. Soc. **141**, 246 (1994).

[7] J. Kim, M. Kanematsu, and T. Noguchi, Proceedings of the Concrete Structure Scenarios, JSMS, Vol. 5, p. 51-56 (2005). (in Japanese)

[8] S. Suzuki *et al.*, Corrosion Science **47**, 1271 (2005).

[9] J. F. Boily, and A. R. Felmy, Geochimica et Cosmochimica Acta **72**, 3338 (2008)

[10] C. Lee, W. Yann, and R. G. Parr, Phys. Rev. B **37**, 785 (1988).

[11] A. D. Becke, J. Chem. Phys. **98**, 5648 (1993).

[12] A. J. H. Wachters, J. Chem. Phys. **52**, 1033 (1970).

[13] P. J. Hay, J. Chem. Phys. **66**, 4377 (1977).

[14] M. J. Frisch *et al.*, Gaussian 03, Revision B.05, Gaussian, Inc., Pittsburgh PA (2003).

[15] G. Schaftenaar and J. H. Noordik, J. Comput.-Aided Mol. Design **14**, 123 (2000).

[16] W. Humphrey, A. Dalke, and K. Schulten, J. Molec. Graphics **14**, 33 (1996).

[17] P. Szarek and A. Tachibana, J. Mol. Model **13**, 651 (2007).

[18] P. Szarek, K. Urakami, C. Zhou, H. Cheng, and A. Tachibana, J. Chem. Phys. **130**, 084111 (2009).

[19] A. Tachibana, Theor. Chem. Acc. **102**, 188 (1999).

[20] A. Tachibana, J. Chem. Phys. **115**, 3497 (2001).

[21] A. Tachibana, in *Stress Induced Phenomena in Metallization*, ed. by S. P. Baker, (American Institute of Physics, New York, 2002), p. 105.

[22] A. Tachibana, in *Reviews in Modern Quantum Chemistry, A Celebration in the Contributions of Robert Parr*, ed. by K. D. Sen, (World Scientific, Singapore, 2002), Chap. 45, p. 1327.

[23] A. Tachibana, in *Fundamental World of Quantum Chemistry, A Tribute to the Memory of Per-Olov Löwdin*, ed. by E. J. Brändas and E. S. Kryachko, (Kluwer Academic, Dordrecht, 2003), Vol. 2, p. 211.

[24] A. Tachibana, Int. J. Quant. Chem. **100**, 981 (2004).

[25] A. Tachibana, J. Mol. Model. **11**, 301 (2005).

[26] P. Szarek, Y. Sueda, and A. Tachibana, J. Chem. Phys. **129**, 094102 (2008).

[27] M. Senami, K. Ichikawa, K. Doi, P. Szarek, K. Nakamura, and A. Tachibana, Molecular Regional DFT program package, ver. 3. Tachibana Lab, Kyoto University, Kyoto (2008).

[28] G. Frenking, S. Fau, C. M. Marchand, and H. Grützmacher, J. Am. Chem. Soc. **119**, 6648 (1997).

[29] B. D. Rowsell, R. J. Gillespie and G. L. Heard, Inorg. Chem. **38**, 4659 (1999).

[30] Y. Ito *et al.*, Math. Comput. Simul., **75**, 200 (2007).

Table 1: Relative energy along the pathway of the reaction of BCl_3 with water shown in Fig. 5.

	Relative energy (eV)
BCl_3+H_2O	0
RC	-0.26065
TS	0.36501
$BCl_2(OH) \cdot HCl$	-0.94056
$BCl_2(OH) + HCl$	-0.84152

Table 2: Relative energy in units of eV for the optimized structure of several spin states of $Fe(OH)_3$ and $FeO(OH){\cdot}H_2O$. We take sextet of $Fe(OH)_3$ which has the lowest energy as the reference point.

	Quartet	Sextet	Octet
$Fe(OH)_3$	0.01366	0	5.48862
$FeO(OH){\cdot}H_2O$	0.04452	0.04936	0.17616

Table 3: Relative energy and skewness of tetrahedron (Eq. (8)) along the pathway of the reaction of BCl_3 with $Fe(OH)_3$ shown in Fig. 8.

	Relative energy (eV)	Skewness of tetrahedron σ
S_1	0	(3-coordinate)
S_2	-1.83438	0.0990
TS_1	-0.66899	0.0990
S_3	-1.70663	0.1013
S_4	-2.36146	0.0961
S_5	-3.47929	0.0324
TS_{2a}	-2.61284	0.0570
TS_{2b}	-3.32846	0.0355
S_6	-3.54107	0.0291
S_7	-3.41744	0.0801
S_8	-4.27892	0.1591
TS_3	-4.18973	0.0723
S_9	-4.57131	0.0515
S_{10}	-4.47948	0.0549
S_{11}	-3.88924	(5-coordinate)
S_{12}	-4.73834	(5-coordinate)
TS_4	-4.51220	(5-coordinate)
S_{13}	-4.72870	0.0364
S_{14}	-4.49319	0.0492

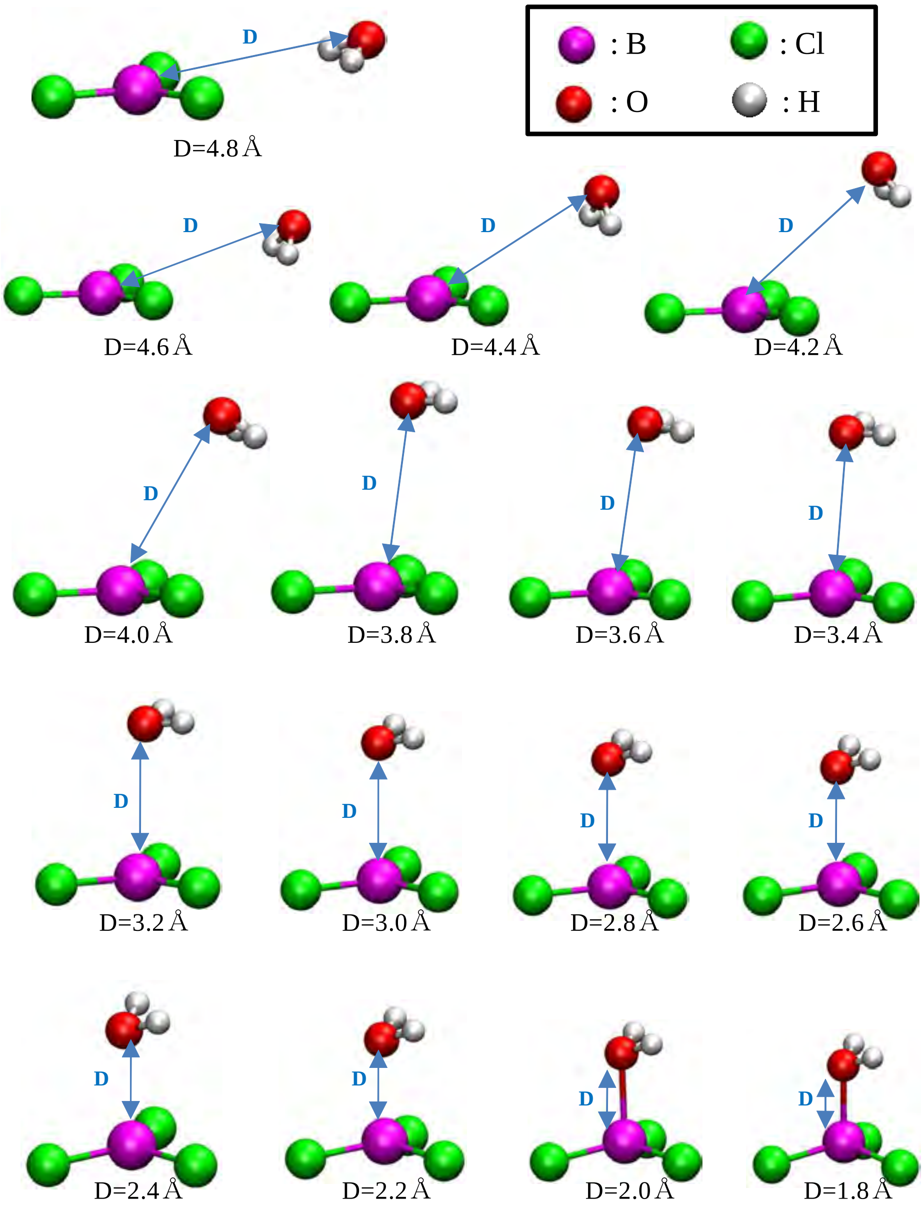

Figure 1: Optimized configurations of BCl_3 and H_2O at the given B—O distance (D).

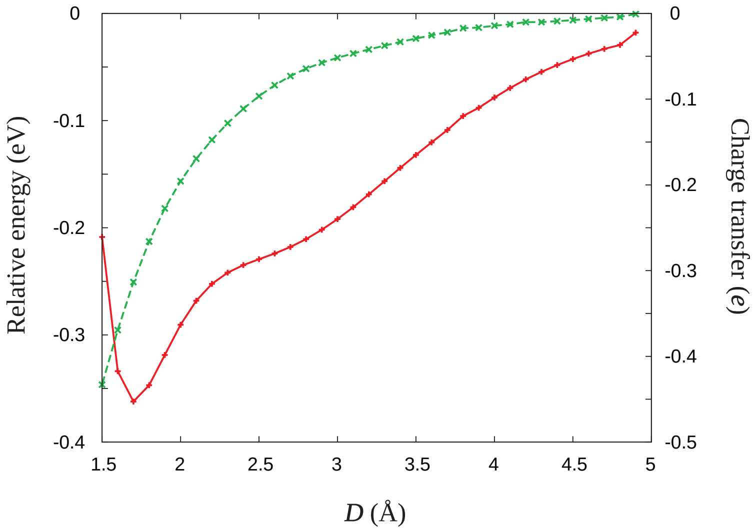

Figure 2: The plots of relative energy (solid red line) and charge transfer (dashed green line) vs B—O distance. The reference energy is the energy of structure in which H_2O locates at an infinite distance from BCl_3. The change in the charge of BCl_3 is plotted as the charge transfer on the right axis. Namely, the negative charge transfer indicates that electrons moves in to BCl_3 from H_2O.

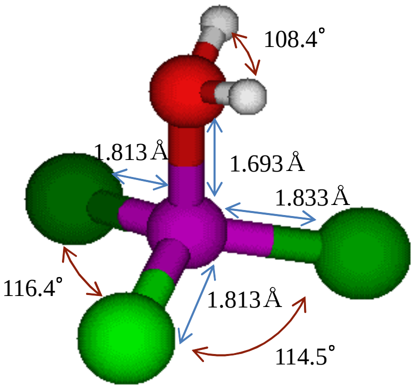

Figure 3: The structure of the stable reactant complex (RC), Cl_3B—OH_2.

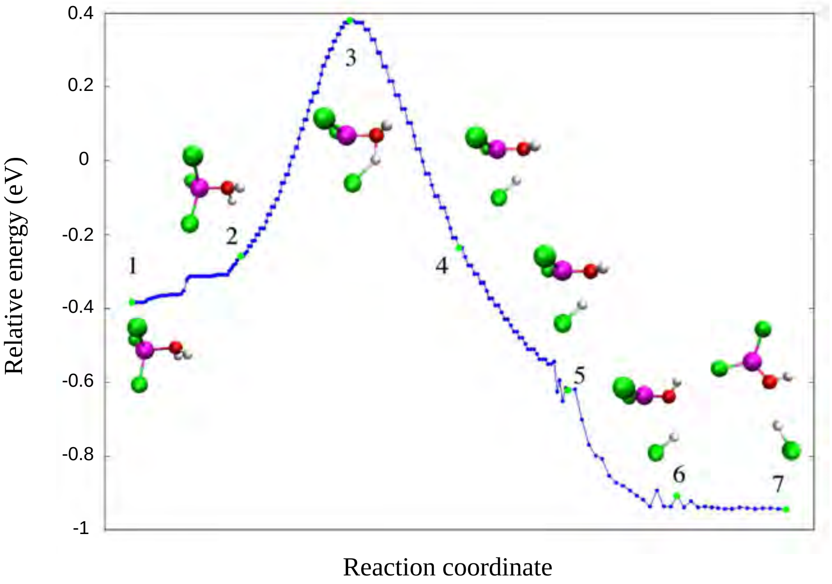

Figure 4: Relative energy of the path from $Cl_3B—OH_2$ (RC) to $BCl_2(OH) \cdot HCl$. The reference energy is the energy of structure in which H_2O locates at an infinite distance from BCl_3.

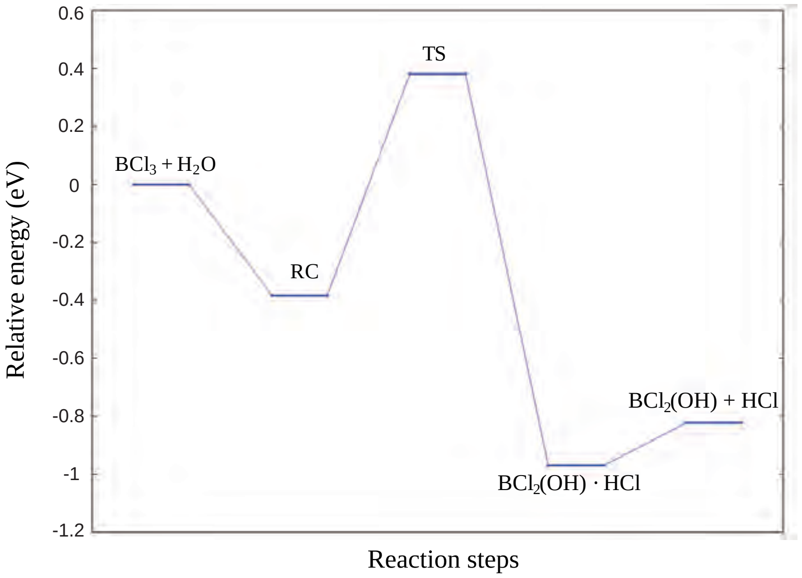

Figure 5: Reaction pathway from $BCl_3 + H_2O$ to $BCl_2(OH) + HCl$.

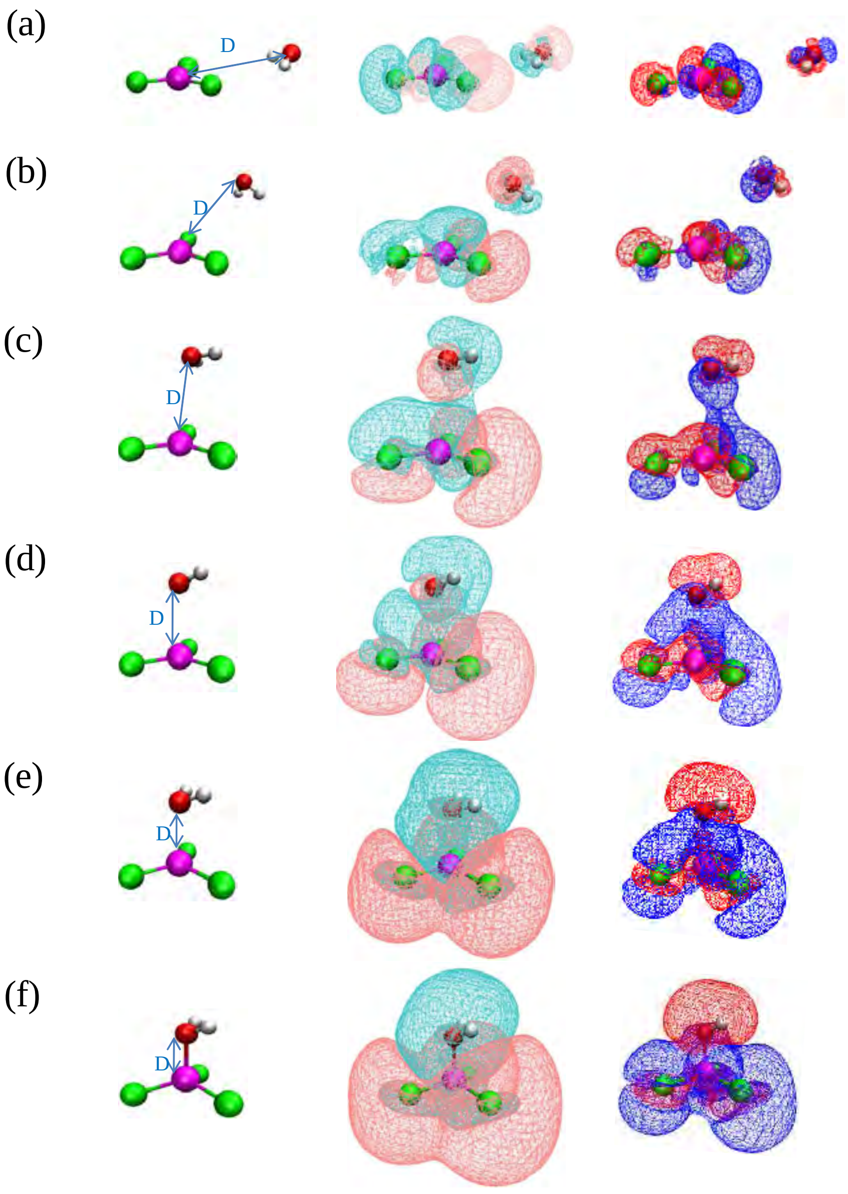

Figure 6: Optimized configurations (left column), electron density difference $\Delta n(\vec{r})$ (middle column) and interaction energy density $\Delta\varepsilon_{\tau}^{S}(\vec{r})$ (right column) during the process of the $Cl_3B—OH_2$ (RC) formation. We partition the system into BCl_3 and H_2O for calculating $\Delta n(\vec{r})$ and $\Delta\varepsilon_{\tau}^{S}(\vec{r})$. For $\Delta n(\vec{r})$, the light blue region has negative value and the pink region has positive value. For $\Delta\varepsilon_{\tau}^{S}(\vec{r})$, the blue region has negative value (*i.e.* stabilized region) and the red region has positive value (*i.e.* destabilized region). Each panel shows the B—O distance of (a) 4.8 Å, (b) 4.2 Å, (c) 3.4 Å, (d) 2.7 Å, (e) 2.2 Å and (f) 1.693 Å (RC).

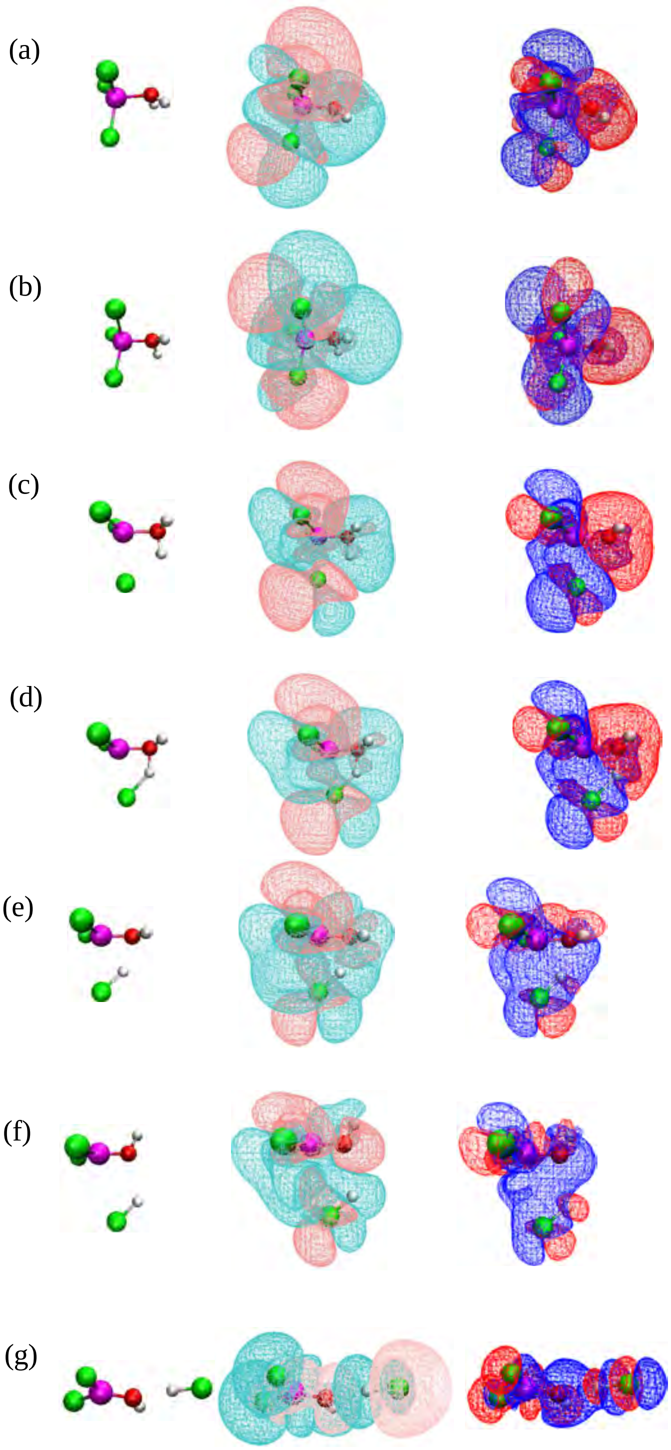

Figure 7: Same as Fig. 6 for the process from Cl_3B—OH_2 (RC) to the HCl detachment. We partition the system into $BCl_2(OH)$ and HCl for calculating $\Delta n(\vec{r})$ and $\Delta\varepsilon^S_\tau(\vec{r})$. Each panel (a)–(g) corresponds respectively to the step 1–7 indicated in Fig. 4. The panel (c) describes TS.

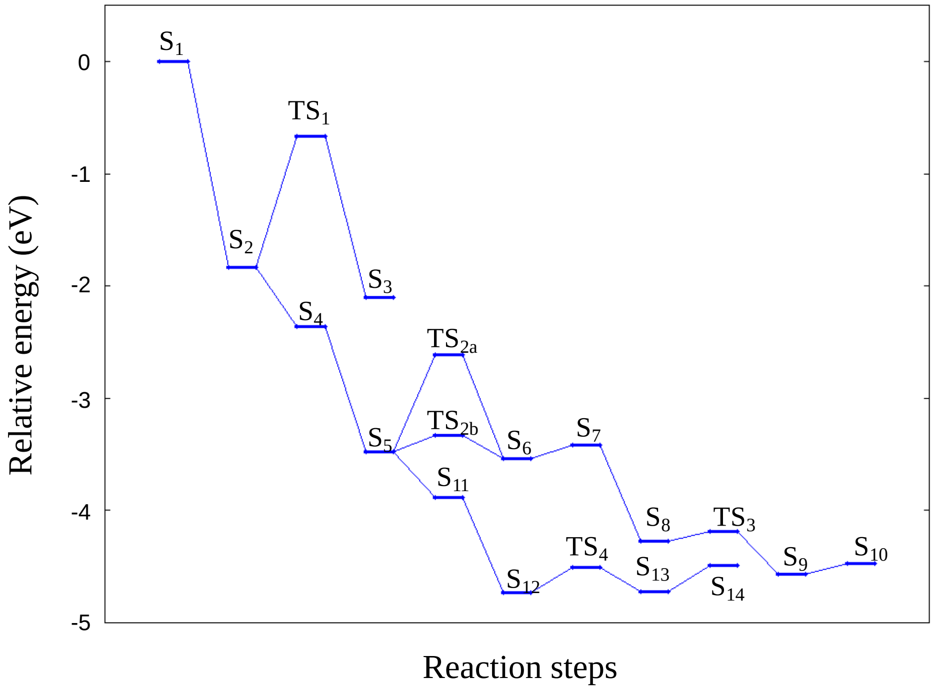

Figure 8: The pathway of reaction of $Fe(OH)_3$ with BCl_3 toward $Fe(Cl)(OBCl_2)_2(OHBCl_2)$ (S_{10}) and $Fe(Cl)_2(OBCl_2)(OHBCl_2)$ (S_{14}).

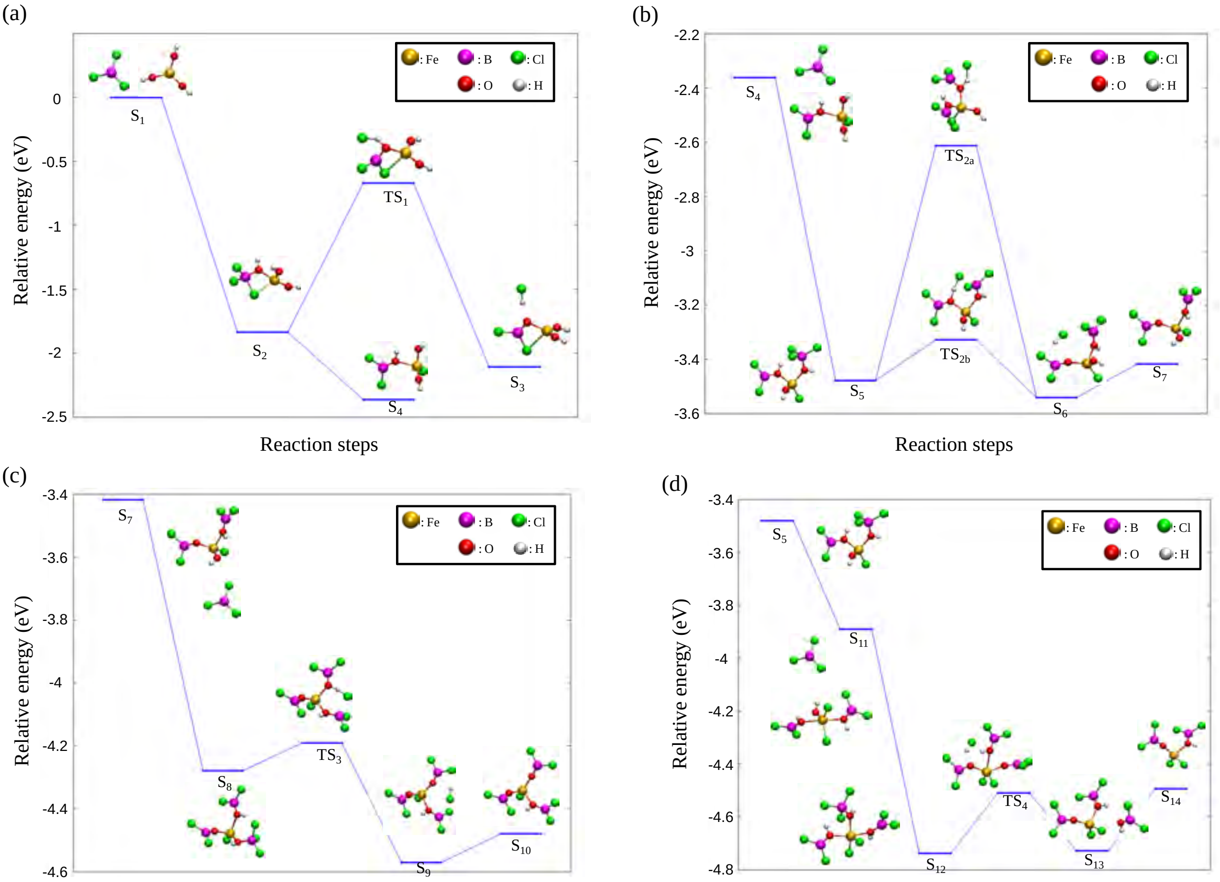

Figure 9: The reaction pathways (a) to $\mathrm{Fe(OH)_2(OBCl_2)\cdot HCl}$ (S_3) and to $\mathrm{FeCl(OH)_2(OHBCl_2)}$ (S_4), (b) to $\mathrm{Fe(OH)(Cl)(OBCl_2)(OHBCl_2)}$ (S_7), (c) to $\mathrm{Fe(Cl)(OBCl_2)_2(OHBCl_2)}$ (S_{10}), and (d) to $\mathrm{Fe(Cl)_2(OBCl_2)(OHBCl_2)}$ (S_{14}).

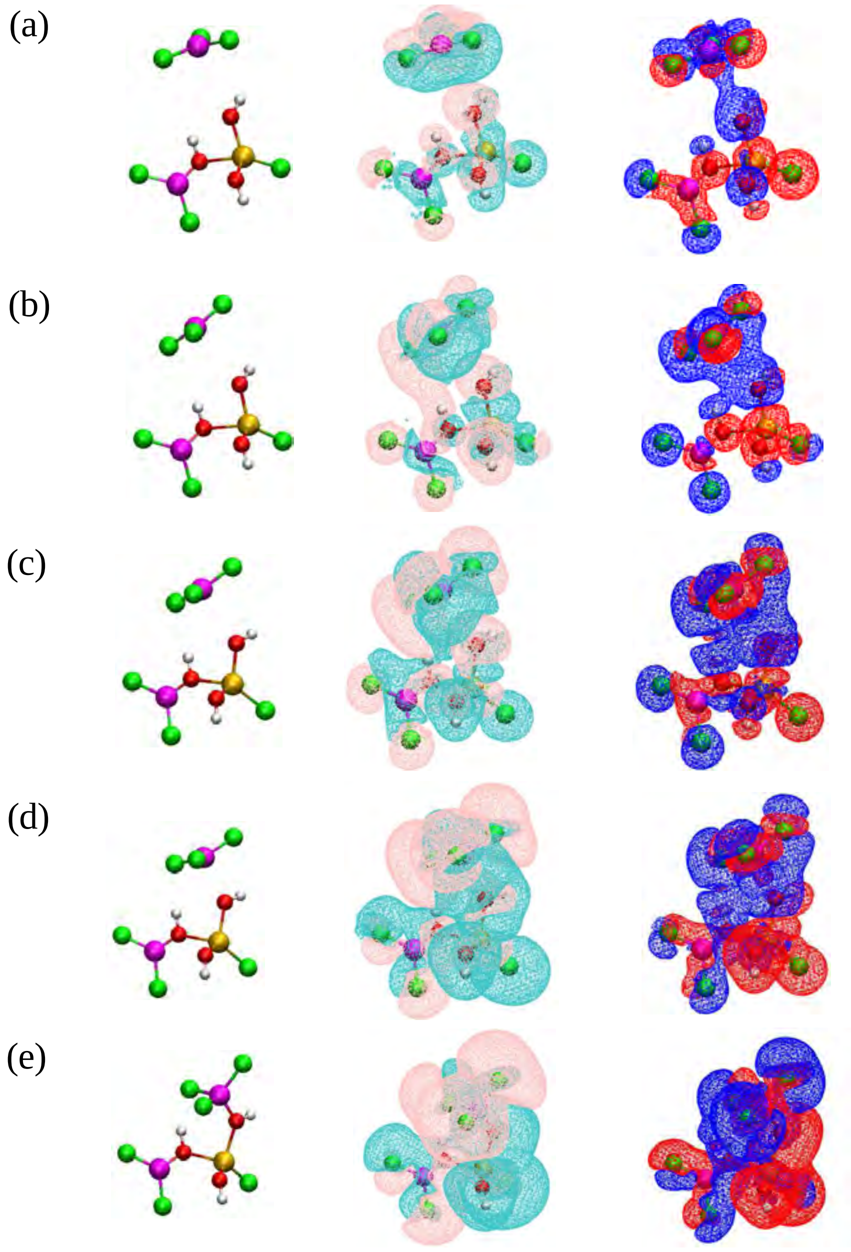

Figure 10: Same as Fig. 6 for the process $\mathrm{S}_4 \rightarrow \mathrm{S}_5$ (see also Fig. 9 (b)). We partition the system into $\mathrm{Fe(Cl)(OH)_2(BCl_2OH)}$ and $\mathrm{BCl_3}$ for calculating $\Delta n(\vec{r})$ and $\Delta\varepsilon_\tau^S(\vec{r})$.

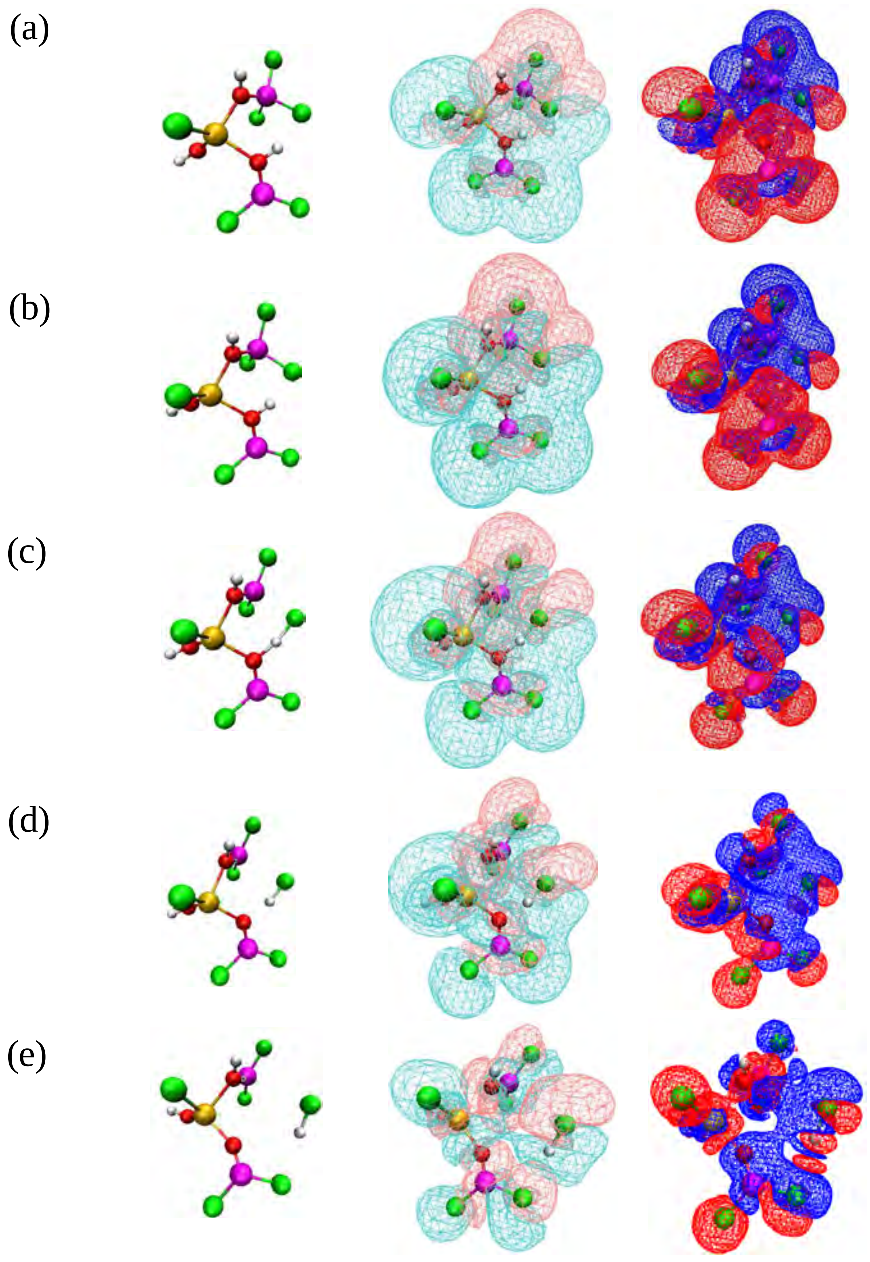

Figure 11: Same as Fig. 6 for the process $S_5 \rightarrow TS_{2b} \rightarrow S_6$ (see also Fig. 9 (b)). We partition the system into Fe(Cl)(OH)(BCl_2O)(BCl_2OH) and HCl for calculating $\Delta n(\vec{r})$ and $\Delta \varepsilon_{\tau}^{S}(\vec{r})$. TS_{2b} is denoted by the panel (c).

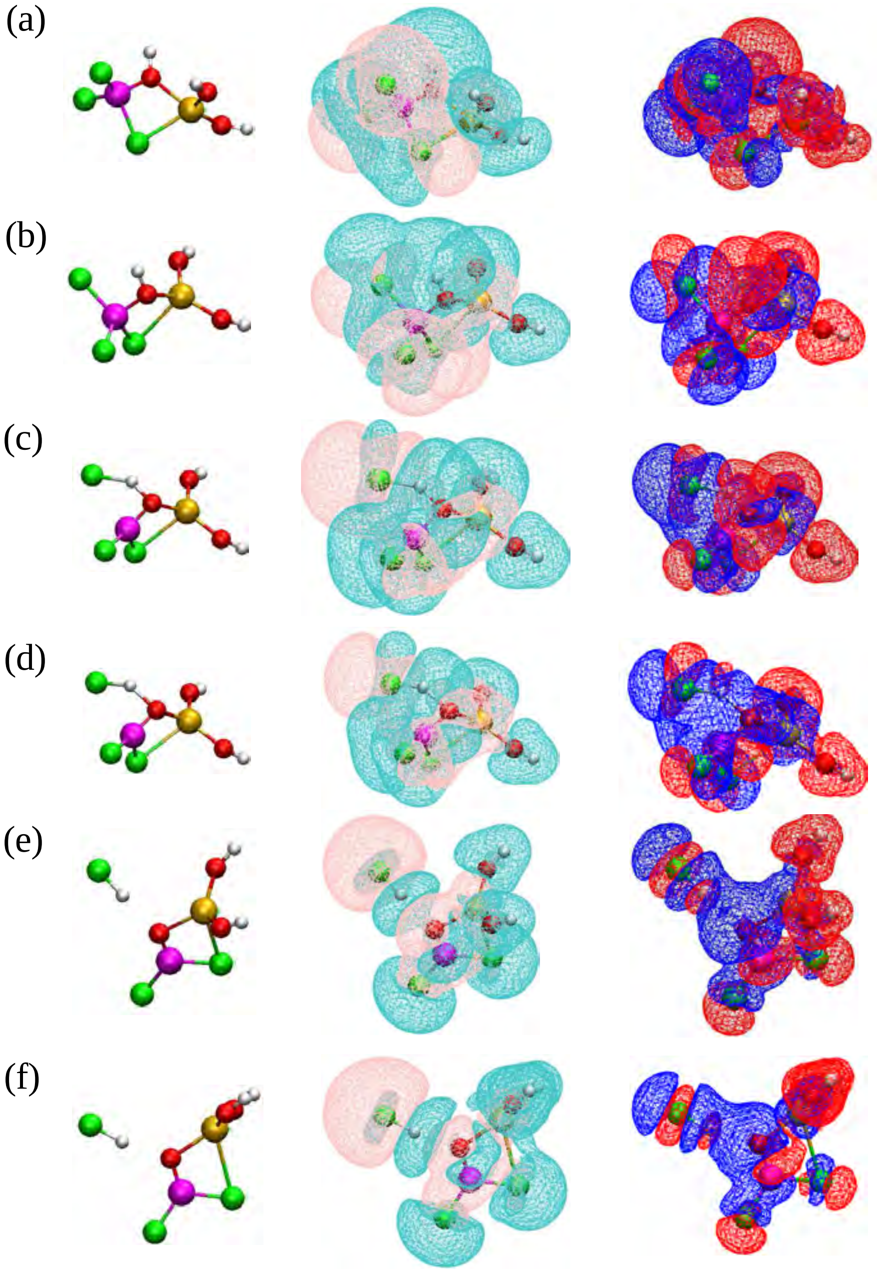

Figure 12: Same as Fig. 6 for the process $\mathrm{S}_2 \to \mathrm{TS}_1 \to \mathrm{S}_3$ (see also Fig. 9 (a)). We partition the system into $\mathrm{Fe(OH)_2(BCl_2O)}$ and HCl for calculating $\Delta n(\vec{r})$ and $\Delta\varepsilon_\tau^S(\vec{r})$. TS_1 is denoted by the panel (c).

Conclusion

In this thesis, several materials have been investigated in detail by first-principles calculation. Through this thesis, quantum energy density has been applied, and it has been shown that local analysis is a powerful tool for nanostructure materials.

We have studied several promising materials in microscopic viewpoints by local density quantities. In particular, properties of bonding states, chemical reaction, and response have been clarified by these quantities. Particularly, it has been shown that local polarizability and dielectric constant can illustrate dielectric properties of nanosize insulator materials. These local quantities have revealed that the dielectric response shows a rotational feature at inner parts of the hafnia, and hence distribution patterns of these quantities are very complicated.

Analysis of nanowire in Chapters 1 and 2 has been focussed on hydrogen adsorption properties of an aluminum nanowire and aluminum boride nanowires. In Chapter 1, we have investigated geometries, electronic structures, and hydrogen adsorption properties of aluminum boride nanowires. The aluminum nanowire is constructed by metallic bonds, and it can be considered that this nanowire has the good electric conductivity. On the other hand, the analysis by stress tensor density shows that aluminum boride nanowires have covalent bonds between boron atoms. Thus it can be considered that aluminum boride nanowires do not have the good electric conductivity like that of the aluminum nanowire. Actually, from the analysis by DOS, band, and electron density, we have confirmed that the aluminum nanowire has the good electric conductivity, while in the case of aluminum boride nanowire, electrons on the fermi level are localized around boron atoms and these nanowires do not show the electric conductivity like that of the aluminum nanowire.

Furthermore, in the case of the aluminum boride nanowire, results of stress tensor density shows that the covalent bond can be seen between hydrogen and boron atoms. On the other hand, in the case of the aluminum nanowire the typical covalent bond cannot be seen between hydrogen and aluminum atoms. These results show that the hydrogen adsorption energy of aluminum boride nanowires is larger than that of the aluminum boride nanowire. Actually, in the case of the aluminum boride nanowires, the adsorption energy has been calculated as -5.5 eV for nanowires whose radius has been calculated as 1.31 Å and for another aluminum boride nanowire whose radius is 1.31 Å and distance between boron rings is 1.54 Å the adsorption energy has been calculated as -5.6 eV. These values are much larger than that in the case of the aluminum nanowire (-3.6 eV). It can be recognized that the prediction from stress tensor density is demonstrated from these results. If all boron atoms of aluminum boride nanowires adsorb hydrogen atoms, wt% of hydrogen is calculated as 5.9 % and 6.2 %. These values are larger than that in the case of the aluminum nanowire (3.0%). From the other viewpoints, these results have also shown that the hydrogen atom on the aluminum nanowire can migrate more easily than that on the aluminum boride nanowire.

Accordingly, in Chapter 2, we have studied the activation energy of the hydrogen migration on the aluminum nanowire. In this chapter, we employ the different aluminum nanowire model. Its radius is 2.47 Å and its distance between aluminum rings is 2.46 Å. The hydrogen adsorption energy of this aluminum nanowire has been calculated as -2.08 eV. The hydrogen atom needs 0.57 eV to migrate on the plane which is perpendicular to the nanowire. On the other hand, for the migration to the axial direction, the activation energy is reduced to 0.19 eV. These results have shown that the hydrogen atom can migrate to the axial direction more easily than to the angular direction. Moreover, we have also showed that the hydrogen atom migrates on the shape volume given by the kinetic energy density. Generally, due to the small mass of the hydrogen atom, for the detail discussion of the dynamics, the effect of zero point vibration on the energy cannot be negligible. Hence, in this work, we have studied the effect of zero point vibration. The probability density of the vibrational mode of the ground state is localized around the most stable point of the PES, and the value of the zero point vibrational energy is calculated as 0.22 eV. Thus the adsorption energy including the zero point energy is -1.86 eV. In addition, the probability densities of vibrational mode of some excited states are localized around places which are different from the place where the ground state localized. The difference of the energy between one of these excited states and the ground state is calculated as 0.09 eV. This is much smaller than that of the difference of the PES. Hence, we must consider the excited states of the vibrational modes for the detailed discussion of the hydrogen migration.

Dielectric properties of cubic hafnium oxides have been investigated in terms of local dielectric constant. It is seen that the cubic hafnium oxide shows complicated response to external electric field. Particularly, the dielectric response shows rotational behavior in wide regions. These properties are only correctly clarified in the local and tensor analyses. In the ordinary global and averaged scalar polarization analyses, these properties cannot be described. As shown in our results, local dielectric constant is a good indicator of dielectric properties. The lattice oscillation has not been included in our works. To analyze macroscopic dielectric properties more accurately, the effect of nuclei has to be taken into account. In Chapter 3, the dielectric property of the cubic hafnium oxide has been investigated in terms of the polarizability density and the dielectric constant density. In the some regions around nuclei, we can see the complex eigenvalues of local polarizability and local dielectric constant. Some arguments of eigenvalues attain as large as about 10°. These complex eigenvalues show that the response to electric field of these regions have rotational properties. It is shown that due to the effect positions of the nuclei the response to the electric field has a rotation and is very complex.

In Chapter 4, we have focused on the cubic hafnium oxide with lanthanum atoms and clarified the effect of the lanthanum atom on its dielectric property. The large local polarizability can be seen around oxygen atoms. This is due to the ionic bonding state. Next, we have discussed an average of local dielectric constant around metal-oxygen bond axis. In the case of hafnium oxide, lanthanum oxide, and hafnium-oxygen bond of $\mathrm{HfLaO_x}$, one of eigenvalue of averages is much smaller than other eigenvalues. However this small eigenvalue cannot be seen in the case of the lanthanum-oxygen bond of $\mathrm{HfLaO_x}$. This shows that the response to electric field is complex due to impurities. Furthermore, the rotational response has appeared around only nuclei in hafnium oxide, while this response can be seen widely in $\mathrm{HfLaO_x}$. In terms of the average of local dielectric constant, the difference between hafnium oxide and $\mathrm{HfLa_x}$ is less than 5% . These results show that the effects of impurities on the microscopic dielectric properties are large, while the effects on the macroscopic dielectric properties are small.

In Chapter 5, we investigated the reaction of boron trichloride that are widely used in semiconductor device production process with iron impuritie that has been included in boron trichloride gas. It has been found that compounds, such as $\mathrm{Fe(Cl)(OBCl_2)_2(OHBCl_2)}$ and $\mathrm{Fe(Cl)_2(OBCl_2)(OHBCl_2)}$ are formed producing hydrogen chloride. The reaction paths to them have been examined in detail and their activation energy has been found to be relatively low due to the formation of a Fe-complex coordinated by several boron trichloride before detaching hydrogen chloride. Furthermore, the reaction with a single water molecule has been investigated and it has been found that it has high activation energy. Such difference in energy barriers indicates that it is more likely that the observed hydrogen chloride originates from the reaction of boron trichloride with iron impurities rather than from the reaction with a water molecule. The stabilization mechanism of these paths has been discussed using newly developed interaction energy density. This interaction energy density has been compared with electron density difference. It can be seen correspondence between positive (negative) region of difference of electron density and negative (positive) region of interaction energy density in general. This indicates that a covalent bond is stabilized by the increase in electron density. Hence this interaction energy density is very useful to analyze and visualize how and in which part of molecules are (destabilized) stabilized during the chemical process.

Publication list

Chapter 1

Theoretical study of the hydrogen adsorption on AlB nanowire

A. Fukushima, K. Doi, M. Senami, and A. Tachibana,

Journal of Power Sources, **184**, 60 (2008)

Chapter 2

Theoretical study of the migration of the hydrogen atom adsorbed on aluminum nanowire

A. Fukushima, K. Hirai, M. Senami, and A. Tachibana,

Surface Science, **604**, 1718 (2010)

Chapter 3

Local Dielectric Property of Cubic Hafnia

A. Fukushima, Y. Tsuchida, M. Senami, and A. Tachibana,

Japanese Journal of Applied Physics, **49** 111504 (2010)

Chapter 4

Local Dielectric Property of Hafnium and Lanthanum Atoms in $HfLaO_x$

A. Fukushima, S. Sugino, Y. Tsuchida, M. Senami, and A. Tachibana,

Japanese Journal of Applied Physics **49** 121504 (2010)

Chapter 5

A Theoretical Study on a Reaction of Iron(III) Hydroxide with Boron Trichloride by Ab Initio Calculation

K. Ichikawa, T. Myoraku, A. Fukushima, Y. Ishikawa, R. Isaki, T. Takeguchi, and A. Tachibana,

Journal of Molecular Structure, **915**, 1 (2009)

References

1. *Role of an Aluminum Atom on Graphene Sheets for Hydrogen Adsorption*

A. Fukushima, A. Sawairi, K. Doi, M. Senami, L. Chen, H. Cheng, and A. Tachibana,

In preparation

2. *Theoretical study of adsorption of lithium atom on the carbon nanotube*

M. Senami, Y. Ikeda, A. Fukushima, and A. Tachibana,

In preparation

3. *Caluculation of the electronic state in electronic current for nanowire model*

M. Senami, Y. Ikeda, A. Fukushima, and A. Tachibana,

Japanese Journal of Applied Physics, (2010) in press

Conference appearances

- *Theoretical Study of Stable Structure and Electric States of AlB Nanowire.*
  (in Japanese)
  A. Fukushima, K. Doi, P. Szarek, A. Tachibana,
  Symposium of Molecular Structure, 20-23 September 2006, Shizuoka, Japan

- *Theoretical Study of Hydrogen Adsorption Processes of Al and AlB Nanowire.*
  (in Japanese)
  K. Doi, A. Fukushima, Y. Kitagawa, K. Hirai, P. Szarek, A. Tachibana,
  The CSJ 87th Spring Meeting, 25-28 March 2007, Osaka, Japan

- *Theoretical Study of The Effect of Al Nanowire on the Hydrogen Adsorption on Graphene.* (in Japanese)
  K. Doi, A. Fukushima, P. Szarek, A. Tachibana,
  1st Symposium of Molecular Science, 17-20 September 2007, Miyagi, Japan

- *Theoretical Study of the Changes of the Electric Structures of Al and AlB Nanowires by the Hydrogen Adsorption.* (in Japanese)
  A. Fukushima, K. Doi, A. Tachibana,
  1st Symposium of Molecular Science, 17-20 September 2007, Miyagi, Japan

- *Theoretical Study on Chemical Bonding States and Dielectric Properties of High-k Oxides.* (in Japanese)

  S. Sugino, A. Fukushima, K. Doi, M. Senami, Akitomo Tachibana,

  13th Workshop on Gate Stack Technology and Physics, 14-15 January 2008, Shizuoka, Japan

- *First-principles Calculations for Si Nanowire in Electric Current and Electromagnetic Field.* (in Japanese)

  Y. Ikeda, A. Fukushima, K. Doi, M. Senami, A. Tachibana,

  13th Workshop on Gate Stack Technology and Physics, 14-15 January 2008, Shizuoka, Japan

- *Theoretical Study of the effect of the aluminum atom on the Hydrogen Adsorption on graphene.* (in Japanese)

  A. Fukushima, M. Senami, K. Doi, A. Tachibana,

  The CSJ 88th Spring Meeting, 26-30 March 2008, Tokyo, Japan

- *Theoretical Study of Hydrogen Adsorption on Al and AlB Nanowire.* (in Japanese)

  A. Fukushima, M. Senami, A. Tachibana,

  The 55th Spring Meeting JSAP and Related Societies, 27-30 March 2008, Chiba, Japan

- *First-principles Calculations for Si Nanowire in Electric Current and Electromagnetic Field.* (in Japanese)

  Y. Ikeda, A. Fukushima, K. Doi, M. Senami, A. Tachibana,

  13th Workshop on Gate Stack Technology and Physics, 22-26 March 2008, Osaka, Japan

- *Theoretical Study of Hydrogen Adsorption on Al and AlB Nanowire.* (in Japanese)

  A. Fukushima, M. Senami, A. Tachibana,

  11th Theoretical Chemistry Symposium, 22-24 May 2008, Kanagawa, Japan

- *Theoretical Study of Al and AlB Nanowire.* (in Japanese)

  A. Fukushima, M. Senami, A. Tachibana,

  Mechanical Engineering Congress 2008 Japan, 3-7 August 2008, Kanagawa, Japan

- *Theoretical Study of Hydrogen Adsorption on the aluminum doped graphene.* (in Japanese)

  A. Fukushima, M. Senami, A. Tachibana,

  The 69th Autumn Meeting 2008 (The Japan Society of Applied Physics) , 2-5 September 2008, Aichi, Japan

- *Theoretical Study of Al and AlB Nanowires for Hydrogen Storage Materials.* (in Japanese)

  A. Fukushima, M. Senami, A. Tachibana,

  JPS the Autumn Meeting 2008, 20-23 September 2008, Yamagata, Japan

- *First Principles Calculation for the conductivity a of silicon nanowire.* (in Japanese)

  A. Fukushima, M. Senami, A. Tachibana,

  JPS the Autumn Meeting 2008, 20-23 September 2008, Yamagata, Japan

- *Theoretical Study of High-k material for a new insulator.* (in Japanese)

  A. Fukushima, M. Senami, A. Tachibana,

  2nd Symposium of Molecular Science, 24-27 September 2008, Fukuoka, Japan

- *Theoretical Study of local dielectric properties of La and Hf oxides.*

  A. Fukushima, M. Senami, A. Tachibana,

  2008 International Workshop on DIELECTRIC THIN FILMS FOR FUTURE ULSI DEVICES:SCIENCE AND TECHNOLOGY, 5-7 November 2008, Tokyo, Japan

- *Theoretical Study of La and Hf oxides as the Gate insulator.*

  A. Fukushima, M. Senami, A. Tachibana,

  The IUMRS International Conference in Asia 2008, 9-13 December 2008, Aichi, Japan

- *Firt-Principles Study on the Conduction Properties of Si Nanowire.*

  Y. Ikeda, A. Fukushima, M. Senami, A. Tachibana,

  The IUMRS International Conference in Asia 2008, 9-13 December 2008, Aichi, Japan

- *First Principles Analysis for The Conduction Characteristics of Si Nanowires.* (in Japanese)

  Y. Ikeda, A. Fukushima, M. Senami, A. Tachibana,

  14th Workshop on Gate Stack Technology and Physics, 23-24 January 2009, Shizuoka, Japan

- *Theoretical Study of the effect of the metal atom on the hydrogen adsorption on the graphene.* (in Japanese)

  A. Fukushima, M. Senami, A. Tachibana,

  The 56th Spring Meeting JSAP and Related Societies, 30 March -2 April 2009, Ibaraki, Japan

- *Role of aluminum atoms for hydrogen adsorption on graphene sheets.*

  A. Fukushima, A. Sawairi, K. Doi, M. Senami, A. Tachibana,

  13th edition of the International Conference on the Applications of Density Functional Theory in Chemistry and Physics, 31 August -5 September 2009, Lyon, France

- *Theoretical Study of behavior of hydrogen atom on aluminum nanowire.* (in Japanese)

  A. Fukushima, K. Hirai, M. Senami, A. Tachibana,

  The 70th Autumn Meeting 2009 (The Japan Society of Applied Physics) , 8-11 September 2009, Toyama, Japan

- *First-principle calculations to express the local conductivity of materials.* (in Japanese)

  M. Senami, Y. Ikeda, A. Fukushima, A. Tachibana,

  The 70th Autumn Meeting 2009 (The Japan Society of Applied Physics) , 8-11 September 2009, Toyama, Japan

- *Theoretical Study on Dielectric Property and Chemical Bonding States of High-k Oxides.* (in Japanese)

  M. Senami, A. Fukushima, Y. Tsuchida, A. Tachibana,

  15th Workshop on Gate Stack Technology and Physics, 22-23 January 2010, Shizuoka, Japan

- *First-principles Calculations for Local Property of Conductance.* (in Japanese)

  M. Senami, Y. Ikeda, A. Fukushima, A. Tachibana,

  15th Workshop on Gate Stack Technology and Physics, 22-23 January 2010, Shizuoka, Japan

- *Analysis for Electron Transport Properties of Silicon Nanowires Using Local Electrical Conductivity.* (in Japanese)

  Y. Ikeda, A. Fukushima, M. Senami, A. Tachibana,

  15th Workshop on Gate Stack Technology and Physics, 22-23 January 2010, Shizuoka, Japan

- *Theoretical study of the local dielectric properties using local dielectric constant.* (in Japanese)

  A. Fukushima, Y. Tsuchida, M. Senami, A. Tachibana,

  The 57th Spring Meeting JSAP and Related Societies, 17-20 March 2010, Kanagawa, Japan

- *Electronic structure calculations to express the current in nanowire models.* (in Japanese)

  M. Senami, Y. Ikeda, A. Fukushima, A. Tachibana,

  The 57th Spring Meeting JSAP and Related Societies, 17-20 March 2010, Kanagawa, Japan

- *Analysis of electron transport properties of silicon nanowire by local conductivity.* (in Japanese)

  M. Senami, Y. Ikeda, A. Fukushima, A. Tachibana,

  JPS the 65th annual Meeting, 20-23 March 2010, Okayama, Japan

- *Theoretical study of local dielectric property of high-k materials.* (in Japanese)

  M. Senami, A. Fukushima, Y. tsuchida, A. Tachibana,

  International symposium on Technology Evolution for Silicon Nano-Electronics, 3-5 June 2010, Tokyo, Japan

- *Calculations of the electronic structures for the conduction states of silicon nanowires.* (in Japanese)

  Y. Ikeda, A. Fukushima, M. Senami, A. Tachibana,

  The 71st Autumn Meeting 2010 (The Japan Society of Applied Physics) , 14-17 September 2010, Nagasaki, Japan

- *Theoretical study of response to electric field in local region in metal oxide.* (in Japanese)

  M. Senami, A. Fukushima, Y. Tsuchida, A. Tachibana,

  JPS the Autumn Meeting 2010, 23-26 September 2010, Osaka, Japan